Distribution Agreement

In presenting this thesis or dissertation as a partial fulfillment of the requirements for an advanced degree from Emory University, I hereby grant to Emory University and its agents the non-exclusive license to archive, make accessible, and display my thesis or dissertation in whole or in part in all forms of media, now or hereafter known, including display on the world wide web. I understand that I may select some access restrictions as part of the online submission of this thesis or dissertation. I retain all ownership rights to the copyright of the thesis or dissertation. I also retain the right to use in future works (such as articles or books) all or part of this thesis or dissertation.

Signature:

_____ _____

Jacob Mattingly Date

RNA and Protein Features Controlling Bacterial Translational Fidelity

By

Jacob Mattingly
Doctor of Philosophy

Biochemistry, Cell, and Developmental Biology

_____
Christine Dunham, PhD
Advisor

_____
Graeme Conn, PhD
Committee Member

_____
Homa Ghalei, PhD
Committee Member

_____
Bo Liang, PhD
Committee Member

_____
Daniel Reines, PhD
Committee Member

Accepted:

_____

Kimberly Jacob Arriola, PhD

Dean of the James T. Laney School of Graduate Studies

_____
Date

RNA and Protein Features Controlling Bacterial Translational Fidelity

By

Jacob Mattingly
B.S., University of Kentucky, 2016

Advisor: Christine M. Dunham, Ph. D.

An abstract of
A dissertation submitted to the Faculty of the
James T. Laney School of Graduate Studies of Emory University
in partial fulfillment of the requirements for the degree of
Doctor of Philosophy
in Biochemistry, Cell, and Molecular Biology
2024

Abstract

RNA and Protein Features Controlling Bacterial Translational Fidelity

By Jacob Mattingly

Translation is the essential process by which all cells use information encoded in messenger RNA (mRNA) to direct the synthesis of proteins. To perform translation, cells use large complexes of RNA and protein known as ribosomes, which coordinate with transfer RNAs (tRNAs) and proteins known as translation factors to extend growing polypeptides through sequential addition of amino acids. The translational machinery has evolved mechanisms to protect the accuracy (fidelity) of protein synthesis, and studying these mechanisms can give us a clearer understanding of the processes underlying protein synthesis and assist in development of translation-targeting antibiotic drugs. To begin translation, ribosomes select a dedicated tRNA used only for initiation (called $tRNA^{fMet}$ in bacteria) and begin synthesizing proteins at a specific mRNA sequence (typically AUG, but sometimes GUG or UUG in bacteria). During initiation, $tRNA^{fMet}$ is recognized against all other cellular tRNAs through features including a series of three consecutive G-C base pairs in its anticodon stem, which interact with the ribosomal RNA (rRNA). Altering the sequence of the middle G-C base pair to C-G (yielding a mutant variant known as $tRNA^{fMet}$ M1) weakens interactions with the ribosome and appears to reduce the fidelity of initiation. The initiation factor IF2 restores normal initiation behavior to $tRNA^{fMet}$ M1, suggesting a previously unknown quality control role for IF2. Structural studies of initiation using $tRNA^{fMet}$ M1 demonstrate that IF2 strengthens the interaction of the tRNA with 16S rRNA nucleotide G1338, which may explain its ability to restore normal initiation *in vitro*. After initiation, ribosomes enter the elongation step of translation, where the growing protein is extended. Errors in elongation can be induced by aminoglycoside antibiotics, a critical class of ribosome-targeting antibiotics which are used in the treatment of severe or chronic infections that often respond poorly to other antibiotic classes. Aminoglycoside resistance via modification of their rRNA target threatens the efficacy of this class of drugs, although some aminoglycosides evade this mode of resistance better than others. Structural and simulation studies of the interaction of aminoglycosides with aminoglycoside-resistant ribosomes suggest several drug design principles that may be used to overcome resistance and preserve aminoglycoside efficacy.

RNA and Protein Features Controlling Bacterial Translational Fidelity

By

Jacob Mattingly
B.S., University of Kentucky, 2016

Advisor: Christine M. Dunham, Ph. D.

A dissertation submitted to the Faculty of the
James T. Laney School of Graduate Studies of Emory University
in partial fulfillment of the requirements for the degree of
Doctor of Philosophy
in Biochemistry, Cell, and Molecular Biology
2024

Acknowledgements

I am incredibly thankful to my research mentor, Dr. Christine Dunham, for her inspiration and guidance throughout my graduate research. Christine was instrumental in getting my wife and me to Emory, and I've come to share her appreciation for structural biology and the fascinating complexity of protein synthesis.

I appreciate the direction of my dissertation committee, Drs. Graeme Conn, Homa Ghalei, Bo Liang, and Danny Reines, who gave me constant encouragement and always saw the best in me and my work.

I thank my former research mentors, Drs. Wenke Feng, Chi Li, Yinan Wei, and Emily Curran, for their patience with me as I developed my skills as a scientist.

I thank the Dunham Lab members past and present for sharing the ups and downs of research with me. Thank you to Dr. Eric Hoffer for teaching me the value of always reading the manual, Drs. Ha An Nguyen and Pooja Srinivas for helping me learn how to be a structural biologist, Drs. Lexie Kuzmishin-Nagy, Evy Kimbrough, and Tiffany Trieu for letting me constantly bounce ideas around with them, Julia Tanquary for being an amazing collaborator and coworker, and all of my other coworkers for building a friendly and welcoming research team.

I thank my collaborators in the Conn Lab for sharing their work with me and for treating me like the expert I've tried to become.

Many thanks go out to the electron microscope facilities that supported my work: NCCAT, PNCC, and the Emory IEMC. In particular, Drs. Ricardo Guerrero-Ferreira and Ravi Koripella have been instrumental in teaching me cryo-EM and helping to get my work across the line when deadlines were tight.

I am thankful to my parents, Mike and Lisa Mattingly, for giving me the gift of life and teaching me to live with principle and to strive to improve myself.

Finally, I thank my wife, Dr. Rachel Jang, for being an immense source of love and support throughout this process. I am so proud of what we've managed to achieve together in the past ten years, and I look forward to the rest of forever with you.

Table of Contents

List of Figures

List of Tables

Chapter 1: Introduction - Overview of Translation and Translational Fidelity

Proteins are biopolymers composed of amino acids that serve as critical structural and functional components of all living cells. Cells use information encoded in genetic material to direct the synthesis of new protein molecules through sequential addition of amino acids to a growing polypeptide chain[1]. Because of the importance of proteins in all aspects of cellular function, the maintenance of protein synthesis accuracy (fidelity) is an issue of great scientific interest. Better understanding how cells maintain the accuracy of protein synthesis can reveal unknown functions of the machinery cells use to synthesize new proteins and can better inform the design of antibiotics targeting protein synthesis in bacterial pathogens.

1.1: Architecture and function of translational machinery

Translation is the essential, conserved process by which cells in all domains of life decode messenger RNA (mRNA) information to direct proteins synthesis. It is carried out by ribosomes, megadalton-scale ribonucleoprotein machines consisting of two subunits designated by their sedimentation coefficients: a large subunit (50S in bacteria and archaea and 60S in eukaryotes) and a small subunit (30S in bacteria and archaea and 40S in eukaryotes), which join during the initiation step of translation to form complete ribosomes (70S in bacteria and archaea and 80S in eukaryotes) (Fig. 1A)[1]. Ribosomes feature two conserved functional centers composed entirely of RNA, with accessory proteins aiding in ribosome biogenesis and function[1, 2].

Ribosomes use adaptor molecules called transfer RNAs (tRNAs) to assemble new polypeptides. tRNAs carry amino acids at their 3’ ends (acceptor ends) and decode mRNA information during translation to direct selection of the appropriate amino acids[3]. Information in mRNA is encoded in three-nucleotide units called codons, which base pair with a corresponding three-nucleotide tRNA anticodon during translation[4]. Ribosomes contain three tRNA binding sites

which interact with tRNAs throughout the translation cycle. The aminoacyl site (A site) binds new aminoacyl-tRNAs (aa-tRNAs), which are delivered by a dedicated elongation factor and add corresponding amino acids to the growing peptide chain[1, 5]. The peptidyl site (P site) holds the peptidyl-tRNA, which carries the growing peptide chain prior to its release during translation termination[1, 5]. Finally, ribosomes contain an exit site (E site), which binds deacylated tRNAs as they leave the ribosome after their peptidyl chains have been transferred to new tRNAs (Fig. 1B)[1, 5, 6]. During the translation cycle, individual tRNAs enter the ribosome at the A site and are translocated through the ribosome by a dedicated elongation factor during each cycle of elongation of the nascent peptide until reaching the E site[1].

Ribosomes possess two evolutionarily conserved functional centers composed entirely of ribosomal RNA (rRNA) which are crucial for their function of directing protein synthesis. The peptidyl transferase center is housed on the large ribosomal subunit, resides near the acceptor ends of the A- and P-site tRNAs, and catalyzes the transpeptidation reaction between peptidyl-tRNA molecules residing in the P site and aminoacyl-tRNA molecules residing in the ribosomal A site. These reactions yield deacylated P-site tRNAs and A-site peptidyl-tRNAs which have extended the growing peptide by one amino acid[7]. These tRNAs are moved through the ribosome (into the E and P sites, respectively) during the translocation step of the translation cycle to permit delivery of new tRNAs to the ribosome and further elongation of the nascent polypeptide[1, 8]. Disruption of the peptidyl transferase center arrests protein synthesis, which can stall cell growth or result in cell death[9-13]. The second conserved functional center of ribosomes, the decoding center, resides on the small subunit and uses 16S rRNA nucleotides which inspect the base pairing between the mRNA and newly delivered aa-tRNAs to direct the selection of the appropriate aa-tRNA during each cycle of elongation[4, 14-17]. Because of its function in determining accurate tRNA selection, disruption of the decoding center can produce errors in protein sequence, which can lead to cell death through the accumulation of nonfunctional or toxic mis-

translated protein products[18-20]. Both the peptidyl transfer and decoding functions of the ribosome are common targets of translation-disrupting antibiotics, which bind near the ribosome's functional centers and alter their local rRNA conformations[13].

1.2: Steps of the bacterial translation cycle

To produce proteins from an mRNA message, ribosomes must execute a series of steps coordinated by mRNA features and translation factors. The translation factors help to regulate the speed and fidelity of the steps of the translation cycle, with several using GTP as an energy source to drive these processes forward[8, 21]. The translation cycle begins with initiation, beginning with the association of mRNA, initiation factors, and a dedicated initiator tRNA on the bacterial 30S ribosomal subunit and culminating with the recruitment of the 50S subunit and formation of the mature 70S initiation complex[22]. During initiation, the bacterial small ribosomal subunit base pairs with a purine-rich region of the mRNA upstream of the start codon, termed the Shine-Dalgarno (SD) sequence, using its complementary anti-Shine-Dalgarno sequence at the 3' end of its 16S rRNA[23]. The SD sequence precedes an mRNA spacer which positions the mRNA start codon (typically AUG, with GUG and UUG serving as less common canonical start codons in bacteria) in the P site of the 30S subunit[23]. Concurrently, and without a required order of assembly, the 30S subunit associates with the initiation factors IF1, IF2 (a GTPase), and IF3 and a dedicated initiator tRNA, $tRNA^{fMet}$, which carries an *N*-formyl methionine moiety at its acceptor end, to form the 30S initiation complex (30S IC). The initiation factors aid in tRNA and start codon selection, with IF3 assisting in the rejection of non-start mRNA codons and elongator tRNAs and IF2 helping to select initiator $tRNA^{fMet}$ through direct inspection of the *N*-formyl methionine moiety[24-26]. A series of three G-C base pairs in the anticodon stem loop of $tRNA^{fMet}$ also assist in its selection by the 30S subunit during initiation through the formation of interactions between the 16S rRNA and the tRNA minor groove (referred to as A-minor interactions)[27-31]. Following association of the mRNA, initiator

tRNA, and initiation factors on the small ribosomal subunit, IF1 and IF3 dissociate and the large ribosomal subunit is recruited by IF2, which is ejected from the assembled 70S initiation complex (70S IC) following GTP hydrolysis (Fig. 2A)[25, 32]. Initiation is typically the rate-limiting step of translation in bacteria and determines how efficiently a given mRNA is translated[21]. For this reason, both its speed and fidelity are crucial for translation, with inefficient initiation leading to low levels of protein expression and dysregulation of start codon or initiator tRNA selection potentially leading to spurious initiation at non-start mRNA codons.

Following assembly of the 70S IC and dissociation of initiation factors, the translating ribosome complex becomes competent for elongation, during which the nascent polypeptide is extended through the sequential addition of amino acids. The GTPase elongation factor EF-Tu delivers new aa-tRNAs to the ribosomal A site (in the form of EF-Tu·aa-tRNA·GTP ternary complex), where 16S rRNA nucleotides A1492 and A1493 (*E. coli* numbering) of the decoding center inspect the tRNA-mRNA pairing, with cognate tRNAs (*i.e.*, tRNAs with anticodon sequences complementary to the mRNA codon) being selected for amino acid incorporation into the nascent polypeptide[15, 33]. The decoding center is crucial for accurate selection of tRNAs during elongation, with disruption of its function leading to selection of incorrect tRNAs and production of inaccurately synthesized proteins[13, 18-20]. Cognate pairings with the mRNA codon permit full accommodation of aa-tRNAs onto the ribosome, which is followed by peptidyl transfer from the P-site tRNA to the new A-site aa-tRNA, yielding a nascent polypeptide which is one amino acid longer than before peptidyl transfer[15, 34]. Following peptidyl transfer, the tRNAs undergo a change in position on the 50S subunit, with the acceptor end of the A-site peptidyl-tRNA moving toward the P site and the acceptor end of the deacylated P-site tRNA moving toward the E site[35, 36]. These shifts in tRNA position are coupled with a ratcheting movement in the 30S subunit, after which the GTPase elongation factor EF-G binds the ribosome to translocate the tRNA anticodon stems and their associated base paired mRNA codons into the adjacent tRNA binding site[37, 38]. Following

translocation, EF-G dissociates, yielding a ribosome complex competent for receiving another aa-tRNA in the A site to begin another cycle of elongation (Fig. 2B)[39, 40].

Ribosomes continue translating mRNA into protein until reaching mRNA codons which signal the ribosome to terminate translation. These stop codons (with sequence UAG, UGA, or UAA) are not natively decoded by tRNAs and are instead decoded by the release factors RF1 (which recognizes UAG and UAA codons) and RF2 (which recognizes UGA and UAA codons)[41]. Upon recognition of a stop codon presented at the ribosomal A site, release factors use their characteristic GGQ amino acid motifs to deliver an ordered water molecule to the peptidyl transferase center, which is used to hydrolyze the peptidyl-tRNA linkage of the P-site tRNA, releasing the completed protein (Fig. 2C)[41, 42]. Following peptide release, ribosomes are split into their component subunits in a process involving ribosome recycling factor (RRF) and EF-G, where they can subsequently participate in initiation of new translation (Fig. 2D)[43].

1.3: Maintenance and disruption of translational fidelity

Both the initiation and elongation stages of the translation cycle require the coordination of rRNA and tRNA features along with translation factors to prevent errors and maintain the accuracy of protein synthesis (Fig. 3A-B). Proper selection of translation start sites, start codons, and initiator tRNAs is essential for production of proteins, with start codon sequence and mutations weakening the interaction between the 16S rRNA and $tRNA^{fMet}$ anticodon stem affecting the efficiency of initiation[27, 29, 31, 44]. In bacteria, AUG is typically used as the start codon, with GUG and UUG serving as less common canonical start codons[31, 44]. The initiation factor IF3 aids in the rejection of incorrect start codons to maintain the fidelity of initiation[22, 45, 46]; however, it is still unclear why CUG codons are used only rarely for translation initiation given that AUG, GUG, and UUG are each used for canonical translation initiation in bacteria. Additionally,

interactions between the initiator tRNA and the ribosome are crucial for accurate and efficient initiation. 16S rRNA nucleotides A1339 and G1338 (*E. coli* numbering for rRNA nucleotides is used for thoughout this chapter) form tandem type I and type II A-minor interactions, respectively, with a series of three consecutive G-C base pairs in the $tRNA^{fMet}$ anticodon stem[30]. Mutation of the middle G-C base pair to C-G (yielding a $tRNA^{fMet}$ variant referred to as "$tRNA^{fMet}$ M1") or mutations in other components of the anticodon stem decrease the efficiency of initiation, presumably through the disruption of interactions between the initiator tRNA and the ribosome[31]. Likewise, mutations of A1339, which weaken A-minor interactions between the ribosome and tRNA anticodon stem at this position, yield ribosomes with decreased translational activity (Fig. 3C)[28, 29]. Conversely, the 16S rRNA G1338A mutation, which leads to the formation of stronger type II A-minor interactions between the rRNA and $tRNA^{fMet}$ during initiation, yields ribosomes with higher translational activity than wild type but results in spurious initiation at non-start codons (Fig. 3D)[27]. This suggests that initiation may be tuned for an intermediate mix of efficiency and accuracy, requiring strong but not excessively tight interactions between $tRNA^{fMet}$ and the rRNA for rapid and high-fidelity initiation, with tighter interactions reducing accuracy and looser interactions reducing efficiency.

Following initiation, the ribosome must also maintain fidelity during the elongation cycle of translation through accurate selection of tRNAs. During tRNA selection, the 16S rRNA directly inspects the base pairing of the mRNA and tRNA in the A-site through the formation of A-minor interactions between nucleotides A1492/A1493 and the codon-anticodon helix[15, 33]. These nucleotides are components of 16S rRNA helix 44 (h44) and are typically oriented toward the interior of h44 at the decoding center of the ribosome. Cognate mRNA-tRNA pairings stabilize a conformation of A1492 and A1493 where they flip out of h44 to interact with the codon-anticodon helix minor groove, which serves as a signal permitting full accommodation of the tRNA into the ribosomal A site and subsequent incorporation of a new amino acid into the nascent polypeptide

[15, 34]. Miscoding errors, where the ribosome fails to reject a non-cognate tRNA during tRNA selection, can therefore result from stabilization of the flipped-out conformation of the decoding center nucleotides in the presence of a non-cognate mRNA-tRNA pairing[13, 18-20, 47]. Stabilization of this state is the primary function of aminoglycosides, natural product aminosugar antibiotics which bind h44 of the 16S rRNA and displace nucleotides A1492 and A1493, forcing them to occupy a flipped-out conformation and increasing the miscoding rate of the bacterial ribosome (Fig. 4)[13, 18-20, 47].

1.4: Aminoglycoside antibiotics disrupt bacterial translational fidelity

As potent disruptors of bacterial translation fidelity, aminoglycosides serve a crucial medical function as antibiotics of last resort, where they are used to treat complicated or chronic Gram-negative infections or infections which are resistant to treatment with other antibiotic classes[48, 49]. The presence of aminoglycosides in the environment via their production by certain bacterial species (*e.g.*, *Streptomyces* and *Micromonospora spp*.) and their use in both human and animal medical treatment presents selective pressures which encourage the development of resistance systems that protect the fidelity of bacterial translation[50-54]. These mechanisms include changes in cell membrane permeability to prevent aminoglycoside uptake, drug efflux using membrane spanning pumps, drug modification using aminoglycoside modifying enzymes, and target modification in the form of rRNA methylation (Fig. 5)[55, 56]. Aminoglycoside resistance rRNA methylations occur on the nucleobases of either G1405 or A1408 of 16S rRNA h44, each of which interacts with 4,6-deoxystreptamine (4,6-DOS) aminoglycosides, a common class of aminoglycosides containing the drugs kanamycin, gentamicin, and their derivatives[57, 58]. G1405 methylation is conferred by ArmA/Rmt family methyltransferases (RmtA through RmtH) and is sufficient to cause pan-resistance to 4,6-DOS aminoglycosides[59-62]. Conversely, 4,6-DOS aminoglycosides display a range of susceptibility to resistance via A1408 methylation (conferred

by the 16S rRNA methyltransferases NpmA and NpmB), with some aminoglycosides displaying only a small increase in minimum inhibitory concentration (MIC) in *E. coli* when A1408 is methylated while others have their activity nearly totally abolished[63, 64]. Given increasing prevalence of A1408 methylation-mediated aminoglycoside resistance in clinical bacterial isolates, understanding the features determining the susceptibility of 4,6-DOS aminoglycoside drugs to A1408 methylation mediated resistance will prove valuable for the rational improvement of aminoglycoside drugs.

1.5: Goals of this work

While prior studies have established the importance of RNA-RNA interactions between $tRNA^{fMet}$ and the 16S rRNA for proper selection of the initiator tRNA and that bacterial IF2 appears to rescue the efficiency and fidelity of initiation on non-canonical CUG start codons when these interactions are disrupted, the mechanism by which IF2 performs its quality control function remains unclear. Additionally, given that AUG, GUG, and UUG codons are used as canonical start codons for translation initiation in bacteria, it is unclear why bacteria have evolved to select CUG as a start codon extremely rarely. The study presented in Chapter 2 attempts provides on these outstanding questions by using high-resolution single-particle electron cryomicroscopy (cryo-EM) to determine the molecular structures of *E. coli* 70S ribosomes initiating translation using $tRNA^{fMet}$ M1 on AUG, GUG, UUG, and CUG start codons. Structures of 70S ICs assembled without initiation factors and containing each of the four NUG start codons (where N corresponds to any RNA nucleotide) allow the detection of any start codon-specific differences in interactions among $tRNA^{fMet}$, the 16S rRNA, and the mRNA start codon which would give rise to the previously observed apparent loss of fidelity during initiation with $tRNA^{fMet}$ M1 and a CUG start codon. Finally, a fifth cryo-EM structure of an enzymatically assembled 70S IC containing $tRNA^{fMet}$ M1, a CUG start codon, and IF2 permits determination of IF2-dependent structural changes in the IC which

give rise to its ability to maintain fidelity during initiation. These structures reveal that the interactions of $tRNA^{fMet}$ M1 with the 16S rRNA are weakened due to the tRNA's altered anticodon stem sequence, explaining its reduced ability to initiate translation compared to wild type $tRNA^{fMet}$. Additionally, no large-scale differences in the interaction of $tRNA^{fMet}$ M1 with the 16S rRNA were observed among complexes assembled with the four NUG start codons, suggesting that the tRNA-rRNA and tRNA-mRNA interactions do not engage in direct crosstalk with one another and that the efficiency of initiation is instead regulated by the strength of both sets of interactions independently. CUG codons interact the most weakly with the $tRNA^{fMet}$ anticodon among the four NUG start codons, potentially explaining why bacteria have evolved to use it for initiation only very rarely. Finally, the interaction of IF2 with $tRNA^{fMet}$ M1 during initiation positions the tRNA in a unique initiation orientation (called the P/I orientation) which allows 16S nucleotide G1338 to position itself more deeply in the tRNA minor groove when IF2 is bound compared to when it is absent. This strengthens the interaction of the tRNA with the ribosome and can explain the quality control function of IF2 during initiation.

Translation-targeting antibiotics are a critical element of modern medical practice, with aminoglycoside antibiotics serving as essential drugs of last resort for the treatment of severe and chronic bacterial infections. Aminoglycoside resistance through 16S rRNA modification presents a particularly pressing threat to this class of antibiotics, as it can confer resistance to a wide spectrum of aminoglycoside drugs. While *N7*-methylation of 16S nucleotide G1405 yields pan-resistance to the 4,6-DOS subclass of aminoglycosides (including the kanamycin, gentamicin, and sisomicin drug scaffolds), *N1*-methylation of 16S nucleotide A1408, an increasingly prevalent mode of resistance, yields a spectrum of resistance to 4,6-DOS aminoglycosides. If the chemical features which allow some 4,6-DOS aminoglycosides to effectively evade resistance conferred by m^1A1408 could be determined, these principles could be used to rationally improve

aminoglycoside design and preserve their efficacy as resistant infections become increasingly common; however, past studies have not systematically determined these chemical features.

The work presented in Chapter 3 of this dissertation uses a combined cryo-EM and molecular dynamics (MD) approach to systematically characterize drug features which improve aminoglycoside binding to bacterial ribosomes in the presence of the m^1A1408 resistance modification. First, drug features which improve the flexibility of 4,6-DOS aminoglycoside Ring I, which interacts with A1408 in unmethylated ribosomes, improve aminoglycoside binding in the presence of m^1A1408 as long as these features do not also abolish crucial interactions with the rRNA. Second, aminoglycosides possessing uncharged or bulky chemical groups at or near the 6' position of Ring I (*e.g.*, -OH, secondary amines, or additional aliphatic groups at the adjacent 7' position) tend to accommodate m^1A1408 better than drugs with 6'-NH_3^+ groups, which appear to be especially susceptible to electrostatic repulsion from the positively charged m^1A1408 base. Finally, the addition of chemical groups to Ring II of 4,6-DOS aminoglycosides can enhance binding in the presence of m1A1408 by anchoring drugs to h44.

Together, the studies presented in Chapters 2 and 3 of this dissertation contribute to the field's understanding of translational fidelity during initiation and elongation by further detailing the means by which disruption of crucial RNA-RNA interactions negatively affects the efficiency and accuracy of translation. Prior to the study presented in Chapter 2, no published bacterial ribosome structures existed in the literature showing how altering the sequence of the $tRNA^{fMet}$ anticodon stem (as in $tRNA^{fMet}$ M1) leads to decreases in the efficiency and (apparent) accuracy of initiation. These structures show how swapping the sequence of the tRNA 30-40 base pair weakens interactions with the ribosome, which is consistent with prior biochemical studies of $tRNA^{fMet}$ M1 and of 16S rRNA variants with substitutions at positions G1338 and A1339. Additionally, the structure of an IF2-bound 70S IC initiating translation on a CUG codon reveals that IF2 positions 16S rRNA nucleotide G1338 more deeply within the tRNA minor groove, strengthening the tRNA-

ribosome interactions and explaining its quality control function. Finally, our results suggest that tRNA-ribosome and tRNA-mRNA interactions independently control the efficiency of initiation rather than engaging in direct crosstalk. This can explain why CUG is used only rarely as a start codon in bacteria, as prior biochemical studies have shown that CUG interacts with $tRNA^{fMet}$ more weakly than AUG, GUG, or UUG start codons, leading to lower thermodynamic and kinetic stability in 30S and 70S ICs. The study presented in Chapter 3 provides a series of systematic aminoglycoside design principles intended to maximize aminoglycoside binding to ribosomes in the presence of the m^1A1408 resistance modification. Our cryo-EM structures and MD simulations allow for the correlation of differences in aminoglycoside structure, often at a single position, to differences in observed MICs in the presence of m^1A1408-modified ribosomes. These principles may be used in the rational improvement of aminoglycoside design by narrowing the space of drug structures to be produced and tested against m^1A1408-expressing pathogens to the structures most likely to have their antibiotic activity maintained in the presence of the resistance methylation.

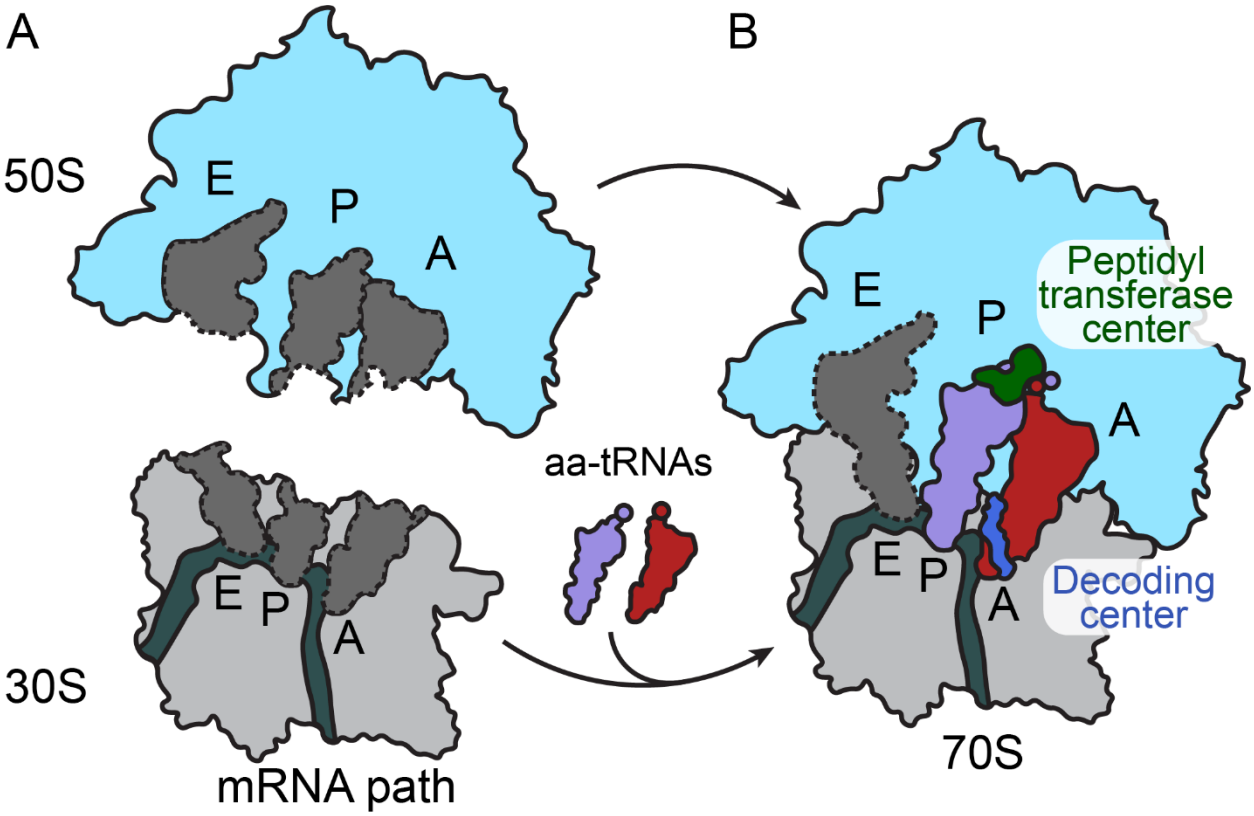

Figure 1. Overall structure and functional centers of the bacterial ribosome. A). The bacterial ribosome is composed of two ribonucleoprotein subunits: a large (50S, light blue) subunit and a small (30S, light gray) subunit. The mRNA path (slate gray) resides on the small subunit, and each subunit has partially-formed tRNA binding sites (dark gray, dashed outline). B). Upon assembly of the complete (70S) ribosome, tRNAs may bind at the A site (red) to participate in peptidyl transfer with the tRNA bound at the P site (purple). A-site tRNA selection is performed through inspection of the codon-anticodon pairing by the ribosome's decoding center (dark blue), composed of 16S rRNA nucleotides G530, A1492, and A1493, along with 23S rRNA nucleotide A1913. The ribosome's peptidyl transferase center (green) catalyzes extension of the nascent polypeptide through transfer of the nascent peptide from the P-site peptidyl-tRNA to the A-site aminoacyl-tRNA.

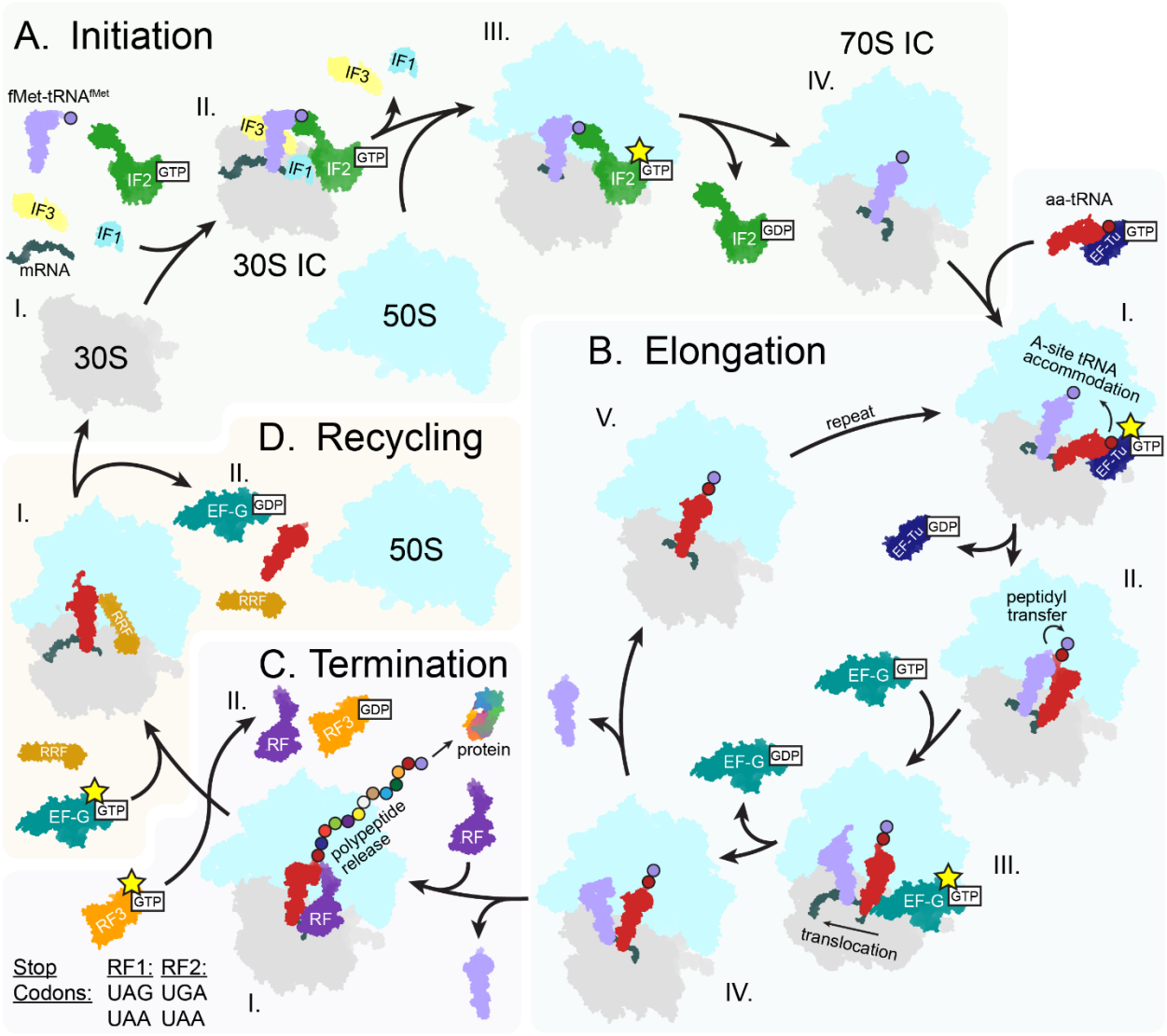

Figure 2. Bacterial translation is a coordinated, multi-step cycle directing the synthesis of new proteins. A). (I) To initiate translation, a free 30S (small) ribosomal subunit must associate an with mRNA molecule, the dedicated initiator tRNA fMet-tRNA^{fMet}, and the three initiation factors IF1, IF2, and IF3 to form the (II) 30S initiation complex (30S IC). IF1 and IF3 then dissociate and IF2 recruits the 50S (large) ribosomal subunit (III). This is followed by GTP hydrolysis by IF2 and its subsequent dissociation from the ribosome, yielding the mature 70S initiation complex (70S IC, IV). B). A 70S IC competent for elongation can receive aa-tRNA·EF-Tu·GTP ternary complexes at its A site (I), with tRNA-mRNA pairing being inspected by the decoding center of the 30S subunit. Cognate tRNAs are fully accommodated onto the ribosome and undergo peptidyl

transfer (II), receiving fMet from the P-site fMet-tRNA^{fMet} and extending the nascent polypeptide chain by one amino acid. The elongation factor EF-G translocates the two tRNAs into their adjacent tRNA binding sites (III; P→E; A→P) and dissociates from the ribosome following GTP hydrolysis, leaving a 70S complex containing E- and P-site tRNAs and an empty A site (IV). The deacylated E-site tRNA exits the ribosome and the 70S complex (V) repeats the elongation cycle to extend the nascent polypeptide until a stop codon is presented at its A site. C). Upon presentation of a stop codon at the A site, one of two release factors (RF1 for UGA and UAA stop codons; RF2 for UGA and UAA stop codons) binds the ribosomal A site (I) and releases the polypeptide chain from the P-site tRNA. The GTPase release factor RF3 binds the ribosome and dissociates RF1/2 from the ribosomal A site, then exits the ribosome following GTP hydrolysis (II). D). 70S complexes from which polypeptides have been released are recycled into their constituent subunits in a manner catalyzed by the recycling factor RRF and EF-G (I), yielding GDP-bound EF-G, free tRNA and RRF, and enabling the ribosomal subunits to participate in new rounds of translation initiation.

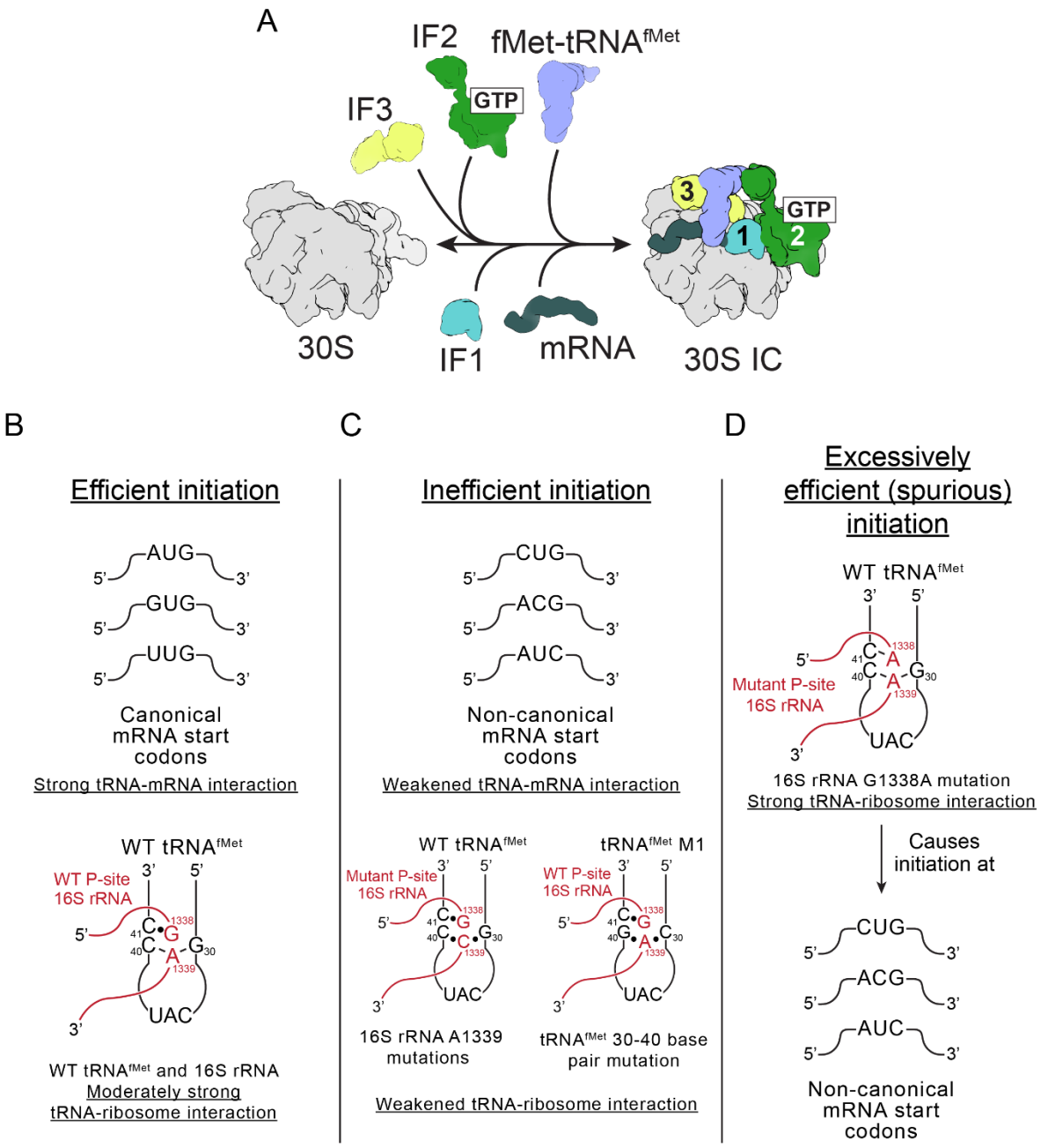

Figure 3. Translation initiation efficiency and fidelity are regulated by the strength of tRNA-mRNA and tRNA-ribosome interactions. A). During translation initiation in bacteria, the ribosomal small (30S) subunit must reversibly bind an mRNA molecule, the dedicated initiator tRNA (fMet-tRNA^{fMet}), and three initiation factors (IF1, IF2, and IF3) to form the 30S initiation complex (30S IC), with components of the 30S IC able to bind without a required order. The strength of interactions between fMet-tRNA^{fMet} and both the mRNA and 30S subunit affects the

stability of the 30S IC, which consequently affects the efficiency of initiation and accuracy of mRNA start codon selection. B). Efficient and accurate translation initiation is achieved by interaction of $tRNA^{fMet}$ with any of the three canonical bacterial start codons (AUG, GUG, and UUG) and by moderately strong interaction of wild type $tRNA^{fMet}$ with wild type 16S rRNA at the ribosomal P site, which makes two conserved A-minor interactions with the tRNA anticodon stem (a suboptimal interaction between 16S nucleotide G1338 and $tRNA^{fMet}$ nucleotide C41 and an optimally strong interaction between 16S nucleotide A1339 and the tRNA G30-C40 base pair). C). Initiation efficiency is diminished on mRNA molecules utilizing non-canonical start codons such as CUG, ACG, and AUC, which exhibit weakened pairing with $tRNA^{fMet}$. Mutating conserved 16S nucleotide A1339 or flipping the $tRNA^{fMet}$ G30-C40 base pair to C30-G40 (known as $tRNA^{fMet}$ M1) also decreases initiation efficiency by rendering the A-minor interaction between the 16S position 1339 nucleotide and the $tRNA^{fMet}$ 30-40 base pair suboptimal. D). Mutating conserved 16S nucleotide G1338 to A renders its interaction with $tRNA^{fMet}$ nucleotide C41 optimally strong, increasing the efficiency of initiation but also resulting in spurious initiation at non-canonical start codons including CUG, ACG, and AUC.

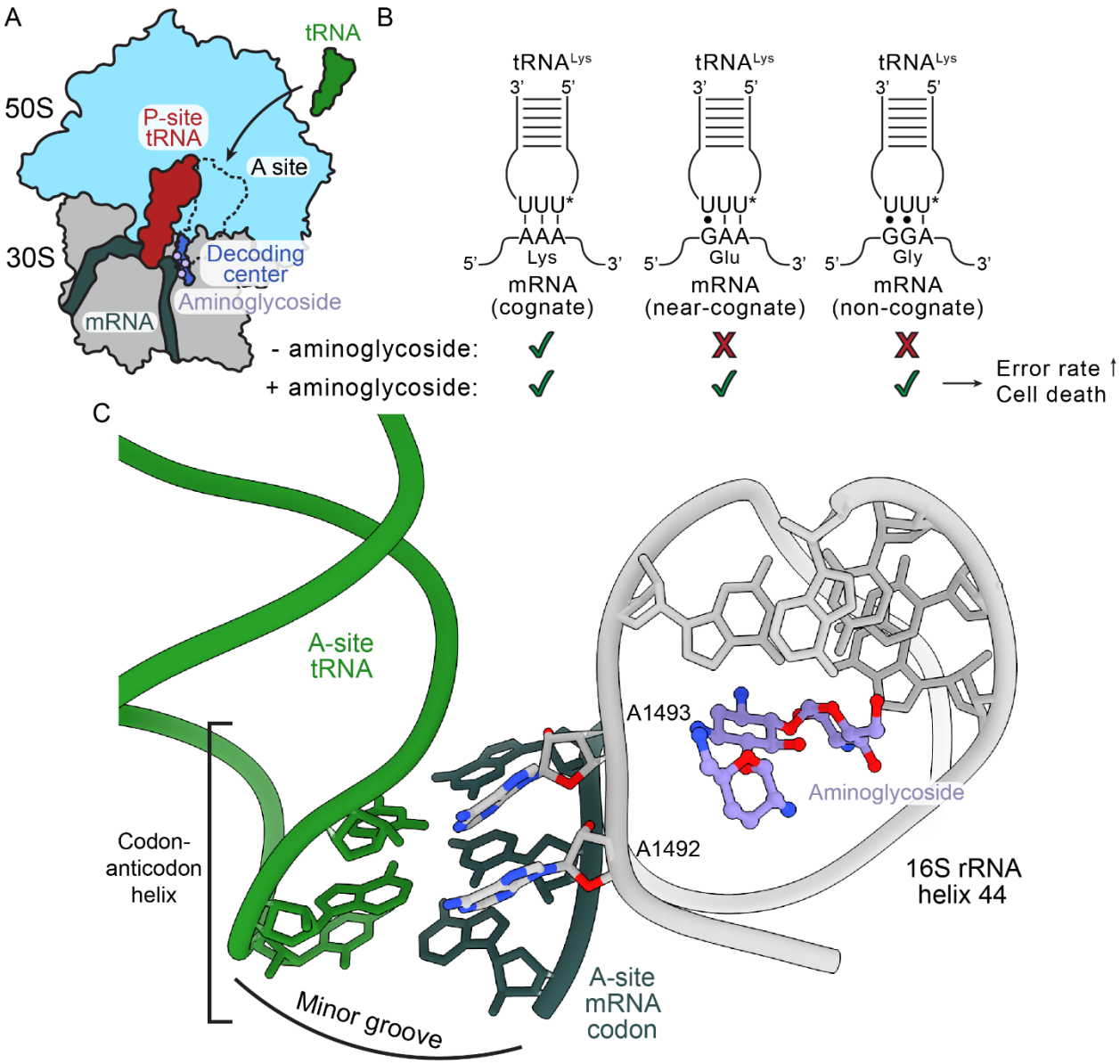

Figure 4. Aminoglycoside antibiotics disrupt translation by increasing the error rate of decoding. A). Aminoglycoside antibiotics (purple) bind the small (30S) subunit of bacterial ribosomes at the ribosome's decoding center (dark blue; 16S rRNA nucleotides G530, A1492 and A1493, 23S rRNA nucleotide A1913), which is involved in the selection of new aminoacyl-tRNAs at the ribosomal A site based on their interactions with the messenger RNA (slate gray). B). In the absence of aminoglycosides, ribosomes will typically select only cognate tRNAs (left) corresponding to the mRNA codon presented at the ribosomal A site (e.g., $tRNA^{Lys}$, which can decode AAA mRNA codons encoding the amino acid lysine). In the presence of aminoglycosides,

the error rate of the decoding center is increased, permitting the accommodation of near-cognate (middle) and non-cognate (right) tRNA-mRNA pairings, leading to misincorporation of amino acids into nascent polypeptides and eventual cell death (U* = 5-methylaminomethyl-2-thiouridine). C.) Aminoglycoside binding at 16S rRNA h44 displaces 16S nucleotides A1492 and A1493 into the minor groove of the codon-anticodon helix, a conformation of these nucleotides which typically signals a correct mRNA-tRNA pairing. This decreases the ability of the ribosome to discriminate against near- or non-cognate tRNA-mRNA pairings, causing miscoding errors.

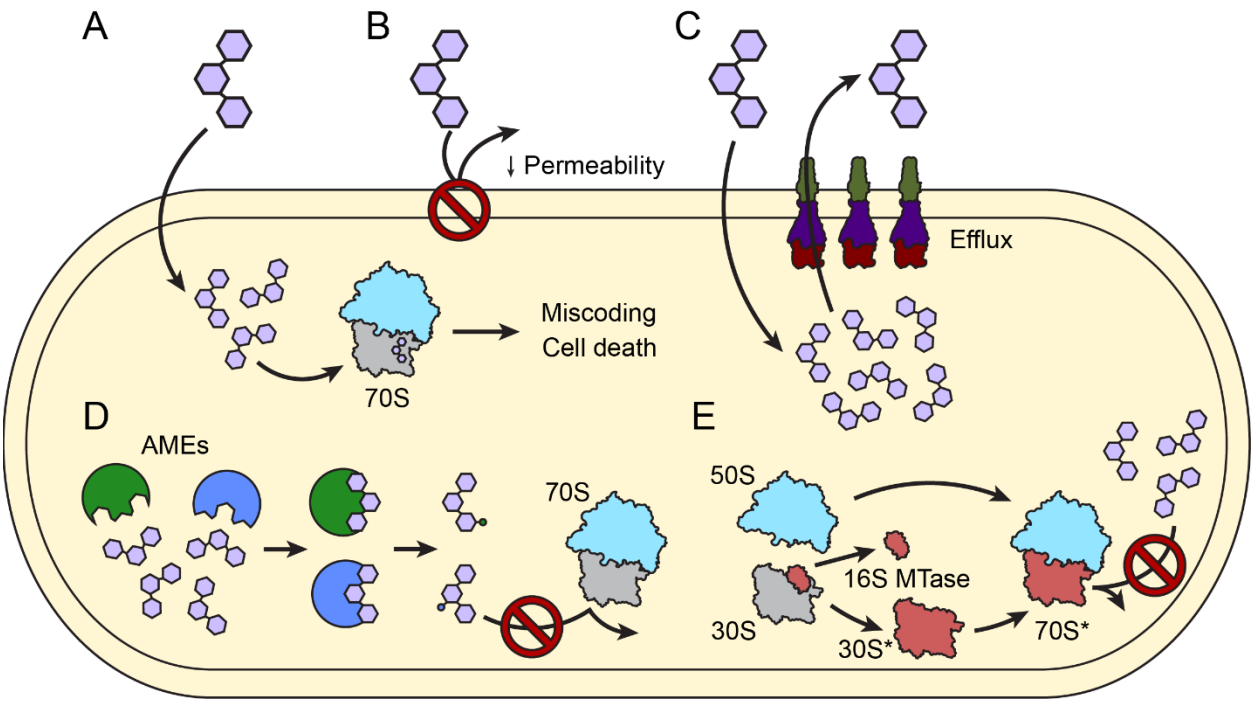

Figure 5. Mechanisms of aminoglycoside resistance. A). In the absence of resistance systems, aminoglycoside antibiotics are taken up into bacterial cells, where they bind the small subunit of translating ribosomes, inducing miscoding and subsequent cell death. B). Reductions in membrane permeability prevent aminoglycosides from entering cells preventing their bactericidal activity. C). Expression of membrane-spanning efflux systems can allow bacteria to remove aminoglycosides which cross their membranes into the cytoplasm. D). Antibiotic modification by aminoglycoside modifying enzymes (AMEs) prevents aminoglycosides from binding to their target on the small ribosomal subunit. AMEs can deposit modifications on a variety of locations on the aminoglycoside scaffold, preventing crucial interactions with 16S rRNA helix 44. E). Target modification at 16S rRNA nucleotides G1405 or A1408 by resistance-associated 16S rRNA methyltransferases yields aminoglycoside-resistant ribosomes (30S*, 70S*) which fail to make important interactions for antibiotic binding, often yielding broad resistance to many aminoglycosides of a similar class or chemical scaffold.

References

1. Rodnina MV. Translation in Prokaryotes. LID - 10.1101/cshperspect.a032664 [doi] LID - a032664(1943-0264 (Electronic)).
2. Davis JA-O, Williamson JA-OX. Structure and dynamics of bacterial ribosome biogenesis. LID - 10.1098/rstb.2016.0181 [doi] LID - 20160181(1471-2970 (Electronic)).
3. Berg MA-O, Brandl CA-O. Transfer RNAs: diversity in form and function(1555-8584 (Electronic)).
4. Rodnina MV. Decoding and Recoding of mRNA Sequences by the Ribosome. Annual Review of Biophysics. 2023;52(Volume 52, 2023):161-82. doi: https://doi.org/10.1146/annurev-biophys-101922-072452.
5. Liu Q, Fredrick K. Intersubunit Bridges of the Bacterial Ribosome. Journal of Molecular Biology. 2016;428(10, Part B):2146-64. doi: https://doi.org/10.1016/j.jmb.2016.02.009.
6. Kaushal PS, Sharma MR, Agrawal RK. The 55S mammalian mitochondrial ribosome and its tRNA-exit region(1638-6183 (Electronic)).
7. Leung EK, Suslov N Fau - Tuttle N, Tuttle N Fau - Sengupta R, Sengupta R Fau - Piccirilli JA, Piccirilli JA. The mechanism of peptidyl transfer catalysis by the ribosome(1545-4509 (Electronic)).
8. Xu B, Liu L, Song G. Functions and Regulation of Translation Elongation Factors(2296-889X (Print)).
9. Arenz S, Ramu H, Gupta P, Berninghausen O, Beckmann R, Vázquez-Laslop N, Mankin AS, Wilson DN. Molecular basis for erythromycin-dependent ribosome stalling during translation of the ErmBL leader peptide. Nature Communications. 2014;5(1):3501. doi: 10.1038/ncomms4501.
10. Sothiselvam S, Liu B, Han W, Ramu H, Klepacki D, Atkinson GC, Brauer A, Remm M, Tenson T, Schulten K, Vázquez-Laslop N, Mankin AS. Macrolide antibiotics allosterically predispose the ribosome for translation arrest. Proceedings of the National Academy of Sciences. 2014;111(27):9804-9. doi: 10.1073/pnas.1403586111.
11. Vázquez-Laslop N, Klepacki D, Mulhearn DC, Ramu H, Krasnykh O, Franzblau S, Mankin AS. Role of antibiotic ligand in nascent peptide-dependent ribosome stalling. Proceedings of the National Academy of Sciences. 2011;108(26):10496-501. doi: 10.1073/pnas.1103474108.
12. Vázquez-Laslop N, Mankin AS. Context-Specific Action of Ribosomal Antibiotics(1545-3251 (Electronic)).
13. Lin J, Zhou D, Steitz TA, Polikanov YS, Gagnon MG. Ribosome-Targeting Antibiotics: Modes of Action, Mechanisms of Resistance, and Implications for Drug Design. Annu Rev Biochem. 2018;87(1545-4509 (Electronic)):451-78. Epub 20180323. doi: 10.1146/annurev-biochem-062917-011942. PubMed PMID: 29570352; PMCID: PMC9176271.
14. Rodnina MA-O, Fischer NA-O, Maracci C, Stark H. Ribosome dynamics during decoding. LID - 10.1098/rstb.2016.0182 [doi] LID - 20160182(1471-2970 (Electronic)).
15. Zeng X, Chugh J, Casiano-Negroni A, Al-Hashimi HM, Brooks CL, 3rd. Flipping of the ribosomal A-site adenines provides a basis for tRNA selection. J Mol Biol. 2014;426(19):3201-13. Epub 20140509. doi: 10.1016/j.jmb.2014.04.029. PubMed PMID: 24813122; PMCID: PMC4150856.
16. Ogle JM, Brodersen DE, Clemons WM, Jr., Tarry MJ, Carter AP, Ramakrishnan V. Recognition of cognate transfer RNA by the 30S ribosomal subunit. Science. 2001;292(5518):897-902. doi: 10.1126/science.1060612. PubMed PMID: 11340196.
17. Noller HF. Biochemical characterization of the ribosomal decoding site. Biochimie. 2006;88(8):935-41. Epub 20060427. doi: 10.1016/j.biochi.2006.04.006. PubMed PMID: 16730404.

18. Demirci H, Murphy Ft, Murphy E, Gregory ST, Dahlberg AE, Jogl G. A structural basis for streptomycin-induced misreading of the genetic code. Nat Commun. 2013;4:1355. doi: 10.1038/ncomms2346. PubMed PMID: 23322043; PMCID: PMC3552334.
19. Spickler C, Brunelle M-N, Brakier-Gingras L. Streptomycin binds to the decoding center of 16 S ribosomal RNA11Edited by M. Gottesman. Journal of Molecular Biology. 1997;273(3):586-99. doi: https://doi.org/10.1006/jmbi.1997.1323.
20. Jerinic O, Joseph S. Conformational Changes in the Ribosome Induced by Translational Miscoding Agents. Journal of Molecular Biology. 2000;304(5):707-13. doi: https://doi.org/10.1006/jmbi.2000.4269.
21. Gualerzi CO, Pon CL. Initiation of mRNA translation in bacteria: structural and dynamic aspects. Cell Mol Life Sci. 2015;72(22):4341-67. Epub 20150811. doi: 10.1007/s00018-015-2010-3. PubMed PMID: 26259514; PMCID: PMC4611024.
22. Laursen BS, Sørensen Hp Fau - Mortensen KK, Mortensen Kk Fau - Sperling-Petersen HU, Sperling-Petersen HU. Initiation of protein synthesis in bacteria(1092-2172 (Print)).
23. Wen JA-O, Kuo SA-O, Chou HA-O. The diversity of Shine-Dalgarno sequences sheds light on the evolution of translation initiation(1555-8584 (Electronic)).
24. Milón P, Maracci C, Filonava L, Gualerzi CO, Rodnina MV. Real-time assembly landscape of bacterial 30S translation initiation complex. Nature Structural & Molecular Biology. 2012;19(6):609-15. doi: 10.1038/nsmb.2285.
25. Sprink T, Ramrath DJF, Yamamoto H, Yamamoto K, Loerke J, Ismer J, Hildebrand PW, Scheerer P, Bürger J, Mielke T, Spahn CMT. Structures of ribosome-bound initiation factor 2 reveal the mechanism of subunit association. Science Advances. 2016;2(3):e1501502. doi: doi:10.1126/sciadv.1501502.
26. Milón P, Rodnina MV. Kinetic control of translation initiation in bacteria. Critical Reviews in Biochemistry and Molecular Biology. 2012;47(4):334-48. doi: 10.3109/10409238.2012.678284.
27. Lancaster L, Noller HF. Involvement of 16S rRNA Nucleotides G1338 and A1339 in Discrimination of Initiator tRNA. Molecular Cell. 2005;20(4):623-32. doi: https://doi.org/10.1016/j.molcel.2005.10.006.
28. ABDI NM, FREDRICK K. Contribution of 16S rRNA nucleotides forming the 30S subunit A and P sites to translation in Escherichia coli. RNA. 2005;11(11):1624-32. doi: 10.1261/rna.2118105.
29. Qin D, Abdi NM, Fredrick K. Characterization of 16S rRNA mutations that decrease the fidelity of translation initiation. RNA. 2007;13(12):2348-55. doi: 10.1261/rna.715307.
30. Mandal N, Mangroo D, Dalluge JJ, McCloskey JA, RajBhandary UL. Role of the three consecutive G:C base pairs conserved in the anticodon stem of initiator tRNAs in initiation of protein synthesis in Escherichia coli. RNA. 1996;2(5):473-82.
31. Roy B, Liu Q, Shoji S, Fredrick K. IF2 and unique features of initiator tRNAfMet help establish the translational reading frame. RNA Biology. 2018;15(4-5):604-13. doi: 10.1080/15476286.2017.1379636.
32. Hussain T, Llácer JL, Wimberly BT, Kieft JS, Ramakrishnan V. Large-Scale Movements of IF3 and tRNA during Bacterial Translation Initiation. Cell. 2016;167(1):133-44.e13. doi: 10.1016/j.cell.2016.08.074.
33. Fislage M, Zhang J, Brown ZP, Mandava CS, Sanyal S, Ehrenberg M, Frank J. Cryo-EM shows stages of initial codon selection on the ribosome by aa-tRNA in ternary complex with GTP and the GTPase-deficient EF-TuH84A. Nucleic Acids Research. 2018;46(11):5861-74. doi: 10.1093/nar/gky346.
34. Khade PK, Shi X, Joseph S. Steric Complementarity in the Decoding Center Is Important for tRNA Selection by the Ribosome. Journal of Molecular Biology. 2013;425(20):3778-89. doi: https://doi.org/10.1016/j.jmb.2013.02.038.

35. Agirrezabala X, Lei J, Brunelle JL, Ortiz-Meoz RF, Green R, Frank J. Visualization of the hybrid state of tRNA binding promoted by spontaneous ratcheting of the ribosome. Mol Cell. 2008;32(2):190-7. doi: 10.1016/j.molcel.2008.10.001. PubMed PMID: 18951087; PMCID: PMC2614368.
36. Walker SE, Shoji S, Pan D, Cooperman BS, Fredrick K. Role of hybrid tRNA-binding states in ribosomal translocation. Proceedings of the National Academy of Sciences. 2008;105(27):9192-7. doi: doi:10.1073/pnas.0710146105.
37. Ling C, Ermolenko DN. Structural insights into ribosome translocation. Wiley Interdiscip Rev RNA. 2016;7(5):620-36. Epub 20160427. doi: 10.1002/wrna.1354. PubMed PMID: 27117863; PMCID: PMC4990484.
38. Zhou J, Lancaster L, Donohue JP, Noller HF. Crystal Structures of EF-G–Ribosome Complexes Trapped in Intermediate States of Translocation. Science. 2013;340(6140):1236086. doi: doi:10.1126/science.1236086.
39. Carbone CE, Loveland AB, Gamper HB, Hou Y-M, Demo G, Korostelev AA. Time-resolved cryo-EM visualizes ribosomal translocation with EF-G and GTP. Nature Communications. 2021;12(1):7236. doi: 10.1038/s41467-021-27415-0.
40. Petrychenko VA-O, Peng BA-O, de APSACA-O, Peske FA-O, Rodnina MA-O, Fischer NA-O. Structural mechanism of GTPase-powered ribosome-tRNA movement(2041-1723 (Electronic)).
41. Graf M, Huter P, Maracci C, Peterek M, Rodnina MV, Wilson DN. Visualization of translation termination intermediates trapped by the Apidaecin 137 peptide during RF3-mediated recycling of RF1. Nature Communications. 2018;9(1):3053. doi: 10.1038/s41467-018-05465-1.
42. Shaw JJ, Green R. Two distinct components of release factor function uncovered by nucleophile partitioning analysis(1097-2765 (Print)).
43. Savelsbergh A, Rodnina MV, Wintermeyer W. Distinct functions of elongation factor G in ribosome recycling and translocation. RNA. 2009;15(5):772-80. doi: 10.1261/rna.1592509.
44. Hecht A, Glasgow J, Jaschke PR, Bawazer LA, Munson MS, Cochran JR, Endy D, Salit M. Measurements of translation initiation from all 64 codons in E. coli. Nucleic Acids Research. 2017;45(7):3615-26. doi: 10.1093/nar/gkx070.
45. Petrelli D, LaTeana A Fau - Garofalo C, Garofalo C Fau - Spurio R, Spurio R Fau - Pon CL, Pon Cl Fau - Gualerzi CO, Gualerzi CO. Translation initiation factor IF3: two domains, five functions, one mechanism?(0261-4189 (Print)).
46. Singh JA-O, Mishra RK, Ayyub SA-O, Hussain TA-O, Varshney UA-O. The initiation factor 3 (IF3) residues interacting with initiator tRNA elbow modulate the fidelity of translation initiation and growth fitness in Escherichia coli(1362-4962 (Electronic)).
47. Sanbonmatsu KY. Energy landscape of the ribosomal decoding center. Biochimie. 2006;88(8):1053-9. Epub 20060726. doi: 10.1016/j.biochi.2006.06.012. PubMed PMID: 16905237.
48. Safi KH, Damiani JM, Sturza J, Nasr SZ. Extended-Interval Aminoglycoside Use in Cystic Fibrosis Exacerbation in Children and Young Adults:A Prospective Quality Improvement Project. Global Pediatric Health. 2016;3:2333794X16635464. doi: 10.1177/2333794x16635464. PubMed PMID: 27336007.
49. Ratjen F, Brockhaus F, Angyalosi G. Aminoglycoside therapy against Pseudomonas aeruginosa in cystic fibrosis: a review. J Cyst Fibros. 2009;8(6):361-9. Epub 20090910. doi: 10.1016/j.jcf.2009.08.004. PubMed PMID: 19747887.
50. Wachino J, Arakawa Y. Exogenously acquired 16S rRNA methyltransferases found in aminoglycoside-resistant pathogenic Gram-negative bacteria: an update. Drug Resist Updat. 2012;15(3):133-48. Epub 20120604. doi: 10.1016/j.drup.2012.05.001. PubMed PMID: 22673098.

51. Nowacka-Kozak E, Gajda A, Gbylik-Sikorska M. Analysis of Aminoglycoside Antibiotics: A Challenge in Food Control. Molecules. 2023;28(12). Epub 20230607. doi: 10.3390/molecules28124595. PubMed PMID: 37375150; PMCID: PMC10301657.
52. Deng YT, Zeng ZL, Tian W, Yang T, Liu JH. Prevalence and characteristics of rmtB and qepA in Escherichia coli isolated from diseased animals in China. Front Microbiol. 2013;4:198. Epub 20130715. doi: 10.3389/fmicb.2013.00198. PubMed PMID: 23874331; PMCID: PMC3710952.
53. Matković B, Piendl W, Böck A. Ribosomal resistance as a wide-spread self-defence mechanism in aminoglycoside-producing Micromonospora species. FEMS Microbiology Letters. 1984;24(2-3):273-6. doi: 10.1111/j.1574-6968.1984.tb01318.x.
54. Hotta K, Ishikawa J, Ogata T, Mizuno S. Secondary aminoglycoside resistance in aminoglycoside-producing strains of Streptomyces. Gene. 1992;115(1):113-7. doi: https://doi.org/10.1016/0378-1119(92)90548-4.
55. Garneau-Tsodikova S, Labby KJ. Mechanisms of Resistance to Aminoglycoside Antibiotics: Overview and Perspectives. Medchemcomm. 2016;7(1):11-27. Epub 20150921. doi: 10.1039/c5md00344j. PubMed PMID: 26877861; PMCID: PMC4752126.
56. Ramirez MS, Tolmasky ME. Aminoglycoside modifying enzymes(1532-2084 (Electronic)).
57. Doi Y, Arakawa Y. 16S Ribosomal RNA Methylation: Emerging Resistance Mechanism against Aminoglycosides. Clinical Infectious Diseases. 2007;45(1):88-94. doi: 10.1086/518605.
58. Witek MA, Conn GL. Expansion of the aminoglycoside-resistance 16S rRNA (m1A1408) methyltransferase family: Expression and functional characterization of four hypothetical enzymes of diverse bacterial origin. Biochimica et Biophysica Acta (BBA) - Proteins and Proteomics. 2014;1844(9):1648-55. doi: https://doi.org/10.1016/j.bbapap.2014.06.012.
59. Srinivas P, Nosrati M, Zelinskaya N, Dey D, Comstock LR, Dunham CM, Conn GL. 30S subunit recognition and G1405 modification by the aminoglycoside-resistance 16S ribosomal RNA methyltransferase RmtC. Proceedings of the National Academy of Sciences. 2023;120(25):e2304128120.
60. Doi Y, Wachino J, Arakawa Y. Nomenclature of plasmid-mediated 16S rRNA methylases responsible for panaminoglycoside resistance. Antimicrob Agents Chemother. 2008;52(6):2287-8. Epub 20080331. doi: 10.1128/aac.00022-08. PubMed PMID: 18378718; PMCID: PMC2415770.
61. Galimand M, Courvalin P, Lambert T. RmtF, a New Member of the Aminoglycoside Resistance 16S rRNA N7 G1405 Methyltransferase Family. Antimicrobial Agents and Chemotherapy. 2012;56(7):3960-2. doi: doi:10.1128/aac.00660-12.
62. Galimand M, Courvalin P, Lambert T. Plasmid-mediated high-level resistance to aminoglycosides in Enterobacteriaceae due to 16S rRNA methylation. Antimicrob Agents Chemother. 2003;47(8):2565-71. doi: 10.1128/aac.47.8.2565-2571.2003. PubMed PMID: 12878520; PMCID: PMC166065.
63. Kanazawa H, Baba F, Koganei M, Kondo J. A structural basis for the antibiotic resistance conferred by an N1-methylation of A1408 in 16S rRNA. Nucleic Acids Res. 2017;45(21):12529-35. doi: 10.1093/nar/gkx882. PubMed PMID: 29036479; PMCID: PMC5716097.
64. Wachino J, Shibayama K, Kurokawa H, Kimura K, Yamane K, Suzuki S, Shibata N, Ike Y, Arakawa Y. Novel plasmid-mediated 16S rRNA m1A1408 methyltransferase, NpmA, found in a clinically isolated Escherichia coli strain resistant to structurally diverse aminoglycosides. Antimicrob Agents Chemother. 2007;51(12):4401-9. Epub 20070917. doi: 10.1128/aac.00926-07. PubMed PMID: 17875999; PMCID: PMC2168023.

Chapter 2:

Structural analysis of noncanonical translation initiation complexes

Jacob M. Mattingly[1,2], Ha An Nguyen[1], Bappaditya Roy[3], Kurt Fredrick[3] and Christine M. Dunham[1,*]

[1]Department of Chemistry, Emory University, Atlanta, GA, USA
[2]Graduate Program in Biochemistry, Cell and Developmental Biology, Emory University, Atlanta, GA, USA
[3]Department of Microbiology and Center for RNA Biology, The Ohio State University, Columbus, Ohio, USA

Data deposition: Atomic coordinates, and structure factors have been deposited in the Protein Data Bank, www.pdb.org and Electron Microscopy Data Bank (EMDB): (PDB codes 9AX7, 9AX8, 9CG5, 9CG6, 9CG7; EMDB codes EMD-43929, EMD-43930, EMD-45569, EMD-45572, EMD-45573)

Key words: protein synthesis**,** translation initiation, $tRNA^{fMet}$, A-minor motif, 16S rRNA

This work was originally published in the *Journal of Biological Chemistry*. JM determined cryo-EM structures and assembled figures. JM, HAN, and CD wrote and edited the manuscript. BR and KF edited and provided feedback on the manuscript.

ABSTRACT

Translation initiation is a highly regulated, multi-step process which is critical for efficient and accurate protein synthesis. In bacteria, initiation begins when mRNA, initiation factors, and a dedicated initiator fMet-tRNA^{fMet} bind the small (30S) ribosomal subunit. Specific binding of fMet-tRNA^{fMet} in the peptidyl (P) site is mediated by the inspection of the fMet moiety by initiation factor IF2 and of three conserved G-C base pairs in the tRNA anticodon stem by the 30S head domain. Tandem A-minor interactions form between 16S ribosomal RNA nucleotides A1339 and G1338 and tRNA base pairs G30-C40 and G29-C41, respectively. Swapping the G30-C40 pair of tRNA^{fMet} with C-G reduces discrimination against the noncanonical start codon CUG *in vitro*, suggesting crosstalk between gripping of the anticodon stem and recognition of the start codon. Here, we solved electron cryomicroscopy structures of *E. coli* 70S initiation complexes containing an fMet-tRNA^{fMet} G30-C40 variant paired to noncanonical CUG start codon, in the presence or absence of IF2 and the non-hydrolyzable GTP analog GDPCP, alongside structures of 70S initiation complexes containing this tRNA^{fMet} variant paired to the canonical bacterial start codons AUG, GUG, and UUG. We find that the M1 mutation weakens A-minor interactions between tRNA^{fMet} and 16S nucleotides A1339 and G1338, with IF2 strengthening the interaction of G1338 with the tRNA minor groove. These structures suggest how even slight changes to the recognition of the fMet-tRNA^{fMet} anticodon stem by the ribosome can impact start codon selection.

INTRODUCTION

Protein synthesis is a highly dynamic and delicately coordinated process involving the ribosome, mRNA, tRNAs and many translation factors. In bacteria, the start of translation (initiation) is generally the rate-limiting step that determines the translation efficiency of an mRNA (1). There are two major steps in initiation. The first step is the assembly of a 30S initiation complex (30S IC), involving base-pairing of the dedicated initiator tRNA, *N*-formyl-methionyl-tRNA^{fMet} (fMet-tRNA^{fMet}), with the mRNA start codon in the peptidyl (P) site, accompanied by three initiation factors (IF1, IF2, IF3) (Fig. 1A). The second step involves the recruitment of the 50S ribosomal subunit, GTP hydrolysis by IF2, and dissociation of all three IFs to form a 70S IC, ready for elongation (2). The IFs act synergistically to regulate both the kinetics and fidelity of these steps (reviewed in (3,4)). The GTPase IF2 ensures the correct selection of fMet-tRNA^{fMet} through recognition of the *N*-formyl moiety on the methionyl group at the tRNA acceptor end. IF2 mediates recruitment of the 50S ribosomal subunit to form the 70S IC, and its subsequent dissociation is driven by GTP hydrolysis (5-9). IF3 prevents the premature joining of the 50S subunit and allows for accurate start codon selection, while IF1 augments the activities of IF2 and IF3 (10).

In many bacteria, translation initiation entails recognition of a purine-rich mRNA region known as the Shine-Dalgarno (SD) sequence, located 7-10 nucleotides upstream of the AUG start codon of the mRNA (11). During initiation, the mRNA SD sequence pairs to the complementary anti-SD (ASD) sequence located at the 3' end of the 16S ribosomal RNA (rRNA) of the 30S subunit. Formation of this SD-ASD helix helps to position the start codon in the P site (12,13). The dedicated initiator tRNA^{fMet} contains distinctive features that specify its use in initiation rather than elongation (14). tRNA^{fMet} is aminoacylated with methionine and then formylated to yield *N*-formyl-methionyl-tRNA^{fMet} (fMet-tRNA^{fMet}). Formylation depends on a unique C1•A72 base pair in the acceptor stem of tRNA^{fMet} and is critical for IF2 recognition (5,15,16). tRNA^{fMet} also has three conserved G-C base pairs (G29-C41, G30-C40, and G31-C39) in the

anticodon stem that are important for P-site binding and efficient initiation *in vivo* (Fig. 1B) (17-21).

AUG, GUG, and UUG are considered canonical start codons in bacteria, accounting for 82%, 14%, and 4% of natural start codons, respectively, in a set of 69 representative genomes (22). The CAU anticodon sequence of $tRNA^{fMet}$ forms a codon-anticodon pairing with the AUG start codon. First-position mismatches, *e.g.*, between $tRNA^{fMet}$ and GUG and UUG start codons, are tolerated during initiation, in contrast to decoding that occurs in the A site (23,24). In the A site, codon-anticodon base pairing is directly probed by 16S rRNA nucleotides for selection of the correct tRNA. After peptidyl transfer and movement of the tRNA to the P site, the codon-anticodon helix of the tRNA is minimally inspected and instead the 16S rRNA that surrounds the P-site tRNA grips its anticodon stem to ensure its correct positioning (13,17,25,26). The gripping of the peptidyl-tRNA by the ribosome is critical for mRNA reading frame maintenance (27,28). Interactions of the ribosomal P site with the tRNA include 16S rRNA nucleotides m^2G966 and C1400 that pack beneath the third nucleotide of the anticodon (nucleotide 34; anticodon nucleotides are numbered 34, 35, 36) and A790, which contacts the tRNA backbone at nucleotide position 38. Conserved 16S nucleotides A1339 and G1338 of the 30S head domain form tandem type I and type II A-minor interactions with base pairs 30-40 and 29-41 of the tRNA in the P site during both initiation and elongation (18,25,29,30). G30-C40 and G29-C41 are two of the three critical G-C base pairs in the anticodon stem of fMet-$tRNA^{fMet}$ needed for efficient initiation (17-19) (Fig. 1B).

While GUG and UUG can act as alternate start codons, it is not clear why there is a sharp decrease in the frequency of usage of CUG as a start codon (0.024% of bacterial initiation codons) despite the tolerance of first-position codon-anticodon mismatches at the ribosomal P site (22). Start codon frequencies (AUG>GUG>UUG>>CUG) also correlate with translation efficiencies from each of the start codons compared to the AUG start codon, where GUG and UUG result in much higher levels of protein production (58.4% and 29.8% relative to AUG, respectively) than

CUG (0.86% relative to AUG) (22). Both the thermodynamic and kinetic stability of fMet-tRNA^{fMet} binding to these start codons on the ribosome also depend on the identity of the first-position nucleotide (AUG>GUG≈UUG>CUG) (21). Interestingly, when the series of three G-C base pairs in the anticodon stem is disrupted, translation efficiency is reduced, with a single base pair change of G30-C40 to C30-G40 (called tRNA^{fMet} M1) decreasing translation by 20-fold *in vivo* (20) (Fig. 1B). The M1 variant loses the ability to discriminate against CUG, exhibiting P-site codon recognition properties similar to elongator tRNA^{Met}. In contrast, wild type tRNA^{fMet} has a marked preference for GUG and UUG over CUG (21). The C30-G40 base pair of the M1 variant is identical to that of elongator tRNA^{Met}, suggesting a potential interplay between the tRNA anticodon stem and codon recognition in the 30S P site (21) (Fig. 1B). Recent studies using ribosome toeprint analysis, which measures the position of ribosomes on mRNAs, also indicate that complexes formed on model mRNAs with a CUG start codon show imprecise mRNA positioning, hypothesized to involve either a change in mRNA conformation in the ribosomal A site or frameshifting during translation initiation (21). This mRNA mispositioning is exacerbated by the tRNA^{fMet} M1 variant. IF2 restores normal mRNA positioning in these complexes, revealing a previously unknown quality control role for this initiation factor (21).

To determine how the ribosome interacts with the fMet-tRNA^{fMet} M1 variant, we solved five electron cryomicroscopy (cryo-EM) structures of *E. coli* ribosome complexes containing fMet-tRNA^{fMet} M1: four complexes prepared without IF2 containing tRNA^{fMet} M1 paired with the AUG, GUG, UUG, or CUG start codons, and a fifth prepared with a CUG start codon and IF2 containing the non-hydrolyzable GTP analog GDPCP. We find that the G30-C40 to C30-G40 change weakens A-minor interactions formed by 16S rRNA nucleotides G1338 and A1339 in the absence of IF2, which could contribute to the apparent mRNA mispositioning reported previously. The A-minor interaction between 16S nucleotide G1338 and the tRNA anticodon stem appears to be strengthened in the presence of IF2, consistent with the ability of IF2 to restore mRNA positioning

in analogous noncanonical initiation complexes. Finally, we find that 70S ICs prepared with $tRNA^{fMet}$ M1 and a CUG start codon appear to occupy the normal reading frame and present their A-site mRNA codons in a conformation similar to functional 70S complexes, suggesting aberrant toeprint banding previously observed in 70S ICs containing $tRNA^{fMet}$ M1 and a noncanonical CUG start codon likely arises from a change in mRNA conformation 3' of the ribosomal A site.

RESULTS

Variant M1 of $tRNA^{fMet}$ exhibits weakened interactions with 16S rRNA nucleotides G1338 and A1339. In 70S ICs containing fMet-$tRNA^{fMet}$ paired with an AUG start codon, 16S rRNA nucleotides A1339 and G1338 dock into the minor groove of the anticodon stem, making A-minor interactions with G30-C40 and G29-C41 (17-19). In the M1 variant, which contains C30-G40 rather than G30-C40, this recognition may be altered. To determine the structural effects of this base pair change, we determined the structures *of E. coli* 70S ICs containing the fMet-$tRNA^{fMet}$ M1 variant in the P site paired to mRNA with the noncanonical start codon CUG (2.6 Å overall resolution) and the canonical bacterial start codons AUG (2.8 Å overall resolution), GUG (2.6 Å overall resolution), and UUG (2.6 Å overall resolution) (Fig. 2A; Figs. S1-S3, Tables S1-S4). As expected, fMet-$tRNA^{fMet}$ nucleotides C30 and G40 form a Watson-Crick base pair, and this base pair change does not affect the pitch or width of the anticodon stem loop compared to wild type $tRNA^{fMet}$ (Fig. S4A). Instead, the C30-G40 pair reorganizes its interactions with 16S rRNA nucleotides G1338 and A1339, which project into the tRNA minor groove (Fig. 2B). The type I A-minor motif interaction between the C30-G40 base pair and A1339 is weakened through reduction of the hydrogen bond angle between the A1339 and G40 nucleobases. This interaction typically involves a nearly linear hydrogen bond between atom N3 of A1339 and the minor groove face of G30 in wild type $tRNA^{fMet}$, but the reorientation of hydrogen bond donor and acceptor groups in the $tRNA^{fMet}$ minor groove due to the M1 mutation substantially reduces this hydrogen bond angle (WT: 169°; M1: 134°), weakening this interaction (Fig. 2C, 3A) (PDB code 5MDZ). Additionally,

the interaction distance between the A1339 2'-OH and its nearest hydrogen bond acceptor on the position 40 base (atom O2 of C40 in wild type $tRNA^{fMet}$; atom N3 of G40 in $tRNA^{fMet}$ M1) is increased roughly 0.4 Å from 3.0 Å to 3.4 Å in complexes formed with $tRNA^{fMet}$ M1 compared to those formed with WT $tRNA^{fMet}$ (Fig. 3B) (31) (PDB code 5MDZ). Hydrogen bonding distances in the A1339-C30-G40 A-minor interaction are not substantially different in the presence of UUG, GUG, or AUG start codons compared to the CUG start codon, suggesting the strength of the interaction between $tRNA^{fMet}$ M1 nucleotide G40 and 16S rRNA nucleotide A1339 is not dependent upon the identity of the mRNA codon first-position nucleotide (Fig. S5). Adjacent to this A-minor interaction is the wild type G29-C41 base pair, which forms a type II A-minor interaction with G1338. Specifically, the 2'-OH of $tRNA^{fMet}$ M1 nucleotide C41 forms hydrogen bonds with the N3 atom and 2'-OH group of G1338 (Fig. 2D). Compared to a 70S ribosome complex prepared with wild type $tRNA^{fMet}$, the interaction distance between the G1338 and C41 2'-OH groups is increased from 3.1 Å to 3.5 Å, suggesting a slight weakening of hydrogen bonding, while the interaction distance between the G1338 base and C41 2'-OH group remains unchanged (2.8 Å) (Fig. 3C). Like the adjacent interaction of A1339 with the tRNA anticodon stem, the interaction between G1338 and C41 does not show meaningful differences in hydrogen bonding distances with canonical UUG, GUG, or AUG start codons compared to the non-canonical CUG start codon (Fig. S6). These results indicate that the simple swapping of G30-C40 to C30-G40 in the $tRNA^{fMet}$ M1 variant weakens the ability of 16S rRNA nucleotides G1338 and A1339 to grip the tRNA at its minor groove through the disruption of important interactions with the anticodon stem.

Weakened interactions between the $tRNA^{fMet}$ M1 anticodon and the noncanonical CUG start codon. When $tRNA^{fMet}$ M1 interacts with the CUG start codon, toeprint analysis indicates abnormal positioning of the mRNA, consistent with ribosome complexes appearing to occupy the 0 (normal), +1, and +2 reading frames, with the major product band consisting of apparent +2

frame complexes (21). This suggests a destabilization of mRNA which may allow the initiation complex to sample different positions. In our structure, we find that the CAU anticodon of $tRNA^{fMet}$ M1 interacts with the CUG start codon in the normal reading frame, with map density in the tRNA exit (E) and P sites suggestive of 0-frame AAA and CUG codons, respectively (Fig. S7A-B). However, the first-position codon-anticodon base pair between C_{+1} of the mRNA and U36 of fMet-$tRNA^{fMet}$ M1 is weak (mRNA nucleotide numbering begins at the P site as +1, +2, and +3) (Fig. 4A). While their nucleobases are oriented with their Watson-Crick faces to pair, the hydrogen bond donor-acceptor distances observed are 3.5 Å and 3.9 Å, indicating only weak interactions between these nucleotides are possible (Fig. 4B). The second and third positions of the codon-anticodon interaction (U_{+2}:A35 and G_{+3}:C34, respectively) display hydrogen bonding distances and geometry consistent with typical Watson-Crick base pairing, ranging from 2.7 Å to 3.0 Å in donor-acceptor distances (Figs. 4C-D). Because 70S ICs formed with $tRNA^{fMet}$ M1 and canonical AUG, GUG, or UUG start codons display primarily 0 frame toeprint band formation, do not differ in their tRNA-ribosome interactions compared to CUG in our structures, and differ from CUG start codon complexes only in the identity of their P-site mRNA codon first-position nucleotides, it appears that mRNA mispositioning in ICs containing $tRNA^{fMet}$ M1 and CUG start codons is mediated by differences in base pairing strength between CUG and the canonical start codons rather than by codon-specific differences in tRNA-ribosome interaction strength.

70S ICs containing $tRNA^{fMet}$ M1 paired to a CUG start codon present their A-site codons in the 0 reading frame. To further investigate whether 70S complexes containing $tRNA^{fMet}$ M1 interacting with a CUG start codon undergo +2 frameshifting during initiation in the absence of IF2, the cryo-EM sample containing mRNA with a CUG start codon and lacking IF2 was prepared in the presence of an excess of $tRNA^{IleX}$, which decodes the AUA codon which would be presented at the A site in the event of a +2 frameshift. Notably, toeprint analysis studies have previously shown that apparent +2 frame toeprint bands comprise the major product in 70S ICs containing

$tRNA^{fMet}$ M1 and a CUG start codon (21). Therefore, if these 70S ICs undergo +2 frameshifting, a major population of particles should be observed which contains $tRNA^{IleX}$ at the ribosomal A site. Interestingly, each cryo-EM dataset collected in the absence of IF2 contains a minor population of particles containing both P- and A-site tRNAs (CUG: 10.7% of 70S particles; UUG: 8.9% of 70S particles; GUG: 8.6% of 70S particles; AUG: 8.8% of 70S particles) (Figs. S1 and S2). In the datasets containing UUG, GUG, and AUG start codons, where only $tRNA^{fMet}$ M1 was provided to the reactions, any A-site occupancy must be due to $tRNA^{fMet}$ M1, representing a background level of A-site tRNA binding. The cryo-EM dataset prepared with a CUG start codon and excess $tRNA^{IleX}$ displays only a slight enrichment in A-site tRNA-containing particles compared to UUG, GUG, or AUG datasets prepared without $tRNA^{IleX}$, further suggesting that these complexes do not present +2 frame AUA codons at the ribosomal A site and primarily occupy the 0 reading frame.

An alternative explanation for previously observed toeprint band shifts in 70S ICs containing $tRNA^{fMet}$ M1 paired to a CUG start codon is that the A-site codon is presented in an atypical, nonfunctional conformation which alters mRNA accessibility to reverse transcriptase downstream of the ribosome while not shifting the mRNA reading frame. This hypothesis is consistent with the observation that these 70S ICs are deficient in peptide bond formation activity, displaying reduced rate and extent of dipeptide formation when the tRNA decoding the 0 frame A-site codon is added (21). The map quality for the mRNA in the A site of 70S ribosome complexes is typically poor in the absence of an A-site tRNA, but map density suggests three mRNA nucleotides occupy the A site in our structure in a conformation resembling that of a 70S complex competent for both initiation and subsequent elongation (31) (Fig. S7C) (PDB code 7K00). These results suggest that mRNA mispositioning observed in 70S ICs containing $tRNA^{fMet}$ M1 paired with a CUG codon occurs downstream of the ribosomal A site rather than proceeding through frameshifting or aberrant presentation of the A-site mRNA codon.

IF2 partially restores tRNA^{fMet} M1 interactions with the ribosomal P site. When the 50S ribosomal subunit is recruited during initiation, fMet-tRNA^{fMet} is constrained in the P/I orientation through its interaction with IF2 ("P" refers to position on the 30S subunit and "I" refers to a unique initiation orientation on the 50S subunit, adjacent to the P site) (25). IF2 can suppress aberrant toeprint band formation in complexes containing tRNA^{fMet} M1 and a CUG start codon, suggesting that stabilization of tRNA^{fMet} M1 in the P/I orientation by IF2 may improve contacts between the 16S rRNA and tRNA^{fMet} anticodon stem (21). To determine the structural basis of IF2's rescue activity, we determined a 2.6-Å cryo-EM structure of an *E. coli* 70S IC containing a P-site fMet-tRNA^{fMet} M1, mRNA with a P-site CUG start codon, and IF2 containing the non-hydrolyzable GTP analog GDPCP (Fig. 5A; Figs. S8, S9, Table S5). As in our structure without IF2, we observe no effect on tRNA width or pitch due to the M1 mutation (Fig. S4B). Domain C1 of IF2 interacts with the GTPase center of the ribosome, and its C terminus spans the A and the P sites to directly bind the fMet moiety located in the 50S P site (32). In our structure, when IF2 is present, fMet-tRNA^{fMet} M1 continues to form interactions with the 16S rRNA nucleotides G1338 and A1339 (Fig. 5B). As in the absence of IF2, A1339 projects into the tRNA minor groove alongside the C30-G40 base pair, but poor hydrogen bonding geometry between G40 and A1339 precludes formation of strong type I A-minor interactions such as those observed with wild type tRNA^{fMet} (Fig. 5C, Fig. S10) (13). In contrast, IF2 strengthens interactions of G1338 with the adjacent G29-C41 base pair of tRNA^{fMet} M1. Compared to when IF2 is absent, we observe an approximately 2 Å displacement of the tRNA^{fMet} M1 anticodon stem loop (ASL) and the adjacent 16S rRNA loop containing G1338 and A1339 toward the ribosomal 30S head domain (Fig. S11A). We also observe that the position of G1338 in the tRNA minor groove is altered, with the G1338 base and 2'-OH group displaced 1.2 Å and 0.8 Å upward along the tRNA minor groove, respectively, and the 2'-OH of nucleotide C41 displaced 0.8 Å toward G1338 (relative to the C30-G40 base pair) compared to when IF2 is absent (Fig. S11B). This movement reduces hydrogen bond distances between G1338 and C41, permitting the N3 atom and 2'-OH of G1338 to form tighter A-minor interactions with the 2'-OH

group of C41 (Figs. 5D and S11B). Together, these results indicate that IF2 constrains $tRNA^{fMet}$ M1 in the P/I orientation and that this constraint is sufficient to strengthen interactions between the 30S head domain (in particular, G1338) and $tRNA^{fMet}$ M1. This would, in turn, improve the ability of the ribosome to grip the P-site $tRNA^{fMet}$ M1 and may contribute to the productive engagement of the CUG codon. These small movements that stabilize critical interactions could help explain how IF2 restores normal mRNA positioning in noncanonical complexes analyzed previously (21).

IF2 does not influence pairing between the anticodon of $tRNA^{fMet}$ M1 and the CUG start codon. We reasoned that if IF2 constrains the positioning of the tRNA at the CUG start codon such that the distance between the first position C_{+1} and anticodon nucleotide U36 is reduced, instability in mRNA positioning could be prevented through strengthening of the codon-anticodon interaction (Fig. 6A). However, in the presence of IF2, we find that there is no reduction of hydrogen bonding distance at the first position of the codon-anticodon interaction compared to when IF2 is absent (Fig. 6B). Additionally, as in the absence of IF2, the second and third positions of the codon-anticodon interaction maintain typical Watson-Crick base pairing distance and planarity (Figs. 6C-D). Together, these results suggest that IF2's ability to suppress apparent mRNA mispositioning does not seem to involve enhancement of codon-anticodon pairing strength in the ribosomal P site.

70S ICs containing $tRNA^{fMet}$ M1 paired to a CUG start codon present their A-site codons in the 0 reading frame. Given the ability of IF2 to rescue normal mRNA positioning in toeprint analysis studies of 70S ICs containing $tRNA^{fMet}$ M1 and CUG start codons and given that analogous 70S ICs formed without IF2 appear to occupy the 0 reading frame and present their A-site codons in a conformation resembling other elongation-competent 70S complexes (21), we predicted similar observations for 70S ICs containing $tRNA^{fMet}$ M1, a CUG start codon, and IF2. As expected, these complexes display map density in the E and P sites consistent with AAA and

CUG codons, respectively, and map density in the A site suggests the mRNA codon is presented similarly to 70S complexes productively engaging an A-site tRNA (31) (Fig. S7D-F) (PDB code 7K00).

DISCUSSION

In this work, we sought to gain insight into initiation fidelity by determining structures of noncanonical complexes carrying the fMet-tRNA^{fMet} M1 variant paired with the noncanonical CUG start codon and canonical AUG, GUG, and UUG start codons (21). Changing the G-C base pair at position 30-40 of tRNA^{fMet} to C-G weakens the A-minor interactions formed between 16S rRNA nucleotides A1339 and G1338 and the tRNA minor groove, which manifests in a reduced ability to discriminate against CUG start codons compared to wild type tRNA^{fMet}. While the change in the positions of G1338 and A1339 projecting into the tRNA minor groove is small, the functional implications are substantial given that these changes reduce discrimination by decreasing the stability of canonical GUG and UUG complexes by 10-fold but not further destabilizing CUG complexes relative to ICs formed with wild type tRNA^{fMet} (21).

The observation that tRNA^{fMet} M1 displays weakened A-minor interactions with the 16S rRNA is consistent with prior analysis of the thermodynamics and prevalence of A-minor motifs in structured RNAs (33). Type I A-minor motifs are strongest when the interaction consists of an adenosine buried in the minor groove of a G-C base pair with the A- and C- containing strands antiparallel to one another, as is the case for the interaction of 16S nucleotide A1339 with the G30-C40 base pair in wild type tRNA^{fMet}. In the P4-P6 domain of the *Tetrahymena* group 1 intron, there is a roughly 25% decrease in the free energy of formation of type I A-minor motifs formed with G-C base pairs where the A- and G- containing RNA strands are antiparallel (relative to interactions with the A- and C-containing strands antiparallel). This example is similar to the interaction of 16S rRNA nucleotide A1339 with tRNA^{fMet} M1. The stabilizing impact of strong type I A-minor interactions may be further exemplified by the widespread nature of type I interactions

with antiparallel A- and C- strands as seen in a phylogenetic analysis of 23S rRNA from *H. marismortui and T. thermophilus* (33). In this analysis, 89% of observed type I A-minor motifs consisted of G-C base pairs with antiparallel A- and C-containing strands (as observed with wild type $tRNA^{fMet}$), while only 6% consisted of G-C pairs with antiparallel A- and G-containing strands (as observed with $tRNA^{fMet}$ M1). This prevalence among highly structured RNAs is suggestive of the importance of strong type I A-minor interactions for structural stability. The thermodynamic stability of the interaction of type I A-minor motif interaction between A1339 and wild type $tRNA^{fMet}$ provides additional context for why weakening this interaction in the $tRNA^{fMet}$ M1 variant disrupts normal translation initiation by loosening the ribosome's grip on the tRNA.

Interestingly, *E. coli* ribosomes containing the 16S rRNA mutation G1338A, which strengthens the interaction of the 16S rRNA with the $tRNA^{fMet}$ ASL minor groove, undergo spurious initiation at noncanonical start codons, including CUG, more frequently than wild type ribosomes (19). Conversely, mutations of position A1339, which weaken the tRNA-ribosome interaction at this position, yield ribosomes with greatly reduced translation activity (17,18). These results suggest that translation initiation may be fine-tuned for both efficiency and accuracy in a manner that depends on the strength of interactions of the initiator tRNA with both the mRNA codon and the ribosome. Excessively strong ribosome-tRNA interactions cause initiation at incorrectly selected start codons while weak ribosome-tRNA or tRNA-mRNA interactions, as observed for $tRNA^{fMet}$ M1 initiating translation on the start codon CUG, cause inefficient initiation or nonproductive engagement of the start codon. Given the apparent lack of a direct effect of the first-position codon-anticodon interaction on the strength of tRNA-rRNA interactions between 16S nucleotides A1339 and G1338 and the tRNA minor groove, the ribosome may independently require sufficiently strong rRNA-tRNA and mRNA-tRNA interactions for productive initiation. Previous competition binding assays demonstrate that 30S and 70S ICs assembled with CUG start codons are less thermodynamically and kinetically stable than those formed with AUG, GUG, or UUG start codons irrespective of whether they contain wild type $tRNA^{fMet}$ or $tRNA^{fMet}$ M1 (21);

however, the discrepancy between the stability of ICs containing a CUG start codon and those containing a canonical start codon is smaller when they are formed with $tRNA^{fMet}$ M1. This reduction in the discrepancy may help account for the reduction in the ability of $tRNA^{fMet}$ M1 to discriminate against CUG start codons, which in previous experiments results from a reduction in preference for the canonical but near-cognate start codons GUG and UUG rather than an increase in preference for pairing with CUG, on which neither wild type $tRNA^{fMet}$ nor the M1 variant efficiently initiate translation (21).

One previously observed consequence of the C30-G40 base pair change in $tRNA^{fMet}$ M1 is mRNA mispositioning, as assessed by toeprint analysis (21). In these assays, initiation complexes containing the $tRNA^{fMet}$ M1 variant and mRNA containing the noncanonical CUG start codon appear to occupy the 0 (normal), +1, and +2 reading frames, with the apparent +2 frame band forming the major product. This toeprint heterogeneity is only observed with $tRNA^{fMet}$ M1 engaging a CUG codon, not with AUG, GUG, or UUG (21). The +1 or +2 frame would indicate a movement of the ribosome toward the 3' end of the mRNA, presumably moving the C_{+1} or U_{+2} nucleotide into the E site with a change of the nucleotides that are positioned in the P site. Another interpretation is that the mRNA conformation in the ribosomal A site is altered in some way that exposes the next codon in a shifted downstream register without changing the codon presented in the P site (21). We conclude from our structure of 70S ICs containing $tRNA^{fMet}$ M1 paired with the CUG start codon that $tRNA^{fMet}$ M1 engages the CUG codon in the 0 reading frame, based on map density for the P-site mRNA codon and our observation that adding an excess of $tRNA^{IleX}$, which decodes the +2 frame AUA codon, causes only a very slight enrichment in the proportion of picked 70S particles displaying tRNA occupancy at the ribosomal A site compared to AUG, GUG, and UUG start codon datasets prepared only with $tRNA^{fMet}$ M1. Additionally, the conformation of the A-site mRNA codon appears similar to that observed in 70S complexes productively engaging tRNAs at the A site (31) (PDB code 7K00). Therefore, while prior biochemical assays show an apparent change in mRNA register or conformation at the P or A

site, our structural data suggest that the mRNA is normal in the context of the P and A sites and that prior toeprint analysis assays are reporting on features of these ICs other than the mRNA reading frame or A-site codon conformation. Another possibility is that the mRNA path is altered 3' of the A-site codon, giving rise to the shorter toeprints, although the mRNA was not resolved 3' of the A site in the cryo-EM maps and thus this possibility cannot be evaluated from our structures alone.

Prior ribosome structural studies have focused on understanding single base pair mismatches between the codon and the anticodon at the P site in both initiation and elongation contexts (34,35). Several of these elongation structures contain pyrimidine-pyrimidine mismatches at the P site and while the mismatched nucleotides present their Watson-Crick faces for pairing, observed hydrogen bond donor-acceptor distances are not within accepted ranges and are suggestive of weak interactions. For example, in a structure with a third position C_{+3}-C34 mismatch, the closest donor-acceptor distance is 3.6 Å and in a structure of a first-position U_{+1}-U36 mismatch, the donor-acceptor distances are 4.0 Å and 4.5 Å (34,35). In our 70S IC structures containing a first-position C_{+1}-U36 mismatch, we observe hydrogen bond donor-acceptor distances of 3.5 Å and 3.9 Å, also suggesting weak interaction. Crucially, G-U and U-U base pairs, which are both tolerated at the first position of the codon-anticodon interaction during initiation, may both form two hydrogen bonds in studies of model RNA duplexes, while C-U pairs have been observed to form either one or two hydrogen bonds in model RNAs (36,37). Additionally, it is known empirically that 30S and 70S ICs formed with CUG start codons are less stable than those formed with the canonical bacterial start codons AUG, GUG, and UUG (21). If base pairing strength at the first position of the start codon is important for efficient translation initiation in addition to strong interactions between the initiator tRNA and 16S rRNA, this may help explain why CUG is not used as a common non-AUG start codon in bacteria, in contrast to GUG and UUG start codons (22).

IF2 imposes physical constraints on fMet-tRNA^{fMet} that appear to rescue mRNA positional instability in the context of CUG start codons and contribute to productive initiation (21). We find that IF2 adopts a normal open conformation with domain C2 recognizing the fMet moiety of the initiator tRNA (Fig. S11A). This recognition, and the subsequent constraining of tRNA^{fMet} in the P/I orientation by IF2, also appears to allosterically regulate how the 30S head domain nucleotide G1338 grips the anticodon stem of tRNA^{fMet} M1, strengthening the type II A-minor interaction between G1338 and tRNA^{fMet} nucleotide C41 by permitting G1338 to project more deeply into the tRNA minor groove. While it is not clear if reestablishing the type II A-minor contacts between G1338 and tRNA^{fMet} M1 in the presence of IF2 is itself directly responsible for stabilizing the mRNA placement, these findings are consistent with prior biochemical studies demonstrating that IF2 is sufficient to restore wild type-like codon discrimination behavior in ICs formed with tRNA^{fMet} M1 and mRNA containing a CUG start codon (21).

EXPERIMENTAL PROCEDURES

Ribosome purification. Ribosomes were purified from *E. coli* MRE600 cells as previously described (38,39). Briefly, cells were grown in lysogeny broth (LB) to OD_{600} 0.7 at 37 °C in a shaking incubator then cooled on ice for 20 min. Cells were pelleted by centrifugation, washed with buffer 1 (10 mM HEPES-KOH, pH 7.6, 10 mM $MgCl_2$, 1M NH_4Cl, 6 mM β-mercaptoethanol (β-Me)) twice then resuspended in buffer 2 (buffer 1 with 100 mM NH_4Cl) and lysed using the Emulsiflex-C5 high-pressure homogenizer (Avestin). The lysate was clarified by centrifugation at 27,000 × *g* for 30 min, followed by another spin at 42,000 × *g* for 17 h to pellet ribosomes. The pellet was resuspended in buffer 2 and layered over a 10-40% (w/v) sucrose gradient (buffer 2) and centrifuged at 70,000 × *g* for 12 hr with no break for deceleration. The gradients were then fractionated using a Brandel gradient fractionator monitoring absorbance at 254 nm, and fractions

corresponding to the 70S peak were pooled and concentrated to 11 μM via pelleting. 70S aliquots were flash frozen and stored at -80 °C.

IF2 purification. The alpha form of IF2 was purified using the pET24b-IF2-His6 plasmid through overexpression in BL21 (DE3) Gold cells. Cells were grown in a shaking incubator at 37 °C at 230 rpm. IF2 overexpression was induced by the addition of 1 mM IPTG at OD_{600} of 0.6 for 3.5 hr. All subsequent centrifugation steps were performed at 4 °C. Flasks were placed on ice for 5 min, then pelleted by centrifugation at 4000 x *g* for 20 min. Cell pellets were then washed by resuspension in 20 mM Tris-HCl, pH 8.0, and pelleted again by centrifugation. Cells were lysed in 50 mM Tris-HCl pH 7.5, 60 mM NH_4Cl, 0.7 mM $MgCl_2$, 5 mM imidazole, 15% glycerol, 10 μM GDP, and 2 mM DTT using three passes through the Emulsiflex-C5 high-pressure homogenizer (Avestin). The lysate is then clarified by centrifugation at 16,600 x *g* for 30 min. The supernatant is loaded on to a 5 ml HisTrap™ HP column (Cytiva) using an ÄKTA FPLC system. IF2 was eluted using a 5-500 mM imidazole gradient and dialyzed into 50 mM Tris-HCl pH 7.5, 60 mM NH_4Cl, 0.7 mM $MgCl_2$, 15% glycerol, 5 μM GDP, and 2 mM DTT. IF2 purity was estimated by SDS-PAGE and its concentration determined using a Bradford assay. Samples were aliquoted and flash frozen in liquid nitrogen to be stored at -80 °C.

$tRNA^{fMet2}$ M1 purification and aminoacylation. $tRNA^{fMet2}$ with the M1 mutations (G30C, C40G) were cloned and purified at previously described (21). The mutations were introduced into pUC13-trnfM by QuikChange™ mutagenesis and overexpressed in *E. coli* B105 cells grown in LB with 100 μg/ml ampicillin at 37 °C. Cells were pelleted and washed with PBS (10 mM phosphate pH 7.4, 137 mM NaCl, 3 mM KCl), then resuspended in 20 mM Tris-HCl pH 7.6, 20 mM $MgCl_2$. The lysate was phenol extracted using phenol saturated with 25 mM NaOAc pH 5.2, 50 mM NaCl, then 3 M NaOAc pH 5.2 (1/10 volume) and isopropanol (equal volume) were added and incubated for 2 hr at 4 °C to precipitate crude tRNA. RNA was pelleted by centrifugation at 8,500 rpm for 30 min at 4 °C in a tabletop microfuge and washed with 70% ethanol, dissolved in 200 mM Tris-

acetate pH 9.0, and incubated at 37 °C for 30 min, followed by another round of ethanol precipitation. The resulting RNA pellet is then dissolved in water, mixed with loading dye (50% glycerol with bromophenol blue), and $tRNA^{fMet2}$ M1 was separated on a 12% native PAGE gel overnight at 80 V until dye reaches the bottom of the gel. The band corresponding to $tRNA^{fMet2}$ was identified by UV shadowing and excised from the gel. The RNA was extracted using the crush-and-soak method, and then eluted in 300 mM NaOAc pH 5.2, 0.1% SDS, 1 mM EDTA overnight at 4 °C. The eluate solution was then extracted with water-saturated phenol followed with chloroform-isoamyl alcohol (24:1). $tRNA^{fMet2}$ M1 was precipitated overnight at -20 °C by the addition of 3 M NaOAc pH 5.2 (1/10 volume) and ice-cold ethanol (3x volume). The final $tRNA^{fMet2}$ M1 pellet was obtained by centrifugation at 8,800 rpm for 30 min at 4 °C in a microfuge, washed with 70% ethanol, dissolved in water, and stored at -80 °C. RNA concentration was determined using absorbance at 260 nm. Aminoacylation by methionyl-tRNA synthetase (MetRS) and formylation by methionyl-tRNA formyltransferase (MTF) to generate fMet-$tRNA^{fMet2}$ M1 was performed as previously described (40). MetRS and MTF activity were confirmed by acid gel electrophoresis stained with methylene blue and TLC using [^{35}S]-methionine as previously described (40).

70S complex assembly. 70S initiation complexes (ICs) were prepared by stepwise 5 min incubations of 1.6 μM *E. coli* 70S, 3.2 μM mRNA (IDT, Table S6), and 4.8 μM fMet-$tRNA^{fMet2}$ M1 in buffer 2 (5 mM HEPES-KOH pH 7.5, 50 mM KCl, 10 mM NH_4Cl, 6 mM β-Me) at 37 °C. The mRNA sequence is 5'- GGC AAG GAA AUA AAA NUG GUA UAC UUU -3' (P-site codon underlined, N can be A, U, G, or C). For the CUG start codon complex, 6.4 μM $tRNA^{IleX}$ was additionally added to the reaction to monitor for presentation of a +2 frame AUA codon at the ribosomal A site. For the complex containing a CUG start codon, IF2, and the non-hydrolyzable GTP analog GDPCP, a 70S initiation complex was prepared similarly (without $tRNA^{IleX}$), and IF2 was incubated for 20 minutes with GDPCP in a 1:100 molar ratio before being added to the 70S

IC (10 μM IF2 and 1 mM GDPCP final concentrations). Following assembly, 70S IC samples were briefly placed on ice until preparing grids for cryo-EM.

Cryo-EM sample preparation and data collection. To prepare samples for cryo-EM, C-Flat™ holey carbon gold grids (R1.2/1.3, 300 mesh) were glow discharged in a PELCO easiGlow™ glow discharger (Ted Pella) for 30 seconds. Grids were prepared in a Vitrobot Mark IV (FEI) at 4 °C and 100% humidity. 3 μL of the prepared 70S IC sample was applied to grids and allowed to stand for 15 seconds before blotting and plunging into liquid ethane to vitrify.

Cryo-EM processing and model building. *E. coli 70S-NUG mRNA-fMet-tRNA^{fMet} (no IF2) structures* (Figs. S1-S3). Prior to processing cryo-EM data, movie frames were aligned using Patch Motion Correction and contrast transfer function (CTF) parameters were estimated using Patch CTF Estimation in cryoSPARC 4.5.3 (41). Micrographs displaying poorer than 5 Å estimated maximum resolution were discarded. Following pre-processing, an initial round of automated particle picking was performed on a random subset of 100 micrographs using the reference-free Blob Picker in cryoSPARC 4.5.3. Extracted particles were subjected to reference-free two-dimensional classification to generate a set of 2D reference images, which were then used as templates to repick particles from the 100 micrograph subset. Template-picked particles were extracted and 2D-classified, then ribosome-like classes were selected to generate an optimized particle set to train a Topaz particle picking model (42). The trained Topaz model was used to pick particles from all retained micrographs. Picked particles were extracted with 4X binning and 2D-classified and ribosome-like 2D classes were selected. Three *ab initio* 3D reconstructions (70S ribosomes, 50S subunits, and junk) were generated from selected particles and used as references for heterogeneous 3D refinement, with 70S ribosome particles being selected for further processing and 50S subunit and junk particles being discarded. Selected 70S particles were re-extracted without binning and subjected to initial homogeneous 3D refinement and CTF refinement to correct for microscope aberrations and per-particle defocus estimation.

Particles were then subjected to two rounds of iterative reference-based motion correction (43), homogeneous 3D refinement, and CTF refinement (44) to generate an optimized high-resolution particle set. Focused 3D classification was then performed using a mask of the ribosomal A, P, and E sites generated from the A-, P-, and E-site tRNA chains of PDB code 5JTE (45) in UCSF ChimeraX (46). Particles containing P-site tRNAs and either no (UUG, GUG, and AUG mRNA datasets) or minimal (CUG mRNA dataset) E-site tRNA density were subjected to final homogeneous 3D refinement to generate high-resolution 3D reconstructions. The resultant maps were sharpened for modeling using sharpening B-factors automatically estimated from the Guinier plots for each final homogeneous refinement job. A local resolution map was generated for each reconstruction using cryoSPARC's local resolution estimation implementation with a local FSC cutoff of 0.5.

E. coli 70S-CUG mRNA-fMet-tRNA^{fMet}-IF2 structure (Figs. S8, S9). Micrographs were preprocessed in RELION-3.1 (47) using RELION's motion correction implementation and CTFFIND-4 for CTF estimation (48). Micrographs displaying poorer than 8 Å estimated maximum resolution were discarded and following pre-processing, particles were picked using the RELION-3.1 Laplacian-of-Gaussian and template-based autopickers (similar to the prior dataset) to generate an optimized particle set for Topaz model training (42). Topaz was then trained and used to pick particles from all retained micrographs, which were extracted with 4X binning, 2D classified, used to generate an initial 3D reconstruction with the stochastic gradient descent method (41), and 3D classified for selection of 70S ribosome particles. Selected particles were re-extracted without binning, subjected to initial 3D auto-refinement, and 3D classified without alignment using a focus mask of the ribosomal A and P sites and GTPase center generated from the tRNA and IF2 chains of PDB code 6O9K (49) in UCSF ChimeraX (46). Particles containing P-site fMet-tRNA^{fMet} and IF2 were subjected to CTF refinement (44,47) and 3D auto-refinement. Particles were sorted by E-site tRNA content via two additional rounds of focused classification,

first using a mask generated from the P- and E-site tRNA chains of PDB code 5JTE and then using a mask generated from the E-site tRNA chain of PDB code 5JTE alone (45). Particles containing P- and E-site tRNAs and IF2 were subjected to two rounds of iterative CTF refinement, Bayesian polishing (43), and 3D auto-refinement, then post-processed without sharpening using a solvent mask generated from a 10 Å lowpass filtered copy of the 3D refinement map to yield a final 2.6 Å reconstruction. The resultant map was sharpened for modeling using the Autosharpen tool in PHENIX (50). A local resolution map was generated using RELION's local resolution estimation implementation.

To build a model of 70S-IC containing fMet-tRNA^{fMet} M1, UCSF ChimeraX was used to rigidly dock coordinates from an existing *E. coli* 70S structure containing P-site fMet-tRNA^{fMet} (PDB code 7K00) (31) into the final 3D refinement map. For the 70S-IC containing IF2 and fMet-tRNA^{fMet} M1, an existing IF2-containing *E. coli* 70S-IC structure was rigidly docked in UCSF ChimeraX (PDB code 6O9K) (49) into the final 3D refinement map. Ligand coordinates and restraints for GDPCP were generated using eLBOW in PHENIX (51) before manually fitting GDPCP coordinates into the nucleotide binding site of IF2 using COOT (52). PDB code 7K00 was used to obtain initial A-site GUA codon coordinates and initial magnesium ion coordinates for all structures (31). The docked coordinates were subjected to real space refinement in PHENIX using the final sharpened maps and validated using MolProbity (53,54).

DATA AVAILABILITY

Atomic coordinates, and structure factors have been deposited in the Protein Data Bank, www.pdb.org and Electron Microscopy Data Bank (EMDB): (PDB codes 9AX7, 9AX8, 9CG5, 9CG6, 9CG7; EMDB codes EMD-43929, EMD-43930, EMD-45569, EMD-45572, EMD-45573)

ACKNOWLEDGEMENTS

Support for this work was provided by the NIH Training Grant T32 GM135060 (JMM), and NIH grants R01 GM093278 (CMD) and R01 GM072528 (KF). A portion of this research was supported by NIH grant U24GM129547 and performed at the PNCC at OHSU and accessed through EMSL, a DOE Office of Science User Facility sponsored by the Office of Biological and Environmental Research. This study was also supported by the Robert P. Apkarian Integrated Electron Microscopy Core (IEMC) at Emory University, which is subsidized by the School of Medicine and Emory College of Arts and Sciences. Additional support was provided by the Georgia Clinical & Translational Science Alliance of the National Institutes of Health under award number UL1TR000454.

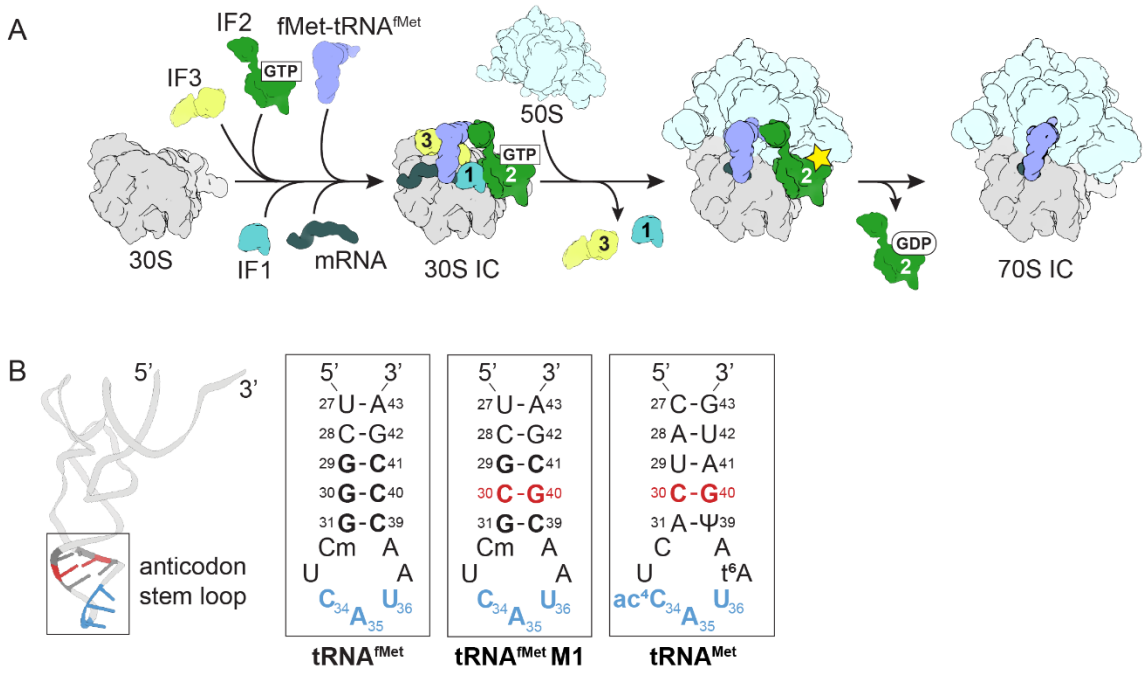

Figure 1. **tRNA^{fMet} has unique features for translation initiation**. A. Translation initiation begins with initiation factors (IF1, IF2, IF3) binding to the 30S subunit in a defined order to guide fMet-tRNA^{tRNA} to the P site (called the 30S IC). 50S joins, GTP is hydrolyzed by IF2, and all factors are released. The resulting 70S IC is ready for the elongation phase. B. Mutation of the conserved G-C base pairs of the anticodon stem of tRNA^{fMet} M1 affect the ability of the ribosome to initiate translation on mRNA. Zoomed in view of the anticodon stem loop (ASL) of tRNA^{fMet} showing the anticodon (blue) and three conserved G-C base pairs (bold). The tRNA^{fMet} M1variant containing the C30-G40 mutation (red). The tRNA^{fMet} M1 30-40 base pair is identical to that of elongator tRNA^{Met}.

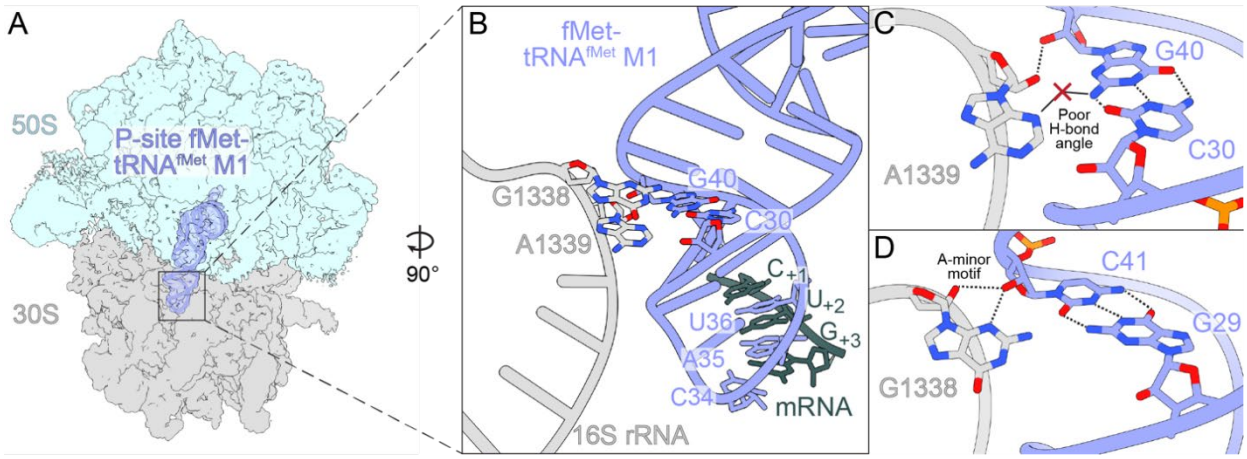

Figure 2. One base pair change in the anticodon stem of tRNA^{fMet} alters how the 16S rRNA recognizes initiator tRNA. A. Map of 70S ribosome complexes containing P-site fMet-tRNA^{fMet} with the M1 mutation (substitution of G-C with C-G at position 30-40). Map and model of tRNA are superimposed to enhance visibility. B. The tRNA^{fMet} M1 ASL interacts with 16S rRNA nucleotides G1338 and A1339. C. In the presence of the M1 mutation, the C30-G40 base pair forms weakened A-minor interactions with the base of conserved 16S rRNA nucleotide A1339. D. In the presence of the M1 mutation, tRNA^{fMet} nucleotide C41 forms A-minor interactions with the base of conserved 16S nucleotide G1338.

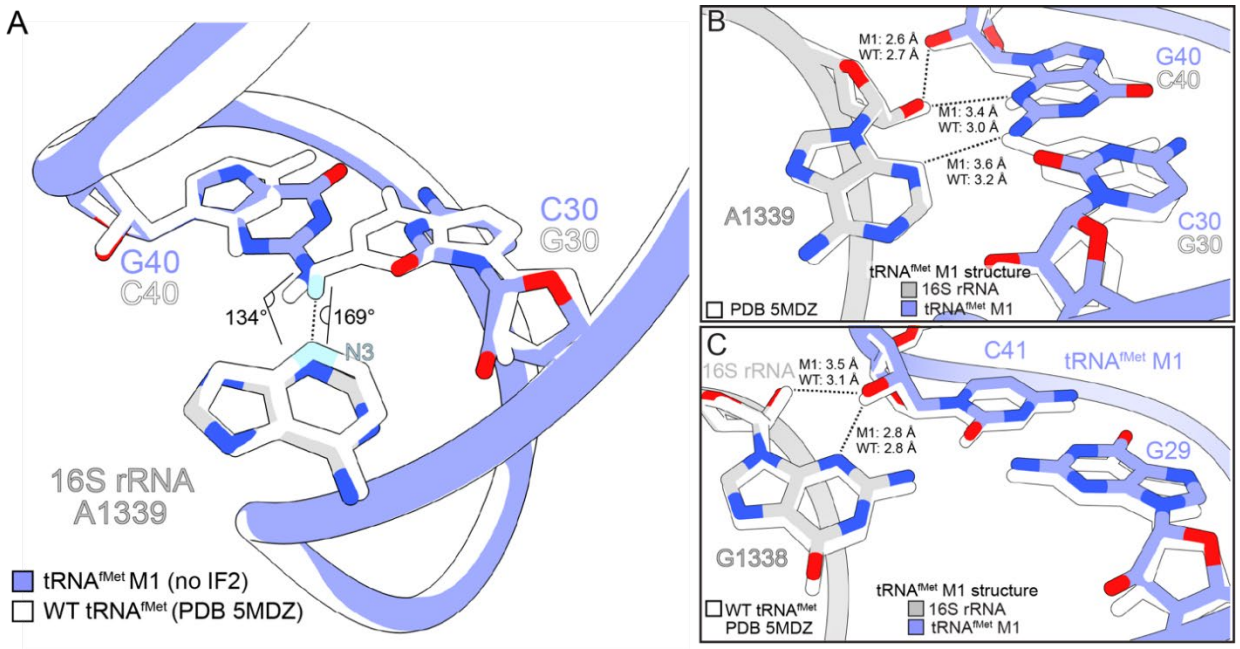

Figure 3. The M1 mutation alters interactions with 16S rRNA nucleotides G1338 and A1339.

A. In the absence of IF2, the tRNA^{fMet} M1 mutation tightens the hydrogen bonding angle between atom N3 of 16S rRNA nucleotide A1339 and hydrogen atom (denoted in blue) of the G of the 30-40 base pair, leading to poorer hydrogen bonding geometry compared to wild type tRNA^{fMet}. B. Compared to a structure containing wild type tRNA^{fMet} (PDB code 5MDZ), hydrogen bonds between A1339 and the tRNA^{fMet} M1 C30-G40 base pair are lengthened, reflecting weaker interaction. C. Compared to wild type tRNA^{fMet}, the 2'-OH of tRNA^{fMet} M1 engages in more distant interactions with the G1338 2'-OH group, but its interaction with the G1338 base is unchanged.

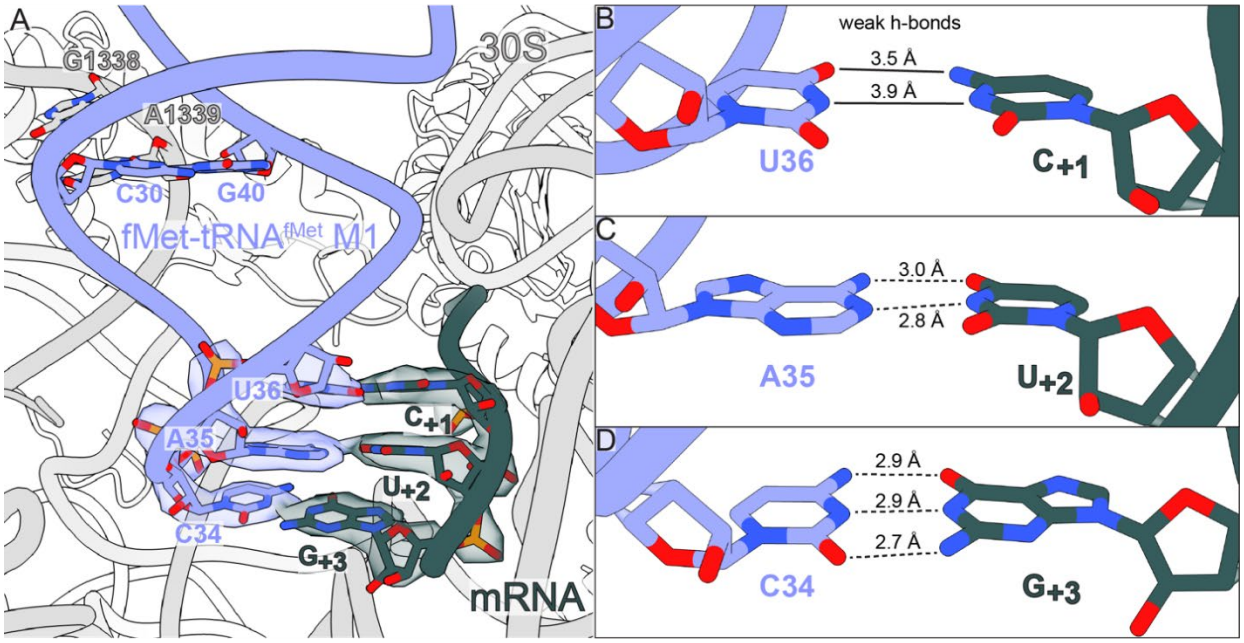

Figure 4. Codon-anticodon interactions between tRNA^{fMet} M1 and the CUG start codon in the absence of IF2. A. The CAU anticodon of tRNA^{fMet} M1 interacts with the noncanonical CUG start codon at the ribosomal P site (map threshold 0.21; map value range -0.877 to 1.41). B. Hydrogen-bond donors and acceptors are too distant for strong base pairing at the first position of the codon-anticodon interaction. C. Base pairing at the second position of the codon-anticodon interaction displays typical hydrogen bonding distances. D. Base pairing at the third position of the codon-anticodon interaction displays typical hydrogen bonding distances.

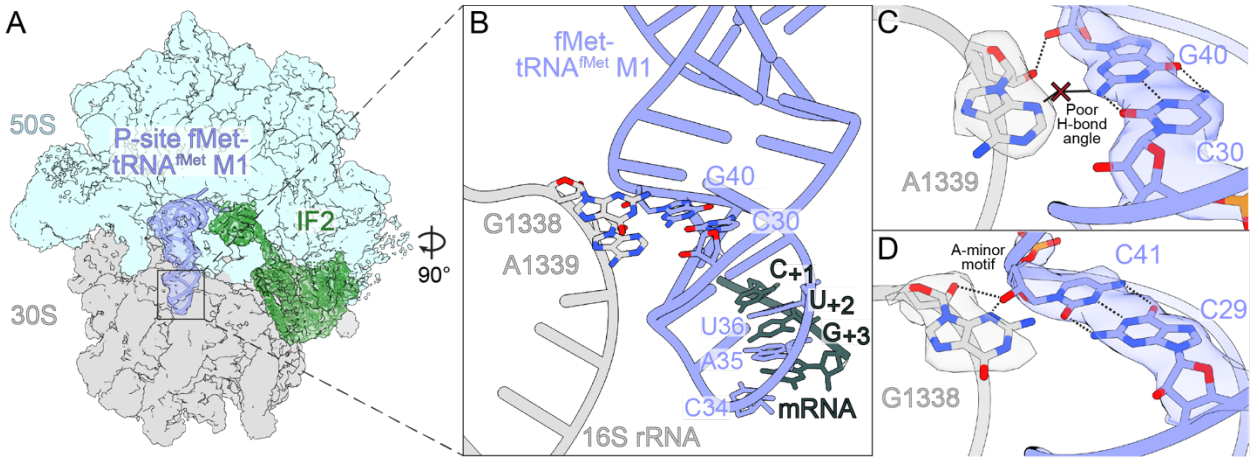

Fig. 5. IF2 partially restores gripping of tRNA^{fMet} M1 by the 16S rRNA. A. Map of 70S initiation complexes containing the IF2·GDPCP·fMet-tRNA^{fMet} M1 complex in the P site (tRNA and IF2 models and map segments superimposed for visibility). B. The tRNA^{fMet} M1 ASL containing the C30-G40 base pair interacts with 16S rRNA nucleotides A1339 and G1338 while maintaining base pairs with the CUG start codon. C. In the presence of IF2, the C30-G40 base pair is unable to form A-minor interactions with the nucleobase of A1339 (map threshold 5.0; map value range -11.3 to 28.2). D. In contrast, G1338 is oriented properly to form A-minor interactions with nucleotide C41 of the adjacent tRNA base pair (map threshold 4.6; map value range -11.3 to 28.2).

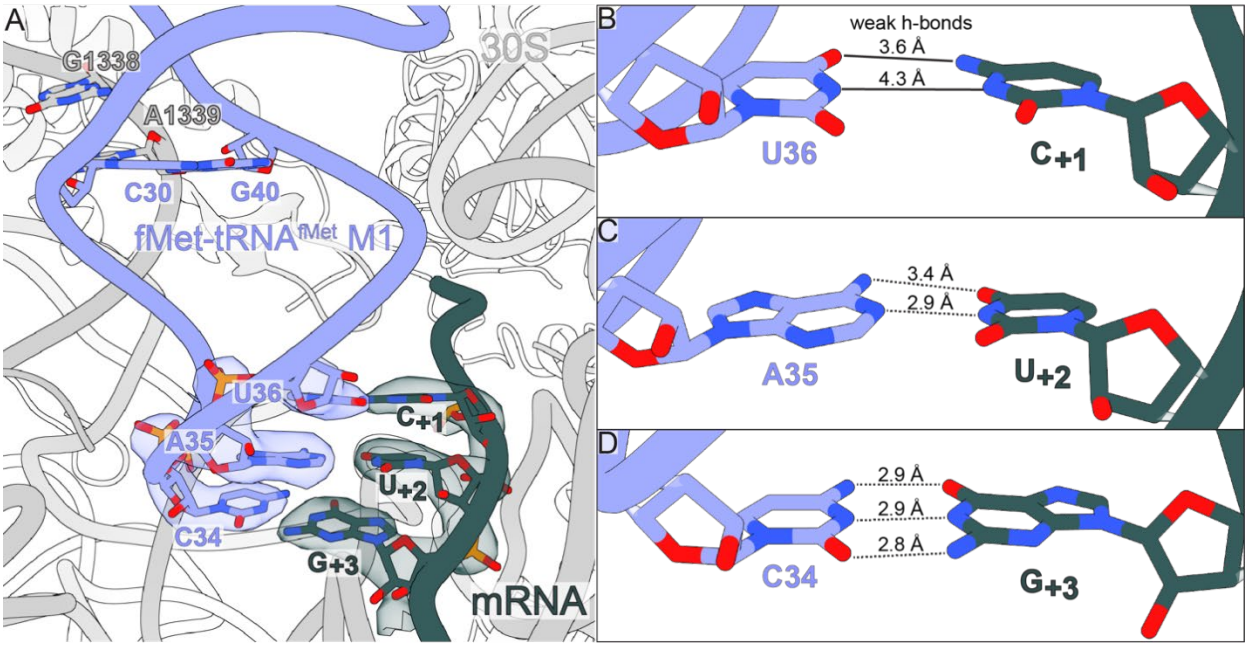

Figure 6. IF2 does not appear to strengthen the interaction between the tRNA^{fMet} M1 anticodon and the noncanonical CUG start codon. A. When IF2 is present, the CAU anticodon of tRNA^{fMet} M1 interacts with the P-site noncanonical CUG start codon (map threshold 4.5; map value range -11.3 to 28.2). B. IF2 interaction with tRNA^{fMet} M1 does not orient the first position codon-anticodon nucleotides closely enough for strong base pairing. C. Base pairing at the second position of the codon-anticodon interaction displays typical hydrogen bonding distances. D. Base pairing at the third position of the codon-anticodon interaction displays typical hydrogen bonding distances.

REFERENCES

1. Gualerzi, C. O., and Pon, C. L. (2015) Initiation of mRNA translation in bacteria: structural and dynamic aspects. *Cell Mol Life Sci* **72**, 4341-4367
2. Milon, P., Maracci, C., Filonava, L., Gualerzi, C. O., and Rodnina, M. V. (2012) Real-time assembly landscape of bacterial 30S translation initiation complex. *Nat Struct Mol Biol* **19**, 609-615
3. Caban, K., and Gonzalez, R. L., Jr. (2015) The emerging role of rectified thermal fluctuations in initiator aa-tRNA- and start codon selection during translation initiation. *Biochimie* **114**, 30-38
4. Milon, P., and Rodnina, M. V. (2012) Kinetic control of translation initiation in bacteria. *Crit Rev Biochem Mol Biol* **47**, 334-348
5. Wu, X. Q., and RajBhandary, U. L. (1997) Effect of the amino acid attached to Escherichia coli initiator tRNA on its affinity for the initiation factor IF2 and on the IF2 dependence of its binding to the ribosome. *J Biol Chem* **272**, 1891-1895
6. Kapp, L. D., Kolitz, S. E., and Lorsch, J. R. (2006) Yeast initiator tRNA identity elements cooperate to influence multiple steps of translation initiation. *RNA* **12**, 751-764
7. Marshall, C. B., Ho, J., Buerger, C., Plevin, M. J., Li, G. Y., Li, Z., Ikura, M., and Stambolic, V. (2009) Characterization of the intrinsic and TSC2-GAP-regulated GTPase activity of Rheb by real-time NMR. *Sci Signal* **2**, ra3
8. Sprink, T., Ramrath, D. J., Yamamoto, H., Yamamoto, K., Loerke, J., Ismer, J., Hildebrand, P. W., Scheerer, P., Burger, J., Mielke, T., and Spahn, C. M. (2016) Structures of ribosome-bound initiation factor 2 reveal the mechanism of subunit association. *Sci Adv* **2**, e1501502
9. Caban, K., Pavlov, M., Ehrenberg, M., and Gonzalez, R. L., Jr. (2017) A conformational switch in initiation factor 2 controls the fidelity of translation initiation in bacteria. *Nat Commun* **8**, 1475
10. Antoun, A., Pavlov, M. Y., Lovmar, M., and Ehrenberg, M. (2006) How initiation factors tune the rate of initiation of protein synthesis in bacteria. *EMBO J* **25**, 2539-2550
11. Shine, J., and Dalgarno, L. (1974) The 3'-terminal sequence of Escherichia coli 16S ribosomal RNA: complementarity to nonsense triplets and ribosome binding sites. *Proc Natl Acad Sci U S A* **71**, 1342-1346
12. Liu, Q., and Fredrick, K. (2015) Roles of helix H69 of 23S rRNA in translation initiation. *Proc Natl Acad Sci U S A* **112**, 11559-11564
13. Selmer, M., Dunham, C. M., Murphy, F. V. t., Weixlbaumer, A., Petry, S., Kelley, A. C., Weir, J. R., and Ramakrishnan, V. (2006) Structure of the 70S ribosome complexed with mRNA and tRNA. *Science* **313**, 1935-1942
14. Mayer, C., Stortchevoi, A., Kohrer, C., Varshney, U., and RajBhandary, U. L. (2001) Initiator tRNA and its role in initiation of protein synthesis. *Cold Spring Harb Symp Quant Biol* **66**, 195-206
15. Blanquet, S., Dessen, P., and Kahn, D. (1984) Properties and specificity of methionyl-tRNAfMet formyltransferase from Escherichia coli. *Methods Enzymol* **106**, 141-152
16. Szkaradkiewicz, K., Zuleeg, T., Limmer, S., and Sprinzl, M. (2000) Interaction of fMet-tRNAfMet and fMet-AMP with the C-terminal domain of Thermus thermophilus translation initiation factor 2. *Eur J Biochem* **267**, 4290-4299
17. Lancaster, L., and Noller, H. F. (2005) Involvement of 16S rRNA nucleotides G1338 and A1339 in discrimination of initiator tRNA. *Mol Cell* **20**, 623-632
18. Abdi, N. M., and Fredrick, K. (2005) Contribution of 16S rRNA nucleotides forming the 30S subunit A and P sites to translation in Escherichia coli. *Rna* **11**, 1624-1632
19. Qin, D., Abdi, N. M., and Fredrick, K. (2007) Characterization of 16S rRNA mutations that decrease the fidelity of translation initiation. *Rna* **13**, 2348-2355

20. Mandal, N., Mangroo, D., Dalluge, J. J., McCloskey, J. A., and Rajbhandary, U. L. (1996) Role of the three consecutive G:C base pairs conserved in the anticodon stem of initiator tRNAs in initiation of protein synthesis in Escherichia coli. *RNA* **2**, 473-482
21. Roy, B., Liu, Q., Shoji, S., and Fredrick, K. (2018) IF2 and unique features of initiator tRNA(fMet) help establish the translational reading frame. *RNA biology* **15**, 604-613
22. Hecht, A., Glasgow, J., Jaschke, P. R., Bawazer, L. A., Munson, M. S., Cochran, J. R., Endy, D., and Salit, M. (2017) Measurements of translation initiation from all 64 codons in E. coli. *Nucleic Acids Res* **45**, 3615-3626
23. Rodnina, M. V., and Wintermeyer, W. (2001) Fidelity of aminoacyl-tRNA selection on the ribosome: kinetic and structural mechanisms. *Annu Rev Biochem* **70**, 415-435
24. Ogle, J. M., Brodersen, D. E., Clemons, W. M., Jr., Tarry, M. J., Carter, A. P., and Ramakrishnan, V. (2001) Recognition of cognate transfer RNA by the 30S ribosomal subunit. *Science* **292**, 897-902
25. Hussain, T., Llacer, J. L., Wimberly, B. T., Kieft, J. S., and Ramakrishnan, V. (2016) Large-Scale Movements of IF3 and tRNA during Bacterial Translation Initiation. *Cell* **167**, 133-144 e113
26. Nasvall, S. J., Nilsson, K., and Bjork, G. R. (2009) The ribosomal grip of the peptidyl-tRNA is critical for reading frame maintenance. *Journal of molecular biology* **385**, 350-367
27. Atkins, J. F., Loughran, G., Bhatt, P. R., Firth, A. E., and Baranov, P. V. (2016) Ribosomal frameshifting and transcriptional slippage: From genetic steganography and cryptography to adventitious use. *Nucleic Acids Res*
28. Dunkle, J. A., and Dunham, C. M. (2015) Mechanisms of mRNA frame maintenance and its subversion during translation of the genetic code. *Biochimie* **114**, 90-96
29. Arora, S., Bhamidimarri, S. P., Bhattacharyya, M., Govindan, A., Weber, M. H., Vishveshwara, S., and Varshney, U. (2013) Distinctive contributions of the ribosomal P-site elements m2G966, m5C967 and the C-terminal tail of the S9 protein in the fidelity of initiation of translation in Escherichia coli. *Nucleic Acids Res* **41**, 4963-4975
30. Shoji, S., Abdi, N. M., Bundschuh, R., and Fredrick, K. (2009) Contribution of ribosomal residues to P-site tRNA binding. *Nucleic Acids Res*
31. Watson, Z. L., Ward, F. R., Meheust, R., Ad, O., Schepartz, A., Banfield, J. F., and Cate, J. H. (2020) Structure of the bacterial ribosome at 2 A resolution. *eLife* **9**
32. Hussain, T., Llacer, J. L., Fernandez, I. S., Munoz, A., Martin-Marcos, P., Savva, C. G., Lorsch, J. R., Hinnebusch, A. G., and Ramakrishnan, V. (2014) Structural changes enable start codon recognition by the eukaryotic translation initiation complex. *Cell* **159**, 597-607
33. Doherty, E. A., Batey, R. T., Masquida, B., and Doudna, J. A. (2001) A universal mode of helix packing in RNA. *Nat Struct Biol* **8**, 339-343
34. Svidritskiy, E., and Korostelev, A. A. (2015) Ribosome Structure Reveals Preservation of Active Sites in the Presence of a P-Site Wobble Mismatch. *Structure* **23**, 2155-2161
35. Nguyen, H. A., Hoffer, E. D., Fagan, C. E., Maehigashi, T., and Dunham, C. M. (2023) Structural basis for reduced ribosomal A-site fidelity in response to P-site codon-anticodon mismatches. *bioRxiv*
36. Baeyens, K. J., De Bondt, H. L., and Holbrook, S. R. (1995) Structure of an RNA double helix including uracil-uracil base pairs in an internal loop. *Nat Struct Biol* **2**, 56-62
37. Tanaka, Y., Fujii, S., Hiroaki, H., Sakata, T., Tanaka, T., Uesugi, S., Tomita, K., and Kyogoku, Y. (1999) A'-form RNA double helix in the single crystal structure of r(UGAGCUUCGGCUC). *Nucleic Acids Res* **27**, 949-955
38. Nguyen, H. A., Hoffer, E. D., and Dunham, C. M. (2019) Importance of a tRNA anticodon loop modification and a conserved, noncanonical anticodon stem pairing in tRNACGGProfor decoding. *J Biol Chem* **294**, 5281-5291

39. Hong, S., Sunita, S., Maehigashi, T., Hoffer, E. D., Dunkle, J. A., and Dunham, C. M. (2018) Mechanism of tRNA-mediated +1 ribosomal frameshifting. *Proc Natl Acad Sci U S A* **115**, 11226-11231
40. Walker, S. E., and Fredrick, K. (2008) Preparation and evaluation of acylated tRNAs. *Methods* **44**, 81-86
41. Punjani, A., Rubinstein, J. L., Fleet, D. J., and Brubaker, M. A. (2017) cryoSPARC: algorithms for rapid unsupervised cryo-EM structure determination. *Nat Methods* **14**, 290-296
42. Bepler, T., Morin, A., Rapp, M., Brasch, J., Shapiro, L., Noble, A. J., and Berger, B. (2019) Positive-unlabeled convolutional neural networks for particle picking in cryo-electron micrographs. *Nat Methods* **16**, 1153-1160
43. Zivanov, J., Nakane, T., and Scheres, S. H. W. (2019) A Bayesian approach to beam-induced motion correction in cryo-EM single-particle analysis. *IUCrJ* **6**, 5-17
44. Zivanov, J., Nakane, T., and Scheres, S. H. W. (2020) Estimation of high-order aberrations and anisotropic magnification from cryo-EM data sets in RELION-3.1. *IUCrJ* **7**, 253-267
45. Arenz, S., Bock, L. V., Graf, M., Innis, C. A., Beckmann, R., Grubmuller, H., Vaiana, A. C., and Wilson, D. N. (2016) A combined cryo-EM and molecular dynamics approach reveals the mechanism of ErmBL-mediated translation arrest. *Nature communications* **7**, 12026
46. Goddard, T. D., Huang, C. C., Meng, E. C., Pettersen, E. F., Couch, G. S., Morris, J. H., and Ferrin, T. E. (2018) UCSF ChimeraX: Meeting modern challenges in visualization and analysis. *Protein Sci* **27**, 14-25
47. Zivanov, J., Nakane, T., Forsberg, B. O., Kimanius, D., Hagen, W. J., Lindahl, E., and Scheres, S. H. (2018) New tools for automated high-resolution cryo-EM structure determination in RELION-3. *eLife* **7**
48. Rohou, A., and Grigorieff, N. (2015) CTFFIND4: Fast and accurate defocus estimation from electron micrographs. *J Struct Biol* **192**, 216-221
49. Kaledhonkar, S., Fu, Z., Caban, K., Li, W., Chen, B., Sun, M., Gonzalez, R. L., Jr., and Frank, J. (2019) Late steps in bacterial translation initiation visualized using time-resolved cryo-EM. *Nature* **570**, 400-404
50. Liebschner, D., Afonine, P. V., Baker, M. L., Bunkoczi, G., Chen, V. B., Croll, T. I., Hintze, B., Hung, L. W., Jain, S., McCoy, A. J., Moriarty, N. W., Oeffner, R. D., Poon, B. K., Prisant, M. G., Read, R. J., Richardson, J. S., Richardson, D. C., Sammito, M. D., Sobolev, O. V., Stockwell, D. H., Terwilliger, T. C., Urzhumtsev, A. G., Videau, L. L., Williams, C. J., and Adams, P. D. (2019) Macromolecular structure determination using X-rays, neutrons and electrons: recent developments in Phenix. *Acta Crystallogr D Struct Biol* **75**, 861-877
51. Moriarty, N. W., Grosse-Kunstleve, R. W., and Adams, P. D. (2009) electronic Ligand Builder and Optimization Workbench (eLBOW): a tool for ligand coordinate and restraint generation. *Acta crystallographica* **65**, 1074-1080
52. Emsley, P., and Cowtan, K. (2004) Coot: model-building tools for molecular graphics. *Acta crystallographica* **60**, 2126-2132
53. Williams, C. J., Headd, J. J., Moriarty, N. W., Prisant, M. G., Videau, L. L., Deis, L. N., Verma, V., Keedy, D. A., Hintze, B. J., Chen, V. B., Jain, S., Lewis, S. M., Arendall, W. B., 3rd, Snoeyink, J., Adams, P. D., Lovell, S. C., Richardson, J. S., and Richardson, D. C. (2018) MolProbity: More and better reference data for improved all-atom structure validation. *Protein Sci* **27**, 293-315
54. Chen, V. B., Arendall, W. B., 3rd, Headd, J. J., Keedy, D. A., Immormino, R. M., Kapral, G. J., Murray, L. W., Richardson, J. S., and Richardson, D. C. (2010) MolProbity: all-atom structure validation for macromolecular crystallography. *Acta crystallographica* **66**, 12-21

Structural analysis of noncanonical translation initiation complexes

Jacob M. Mattingly[1,2], Ha An Nguyen[1], Bappaditya Roy[3], Kurt Fredrick[3] and Christine M. Dunham[1,*]

[1]Department of Chemistry, Emory University, Atlanta, GA, USA
[2]Graduate Program in Biochemistry, Cell and Developmental Biology, Emory University, Atlanta, GA, USA
[3]Department of Microbiology and Center for RNA Biology, The Ohio State University, Columbus, Ohio, USA

SUPPLEMENTARY DATA FILE

Figures S1-S11

Tables S1-S6

Data deposition: Atomic coordinates, and structure factors have been deposited in the Protein Data Bank, www.pdb.org and Electron Microscopy Data Bank (EMDB): (PDB codes 9AX7, 9AX8, 9CG5, 9CG6, 9CG7; EMDB codes EMD-43929, EMD-43930, EMD-45569, EMD-45572, EMD-45573)

Key words: protein synthesis**,** translation initiation, $tRNA^{fMet}$, A-minor motif, 16S rRNA

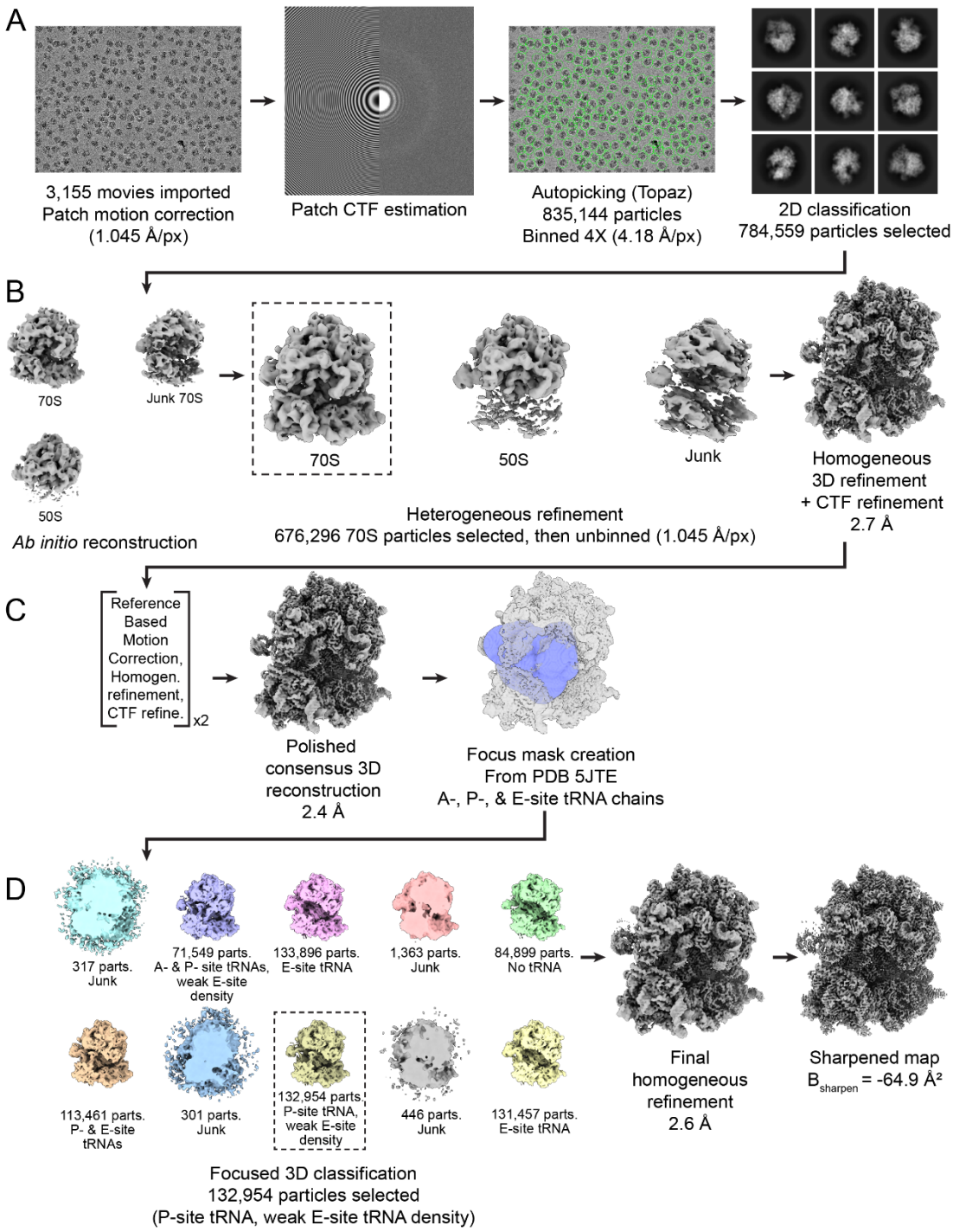

Fig S1. Cryo-EM data processing pipeline (*E. coli* 70S + tRNA^{fMet} M1 + CUG mRNA, no IF2).

A. Micrograph preprocessing, particle picking, and reference-free two-dimensional classification. B. *Ab initio* 3D reconstruction of 2D-classified ribosome-like particles, heterogeneous refinement, and initial 3D refinement of selected 70S ribosome particles. C. Iterative reference-based motion

correction, homogeneous refinement, and CTF refinement steps to yield a resolution-optimized particle set. Focus mask creation (covering the ribosomal A, P, and E sites) D. Focused 3D classification followed by final homogeneous refinement of selected particles with P-site tRNA and minimal E-site density and B-factor sharpening of the resultant map.

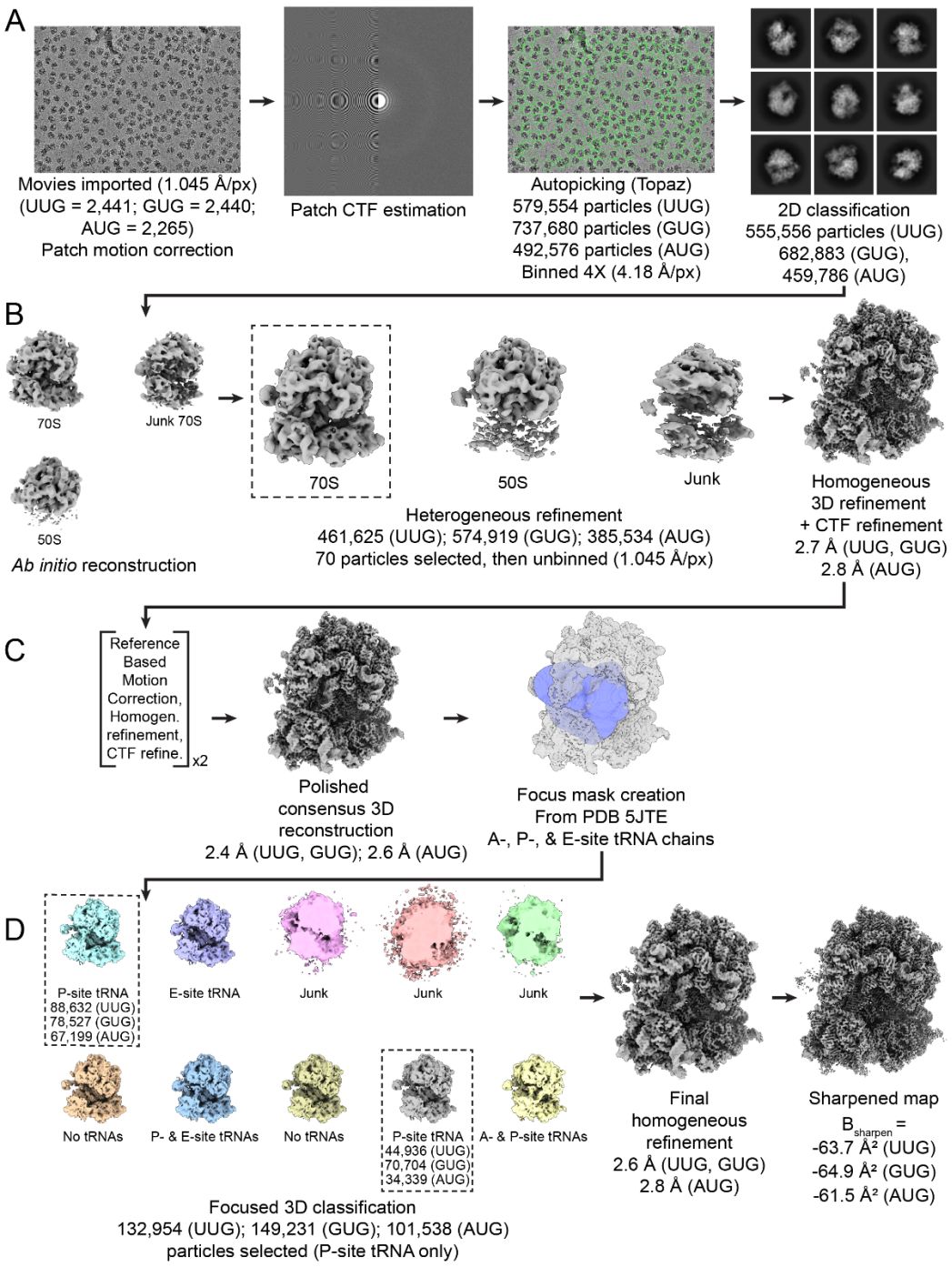

Fig. S2. Cryo-EM data processing pipeline (*E. coli* 70S + tRNA^{fMet} M1 + UUG/GUG/AUG mRNA, no IF2 datasets; UUG dataset shown as examples). A. Micrograph preprocessing, particle picking, and reference-free two-dimensional classification. B. *Ab initio* 3D reconstruction of 2D-classified ribosome-like particles, heterogeneous refinement, and initial 3D refinement of selected 70S ribosome particles. C. Iterative reference-based motion correction, homogeneous

refinement, and CTF refinement steps to yield a resolution-optimized particle set. Focus mask creation (covering the ribosomal A, P, and E sites) D. Focused 3D classification followed by final homogeneous refinement of selected particles with only P-site tRNA and B-factor sharpening of the resultant map.

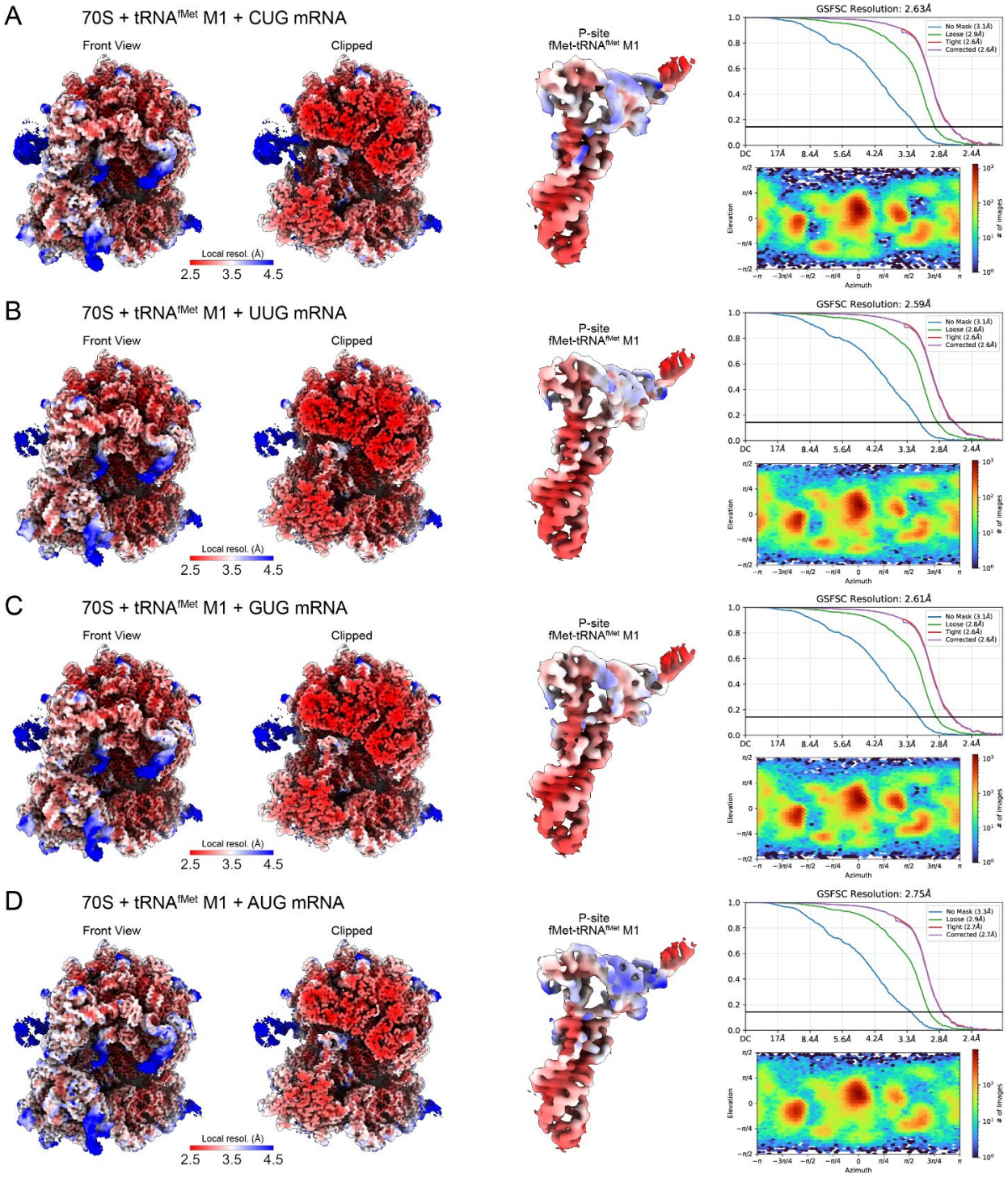

Fig. S3. Data quality metrics (*E. coli* 70S + tRNA^{fMet} M1, no IF2 datasets). A. Data quality metrics for CUG start codon dataset; local resolution maps correspond to 70S front view (left), clipped view for visibility of tRNA binding sites (middle), and zoomed view of P-site fMet-tRNA^{fMet} M1 (right); Fourier shell correlation plot (upper) and orientation distribution plot (lower) from final

homogeneous 3D refinement. B. Data quality metrics for UUG start codon dataset. C. Data quality metrics for GUG start codon dataset. D. Data quality metrics for AUG start codon dataset.

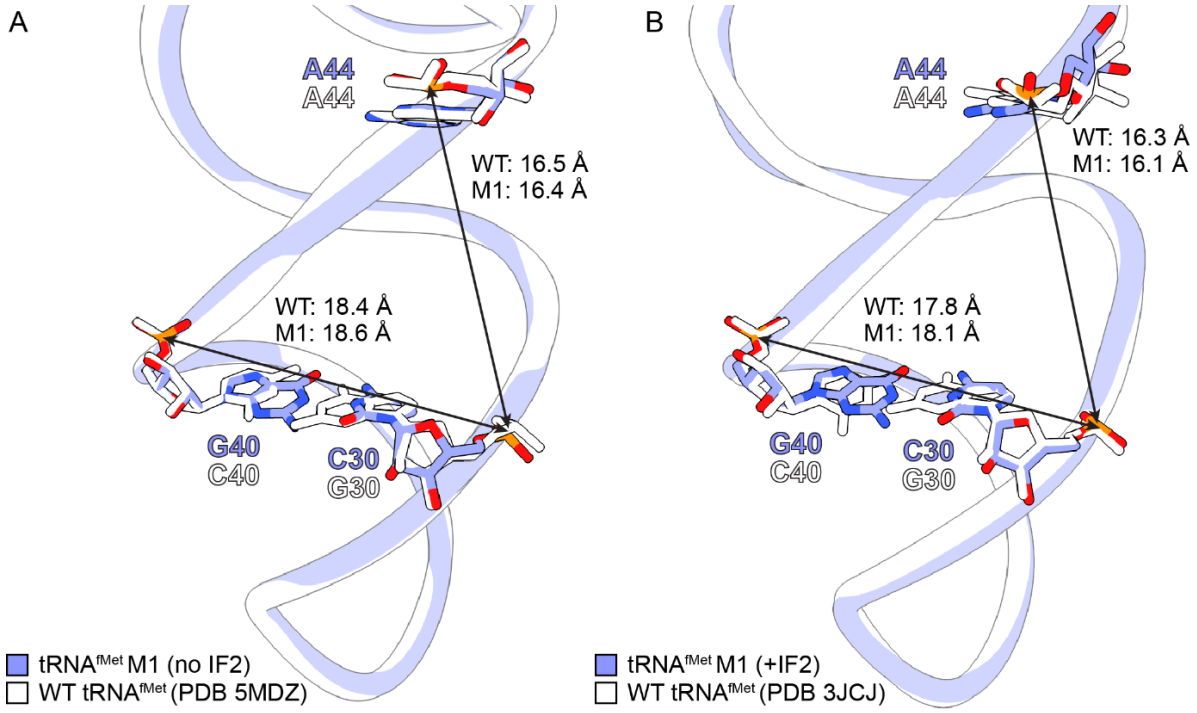

Fig. S4. The M1 mutation does not alter tRNA^{fMet} ASL width or pitch. A. tRNA^{fMet} M1 from 70S ICs prepared without IF2 and WT tRNA^{fMet} from PDB 5MDZ with phosphorus-phosphorus distances measured between nucleotides 30 and 40 (ASL width) and nucleotides 30 and 44 (ASL pitch). B. A. tRNA^{fMet} M1 from 70S ICs containing IF2·GDPCP and WT tRNA^{fMet} from PDB 3JCJ with phosphorus-phosphorus distances measured between nucleotides 30 and 40 (ASL width) and nucleotides 30 and 44 (ASL pitch).

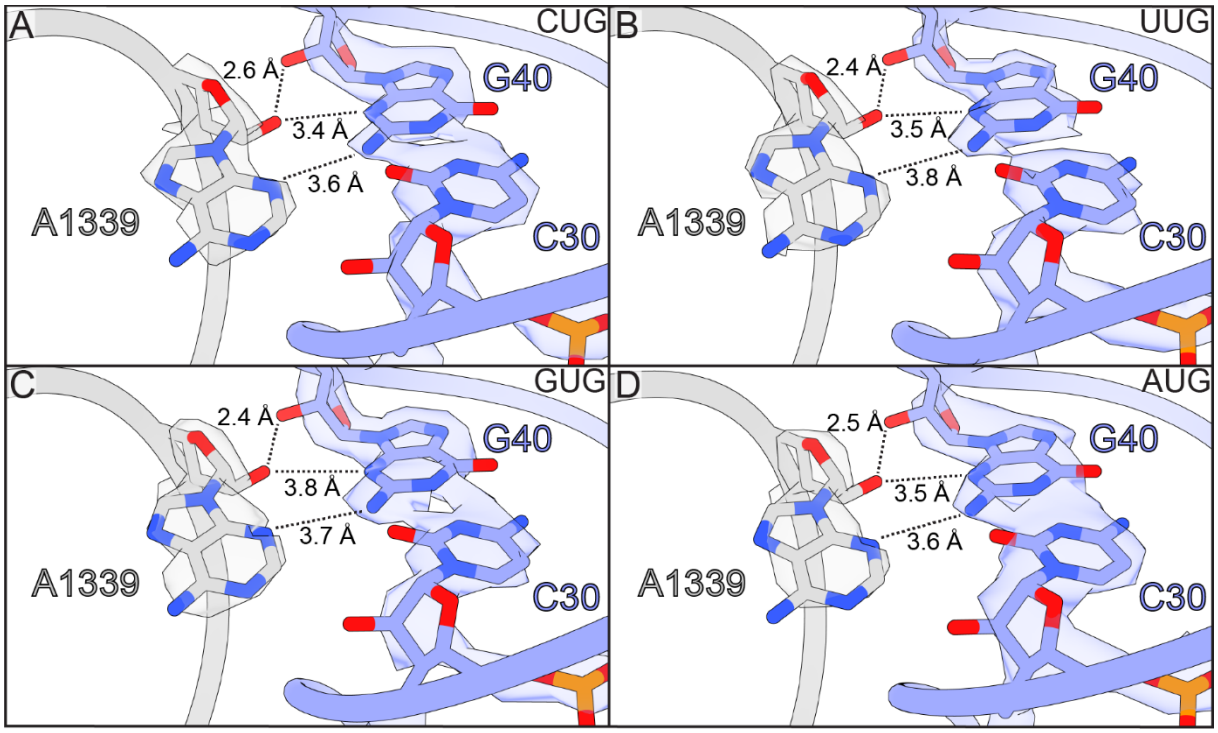

Fig. S5. A-minor interactions between 16S rRNA nucleotide A1339 and the tRNA^{fMet} M1 30-40 base pair are similar in the presence of all NUG start codons. A. A-minor interaction of A1339 with the tRNA^{fMet} M1 30-40 base pair (CUG start codon, map threshold 0.26, map value range -0.877 to 1.41). B. A-minor interaction of A1339 with the tRNA^{fMet} M1 30-40 base pair (UUG start codon, map threshold 0.26, map value range -0.785 to 1.38). C. A-minor interaction of A1339 with the tRNA^{fMet} M1 30-40 base pair (GUG start codon, map threshold 0.26, map value range -0.745 to 1.33). D. A-minor interaction of A1339 with the tRNA^{fMet} M1 30-40 base pair (AUG start codon, map threshold 0.20, map value range -0.527 to 1.03).

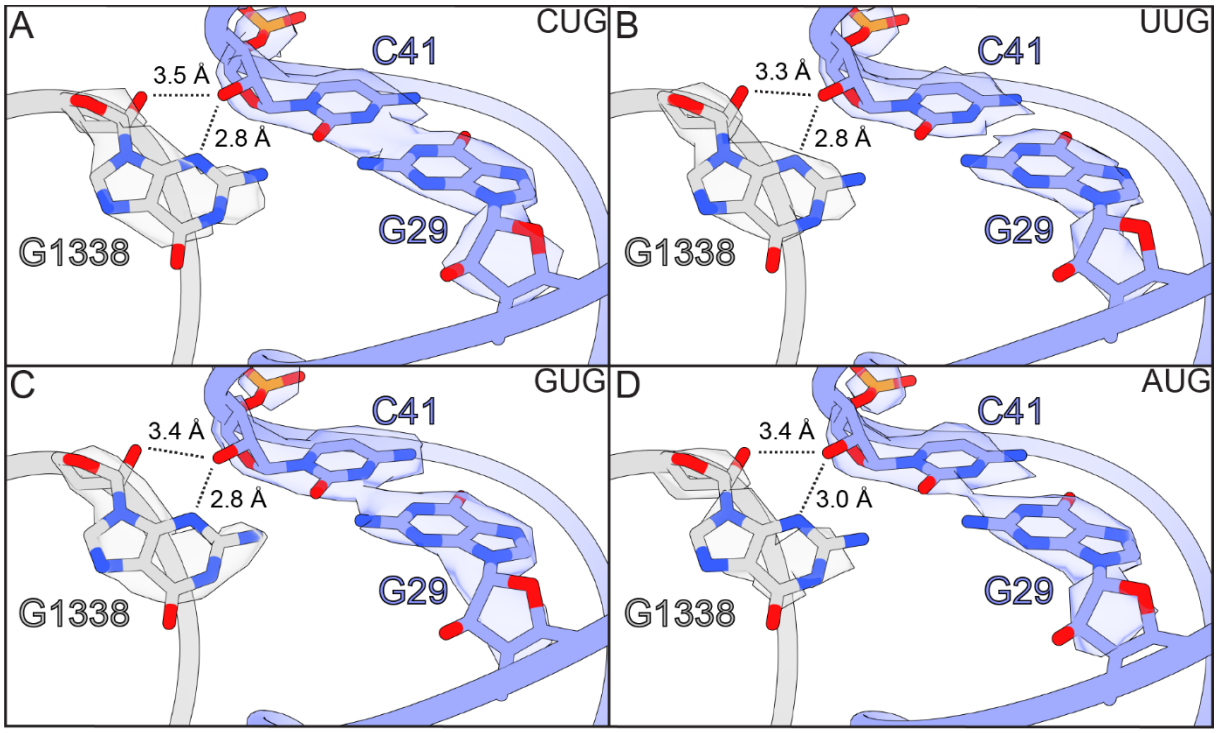

Fig. S6. A-minor interactions between 16S rRNA nucleotide G1338 and tRNA^{fMet} M1 nucleotide C41 are similar in the presence of all NUG start codons. A. A-minor interaction of G1338 with tRNA^{fMet} M1 nucleotide C41 (CUG start codon, map threshold 0.28, map value range -0.877 to 1.41). B. A-minor interaction of G1338 with tRNA^{fMet} M1 nucleotide C41 (UUG start codon, map threshold 0.26, map value range -0.785 to 1.38). C. A-minor interaction of G1338 with tRNA^{fMet} M1 nucleotide C41 (GUG start codon, map threshold 0.26, map value range -0.745 to 1.33). D. A-minor interaction of G1338 with tRNA^{fMet} M1 nucleotide C41 (AUG start codon, map threshold 0.22, map value range -0.527 to 1.03).

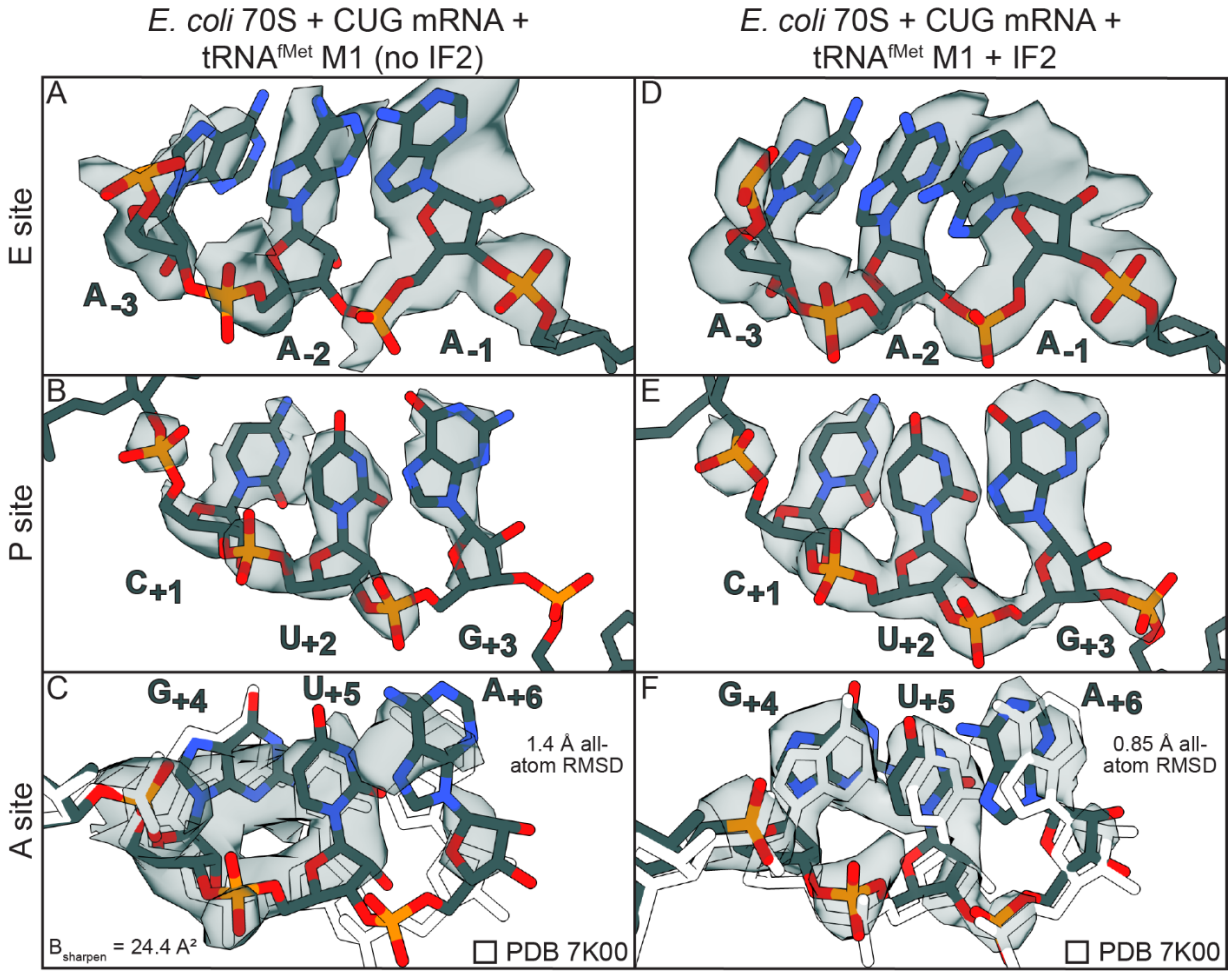

Fig. S7. 70S complexes are observed in the 0 reading frame with functionally presented A-site mRNA codons. A. E-site mRNA codon map and model (no-IF2, CUG start codon structure; map threshold 0.13, map value range -0.877 to 1.41). B. P-site mRNA codon map and model (no-IF2, CUG start codon structure; map threshold 0.3). C. A-site mRNA codon model and alternative sharpened map generated using PHENIX Autosharpen (no-IF2, CUG start codon structure with A-site codon from PDB 7K00 superimposed; global sharpening B-factor of 24.41 Å^2, map threshold 2.9, map value range -13.7 to 29.8). Models were aligned on their 16S rRNA platform domains for measurement of an all-atom RMSD for their A-site codons. D. E-site mRNA codon map and model (+IF2 structure; map threshold 2.9, map value range -11.3 to 28.2). E . P-site mRNA codon map and model (+IF2 structure; map threshold 4.5).). F. A-site mRNA codon map and model (+IF2, CUG start codon structure A-site mRNA codon from PDB 7K00 superimposed;

map threshold 2.4). Models were aligned on their 16S rRNA platform domains for measurement of an all-atom RMSD for their A-site codons.

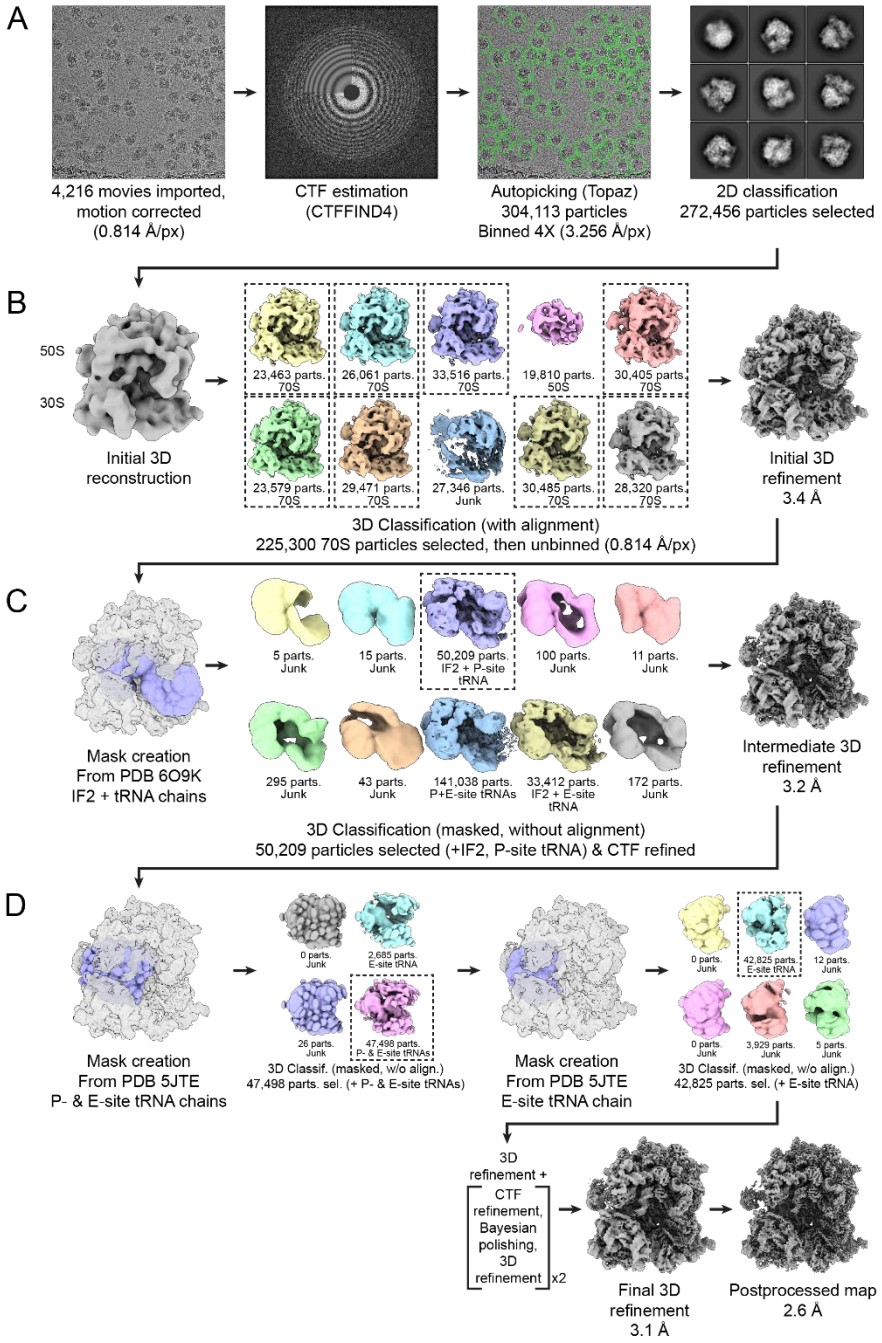

Fig. S8. Cryo-EM data processing pipeline (*E. coli* 70S + tRNA^{fMet} M1 + IF2). A. Micrograph preprocessing, particle picking, and reference-free two-dimensional classification. B. Initial 3D reconstruction of 2D-classified ribosome-like particles, three-dimensional classification with particle alignment, and initial 3D refinement of selected 70S ribosome particles. C. Mask creation (covering the IF2 binding site and ribosomal P site), followed by focused three-dimensional

classification without particle alignment and 3D refinement of selected IF2-containing particles. D. Mask creation (covering the ribosomal P and E sites), focused 3D classification without alignment, additional focused classification with a mask covering the ribosomal E site, and final CTF refinement, Bayesian particle polishing, 3D refinement, and postprocessing steps to yield a 2.6 Å 3D reconstruction.

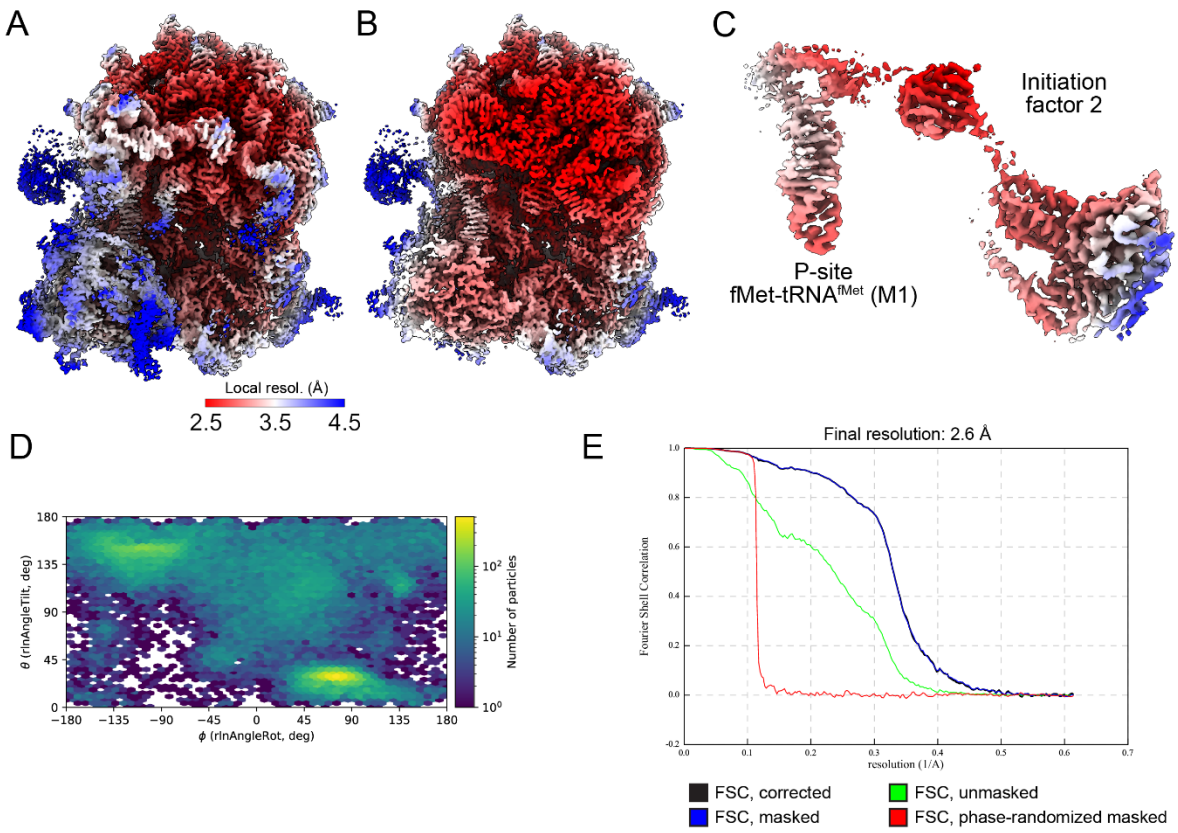

Fig. S9. Data quality metrics (*E. coli* 70S + tRNA^{fMet} M1 + IF2). A. Local resolution map (external view) generated using RELION-3.1's local resolution estimation implementation. B. Local resolution map with clipping plane applied for visibility of bound P-site fMet-tRNA^{fMet} M1 and IF2. C. Local resolution of fMet-tRNA^{fMet} M1 and IF2 map fragments extracted from final 3D reconstruction displayed in (A). D. Angular distribution plot of 42,825 IF2-containing particles generated using AngDist. E. Fourier shell correlation plot from RELION-3.1 postprocessing job yielding a resolution of 2.6 Å at the FSC=0.143 cutoff upon application of a solvent mask.

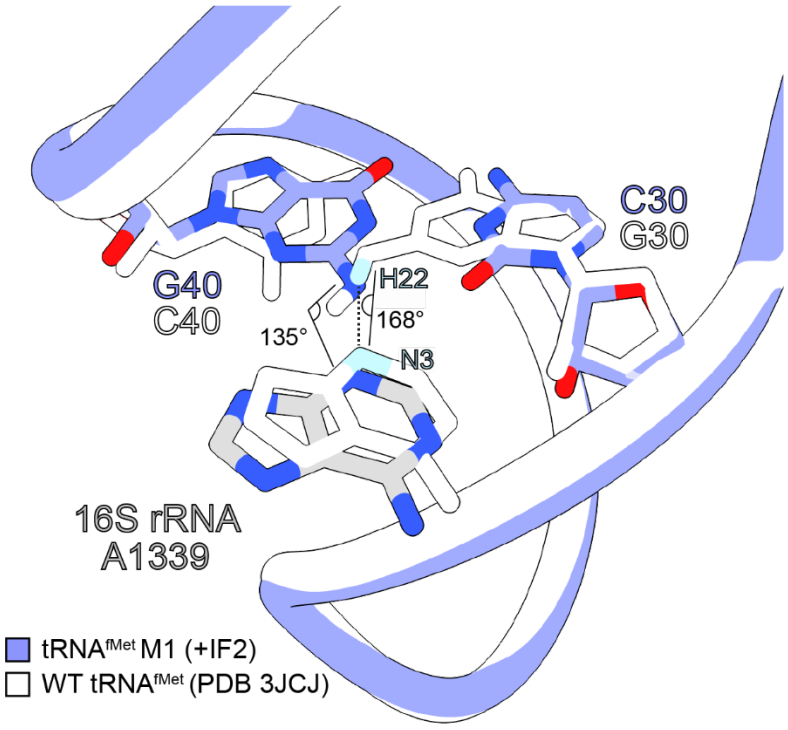

Fig. S10. The M1 mutation appears to weaken tRNA^{fMet} interaction with 16S nucleotide A1339 by reducing hydrogen bonding angles with the 30-40 base pair. IF2 binding to complexes containing tRNA^{fMet} M1 does not improve the linearity of hydrogen bonding between A1339 and the 30-40 base pair.

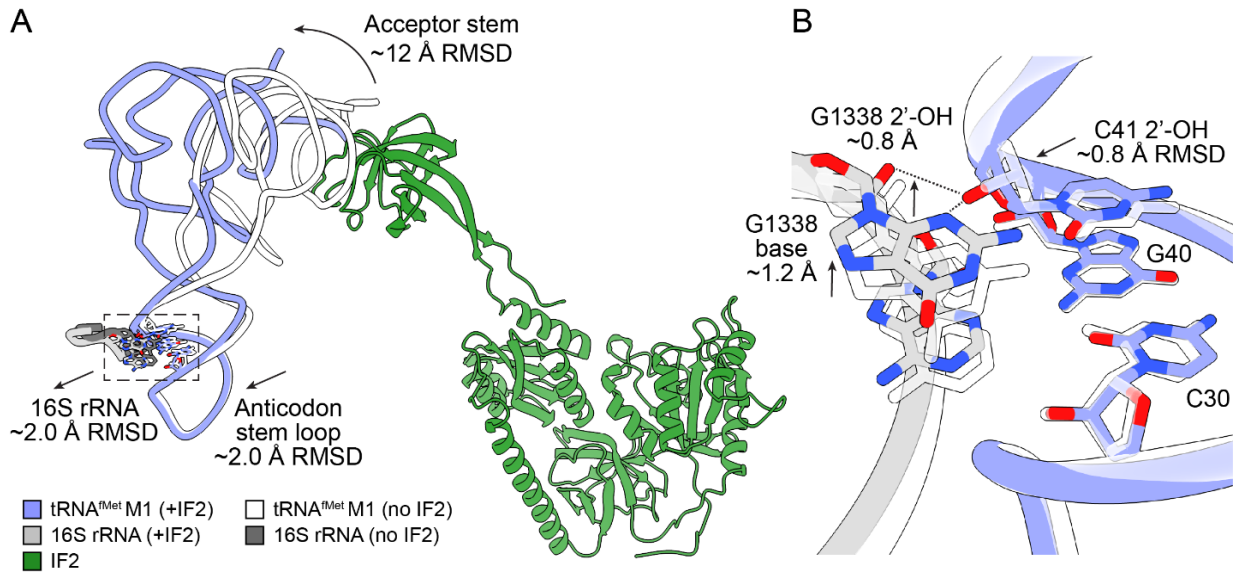

Fig. S11. IF2 improves the interaction between 16S rRNA and the tRNA^{fMet} M1 minor groove. A. When IF2 is present, the acceptor stem of tRNA^{fMet} M1 is displaced ~12 Å toward the ribosomal E site while the anticodon stem loop is displaced roughly 2 Å toward the ribosomal 30S head domain. The single-stranded 16S rRNA loop containing NTs 1335-1339 is displaced roughly 2 Å along with the tRNA^{fMet} M1 ASL when IF2 is present (structures aligned on the 16S rRNA platform domain). B. The interaction of IF2 with tRNA^{fMet} M1 during initiation displaces the 2'-OH of ASL nucleotide C41 roughly 0.8 Å toward the 16S rRNA, the 16S nucleotide G1338 base roughly 1.2 Å upward along the tRNA minor groove, and G1338 2'-OH 0.8 Å upward along the minor groove relative to the C30-G40 base pair, slightly strengthening tRNA gripping by the ribosomal P site (structures aligned on the tRNA^{fMet} M1 C30-G40 base pair).

Table S1. Cryo-EM data collection and model statistics for the *E. coli* 70S + tRNA^{fMet} M1 + CUG start codon dataset (no IF2).

EMDB accession	**EMD-43929**	
PDB ID	**9AX7**	
Name	**70S IC (tRNA^{fMet} M1 + CUG start codon)**	
Data collection		
Microscope	FEI Talos Arctica	
Detector	Gatan K3 Bioquantum	
Voltage (keV)	200	
Electron exposure ($e^-/Å^2$)	58.4	
Pixel size (Å)	1.045	
Defocus range (μm)	-0.6-1.8	
Frames per movie	40	
Micrographs (#)	3,155	
Initial particles (#)	835,144	
Final particles (#)	132,954	
Model refinement and validation statistics		
Composition (#)		
Atoms	140,102	
Residues	Protein: 5,585; Nucleotide: 4,472	
Ligands	Mg: 394 Zn: 2	
Bonds (RMSD)		
Length (Å) (# > 4σ)	0.003 (0)	
Angles (°) (# > 4σ)	0.651 (2)	
MolProbity score	1.59	
Clash score	7.43	
Ramachandran plot (%)		
Outliers	0.04	
Allowed	3.00	
Favored	96.97	
Rotamer outliers (%)	0.28	
Cβ outliers (%)	0.00	
Peptide plane (%)		
Cis proline/general	2.2/0.0	
Twisted proline/general	0.0/0.0	
CaBLAM outliers (%)	1.80	
ADP (B-factors)	min/max/mean	
Protein	0.00/109.35/43.20	
Nucleotide	0.00/152.32/34.10	
Ligand	0.22/82.03/24.98	
Resolution Estimates (Å)	Masked	Unmasked
d FSC (half maps; 0.143)	2.8	2.9
d 99 (full/half1/half2)	2.9/2.1/2.1	2.8/2.1/2.1
d model	2.9	2.9
d FSC model (0/0.143/0.5)	2.6/2.6/2.8	2.6/2.6/3.0
Map min/max/mean	-0.88/1.41/0.01	
Model vs. Data		
CC (mask)	0.85	

Table S2. Cryo-EM data collection and model statistics for the *E. coli* 70S + tRNA^{fMet} M1 + UUG start codon dataset.

EMDB accession	**EMD-45569**	
PDB ID	**9CG5**	
Name	**70S IC (tRNA^{fMet} M1 + UUG start codon)**	
Data collection		
Microscope	FEI Talos Arctica	
Detector	Gatan K3 Bioquantum	
Voltage (keV)	200	
Electron exposure ($e^-/Å^2$)	58.4	
Pixel size (Å)	1.045	
Defocus range (μm)	-0.6-1.8	
Frames per movie	40	
Micrographs (#)	2,441	
Initial particles (#)	579,544	
Final particles (#)	133,568	
Model refinement and validation statistics		
Composition (#)		
Atoms	140,102	
Residues	Protein: 5,585; Nucleotide: 4,472	
Ligands	Mg: 309 Zn: 2	
Bonds (RMSD)		
Length (Å) (# > 4σ)	0.008 (2)	
Angles (°) (# > 4σ)	0.834 (4)	
MolProbity score	1.66	
Clash score	7.00	
Ramachandran plot (%)		
Outliers	0.11	
Allowed	3.87	
Favored	96.02	
Rotamer outliers (%)	0.94	
Cβ outliers (%)	0.00	
Peptide plane (%)		
Cis proline/general	2.2/0.0	
Twisted proline/general	0.0/0.0	
CaBLAM outliers (%)	1.91	
ADP (B-factors)	min/max/mean	
Protein	0.00/107.75/39.90	
Nucleotide	0.00/125.66/32.79	
Ligand	0.00/76.48/23.21	
Resolution Estimates (Å)	Masked	Unmasked
d FSC (half maps; 0.143)	2.7	2.9
d 99 (full/half1/half2)	2.8/2.1/2.1	2.7/2.1/2.1
d model	2.9	2.9
d FSC model (0/0.143/0.5)	2.6/2.6/2.8	2.6/2.6/2.9
Map min/max/mean	-0.78/1.38/0.01	
Model vs. Data		
CC (mask)	0.87	

Table S3. Cryo-EM data collection and model statistics for the *E. coli* 70S + tRNA^{fMet} M1 + GUG start codon dataset.

EMDB accession	**EMD-45572**	
PDB ID	**9CG6**	
Name	**70S IC (tRNA^{fMet} M1 + GUG start codon)**	
Data collection		
Microscope	FEI Talos Arctica	
Detector	Gatan K3 Bioquantum	
Voltage (keV)	200	
Electron exposure (e$^-$/Å^2)	58.4	
Pixel size (Å)	1.045	
Defocus range (μm)	-0.6-1.8	
Frames per movie	40	
Micrographs (#)	2,440	
Initial particles (#)	737,680	
Final particles (#)	149,231	
Model refinement and validation statistics		
Composition (#)		
Atoms	140,105	
Residues	Protein: 5,585; Nucleotide: 4,447	
Ligands	Mg: 309 Zn: 2	
Bonds (RMSD)		
Length (Å) (# > 4σ)	0.007 (2)	
Angles (°) (# > 4σ)	0.797 (11)	
MolProbity score	1.64	
Clash score	6.85	
Ramachandran plot (%)		
Outliers	0.15	
Allowed	3.73	
Favored	96.13	
Rotamer outliers (%)	1.01	
Cβ outliers (%)	0.00	
Peptide plane (%)		
Cis proline/general	2.2/0.0	
Twisted proline/general	0.0/0.0	
CaBLAM outliers (%)	2.08	
ADP (B-factors)	min/max/mean	
Protein	0.00/110.95/41.08	
Nucleotide	0.00/123.13/33.55	
Ligand	0.61/78.92/24.25	
Resolution Estimates (Å)	Masked	Unmasked
d FSC (half maps; 0.143)	2.7	2.9
d 99 (full/half1/half2)	2.9/2.2/2.2	2.8/2.1/2.1
d model	2.9	2.9
d FSC model (0/0.143/0.5)	2.6/2.6/2.8	2.6/2.6/2.9
Map min/max/mean	-0.74/1.33/0.01	
Model vs. Data		
CC (mask)	0.87	

Table S4. Cryo-EM data collection and model statistics for the *E. coli* 70S + tRNA^{fMet} M1 + AUG start codon dataset.

EMDB accession	**EMD-45573**	
PDB ID	**9CG7**	
Name	**70S IC (tRNA^{fMet} M1 + AUG start codon)**	
Data collection		
Microscope	FEI Talos Arctica	
Detector	Gatan K3 Bioquantum	
Voltage (keV)	200	
Electron exposure ($e^-/Å^2$)	58.4	
Pixel size (Å)	1.045	
Defocus range (μm)	-0.6-1.8	
Frames per movie	40	
Micrographs (#)	2,265	
Initial particles (#)	492,576	
Final particles (#)	101,538	
Model refinement and validation statistics		
Composition (#)		
Atoms	140,104	
Residues	Protein: 5,585; Nucleotide: 4,447	
Ligands	Mg: 309 Zn: 2	
Bonds (RMSD)		
Length (Å) (# > 4σ)	0.007 (7)	
Angles (°) (# > 4σ)	0.776 (4)	
MolProbity score	1.64	
Clash score	6.43	
Ramachandran plot (%)		
Outliers	0.11	
Allowed	4.06	
Favored	95.83	
Rotamer outliers (%)	0.37	
Cβ outliers (%)	0.00	
Peptide plane (%)		
Cis proline/general	2.2/0.0	
Twisted proline/general	0.0/0.0	
CaBLAM outliers (%)	2.10	
ADP (B-factors)	min/max/mean	
Protein	0.00/111.21/43.18	
Nucleotide	0.00/114.69/40.32	
Ligand	4.42/83.88/25.80	
Resolution Estimates (Å)	Masked	Unmasked
d FSC (half maps; 0.143)	2.9	3.0
d 99 (full/half1/half2)	3.0/2.1/2.1	2.9/2.1/2.1
d model	3.0	2.9
d FSC model (0/0.143/0.5)	2.7/2.7/2.9	2.7/2.7/3.0
Map min/max/mean	-0.53/1.03/0.01	
Model vs. Data		
CC (mask)	0.87	

Table S5. Cryo-EM data collection and model statistics for the *E. coli* 70S + tRNA^{fMet} M1 + IF2·GDPCP + CUG start codon dataset.

EMDB accession	**EMD-43930**	
PDB ID	**9AX8**	
Name	**70S IC (tRNA^{fMet} M1, IF2·GDPCP + CUG start codon)**	
Data collection		
Microscope	TFS Krios	
Detector	TFS Falcon 4i	
Voltage (keV)	300	
Electron exposure (e^-/Å^2)	50	
Pixel size (Å)	0.814	
Defocus range (μm)	-0.5-2.5	
Frames per movie	29	
Micrographs (#)	4,216	
Initial particles (#)	304,113	
Final particles (#)	42,825	
Model refinement and validation statistics		
Composition (#)		
Atoms	145,067	
Residues	Protein: 5,904; Nucleotide: 4,597	
Ligands	Mg: 287 GDPCP: 1	
Bonds (RMSD)		
Length (Å) (# > 4σ)	0.003 (7)	
Angles (°) (# > 4σ)	0.661 (19)	
MolProbity score	2.29	
Clash score	6.90	
Ramachandran plot (%)		
Outliers	0.76	
Allowed	7.95	
Favored	91.29	
Rotamer outliers (%)	3.32	
Cβ outliers (%)	0.00	
Peptide plane (%)		
Cis proline/general	0.0/0.0	
Twisted proline/general	0.0/0.0	
CaBLAM outliers (%)	5.83	
ADP (B-factors)	min/max/mean	
Protein	10.51/182.48/66.46	
Nucleotide	0.00/356.69/80.36	
Ligand	9.69/79.47/34.34	
Resolution Estimates (Å)	Masked	Unmasked
d FSC (half maps; 0.143)	2.6	2.9
d 99 (full/half1/half2)	3.1/1.8/1.8	3.0/1.7/1.7
d model	2.9	2.9
d FSC model (0/0.143/0.5)	2.4/2.6/2.9	2.6/2.7/3.0
Map min/max/mean	-11.34/28.17/0.15	
Model vs. Data		
CC (mask)	0.86	

Table S6. Sequences of nucleic acids used in this study.

Name	Nucleotide sequence (5' → 3')	Source
mRNA (CUG)	GGCAAGGAAAUAAAACUGGUAUACUUU	Chemically synthesized (IDT)
mRNA (UUG)	GGCAAGGAAAUAAAAUUGGUAUACUUU	Chemically synthesized (IDT)
mRNA (GUG)	GGCAAGGAAAUAAAAGUGGUAUACUUU	Chemically synthesized (IDT)
mRNA (AUG)	GGCAAGGAAAUAAAAAUGGUAUACUUU	Chemically synthesized (IDT)

Chapter 3:

Basis for selective drug evasion of an aminoglycoside-resistance ribosomal RNA modification

Debayan Dey[1*], Jacob Mattingly[2,3*], Natalia Zelinskaya[1], Christine M. Dunham[2†] and Graeme L Conn[1†]

[1]Department of Biochemistry, Emory University School of Medicine, Atlanta, GA 30322
[2]Department of Chemistry, Emory University, Atlanta, GA 30322
[3]Graduate Program in Biochemistry, Cell, and Developmental Biology (BCDB), Emory University, Atlanta, GA 30322

*Co-first authors.
[†]Correspondence may be addressed to: Christine M. Dunham, cmdunha@emory.edu; or, Graeme L. Conn, gconn@emory.edu.

Key Words: antibiotic resistance, 16S rRNA, RNA methylation, aminoglycoside

This manuscript has been submitted to a journal and is currently awaiting review at time of submission of this dissertation. JM determined cryo-EM structures and made molecular model panels for figures. DD performed MIC assays and MD simulations and made . GC, DD, and JM assembled figures. All authors were involved in writing and editing the manuscript.

Abstract

Aminoglycosides disrupt the fidelity of protein synthesis by the bacterial ribosome, but their potent antibacterial activity is threatened by multiple resistance mechanisms, including methylation of their ribosomal RNA (rRNA) binding site. However, the impact of one such resistance-conferring methylation on N1 of helix 44 nucleotide A1408 (m^1A1408) is highly variable with some aminoglycosides retaining significant potency. Here, we examine bacterial susceptibility to a panel of diverse aminoglycosides, high-resolution electron cryomicroscopy structures of m^1A1408-modified 70S ribosome-aminoglycoside complexes, and molecular dynamics simulations to decipher the key determinants of such “resistance evasion”. Collectively, these analyses reveal how aminoglycosides adapt their conformation to accommodate m^1A1408, including the roles of specific ring substituents, balancing ligand strain and maintaining favorable interactions, and additional functional groups that make compensatory interactions for those disrupted by the modification. This work provides new design principles that can guide future rational development of aminoglycosides refractory to resistance conferred by rRNA modifications.

Introduction

Aminoglycosides are broad spectrum ribosome-targeting antibiotics with activity against both Gram-negative and Gram-positive bacteria[1,2]. Currently, aminoglycosides are in clinical use as last resort antibiotics for patients with severe or complicated infections (e.g. sepsis, infective endocarditis) including multidrug-resistant (MDR) Gram-negative infections, and for long-term treatment of chronic *Pseudomonas aeruginosa* lung infections associated with cystic fibrosis (CF)[3,4]. Broader application has been limited by aminoglycoside toxicity relative to other treatment options, but increasing resistance to these other drug classes has led to a reevaluation of aminoglycoside use[5-7]. However, continued use of aminoglycosides is also threatened by multiple resistance mechanisms including efflux and chemical modification of either the drugs or their ribosomal binding site[8-11].

Aminoglycosides bind 16S ribosomal RNA (rRNA) helix 44 (h44) at the aminoacyl-tRNA site (A site) within the conserved decoding center of the bacterial ribosome and typically induce mRNA misreading to disrupt the fidelity of protein synthesis, eventually resulting in cell death[1]. Aminoglycosides are polycationic oligosaccharides, with most containing a common 2-deoxystreptamine (2-DOS) ring (Ring II) appended with additional aminosugar rings (**Fig. 1**). The 2-DOS ring is connected at position 4 via a glycosidic bond to a modified α-glucose unit (Ring I) to form the disaccharide core that comprises the minimal fragment specifically able to bind to h44. Different classes of aminoglycosides are then distinguished based on the additional sugar linkages to the 2-DOS unit[2]. A second modified α-glucose unit (Ring III) at position 6 of the 2-DOS ring forms the 4,6-DOS aminoglycosides, including kanamycin and the clinically important drugs amikacin (Amk), tobramycin (Tob), gentamicin C1A (Gen), and plazomicin (Plz). Alternatively, appending position 5 of the 2-DOS ring with a β-D-ribosyl moiety forms the scaffold of the 4,5-DOS class of aminoglycosides, including the trisaccharides ribostamycin and butirosyn, tetrasaccharides neomycin (Neo) and paromomycin (Par; **Fig. 1**), and the pentasaccharide lividomicin.

Despite their potency and broad-spectrum activity, emergence of aminoglycoside resistance among pathogenic bacteria has critically impacted the clinical efficacy of this drug class. Prevalent resistance mechanisms include efflux mediated by resistance-nodulation-division family transporters in Gram-negative bacteria, drug modification by aminoglycoside-modification enzymes (AMEs), and ribosomal drug binding site mutation or chemical modification by the aminoglycoside-resistance 16S rRNA methyltransferases[9,11-13]. Countering the action of widespread AMEs has been the major focus of synthetic strategies to date, with alterations designed to restore aminoglycoside activity, such as in the recently approved Plz which is based on the sisomicin scaffold[14,15]. However, like established drugs of this class such as Tob and Amk, Plz–and likely future aminoglycoside variants developed using similar approaches–remain vulnerable to the action of aminoglycoside-resistance 16S rRNA methyltransferases which have

more recently emerged as another major clinical threat[10,14]. These rRNA modification enzymes methylate either the N1 position of residue A1408 (m^1A1408; NpmA and NpmB) or N7 position of G1405 (m^7G1405; ArmA and RmtA to RmtH) to render large groups of aminoglycosides ineffective[12,13,16]. Members of the m^7G1405 methyltransferase family have also been identified on plasmids encoding the NDM-1 β-lactamase, thus contributing to MDR in pathogenic bacteria including *Pseudomonas aeruginosa* and *Klebsiella pneumoniae*[17,18].

While m^7G1405 and m^1A1408 can confer near pan-aminoglycoside resistance, some aminoglycosides can, to varying extents, escape the effects of these two rRNA modifications. For example, the 4,5-DOS aminoglycosides are unaffected by m^7G1405 as Ring III does not project towards the modification site in this arrangement. Additionally, multiple reports of drug activity in bacteria expressing these enzymes have also suggested a propensity for certain aminoglycosides of both structural classes to partially evade the effect of the m^1A1408 modification[13,19,20]. Further, Kanazawa *et al.*[21] showed that G418 (also known as geneticin) and Par, both of which have a 6'-OH group, could bind to a model RNA helix that mimics the A site of the ribosome containing m^1A1408. In this context, the N1-methyl group of m^1A1408 and the 6′-OH group of Ring I of G418 and Par are close, suggesting better electrostatic and steric accommodation compared to Gen, which has a 6′-NH_3^+ group.

Fully defining the basis for the differential impacts of resistance rRNA modifications on the activity of structurally similar aminoglycosides could yield critical insights to guide rational redesign of this drug class to fully evade the rRNA modification resistance mechanism. However, we currently lack the necessary understanding of the structural and dynamic attributes of aminoglycosides upon interaction with modified, aminoglycoside-resistant ribosomes compared to their unmodified, fully drug sensitive counterparts. Here, we develop an experimental and computational framework to provide such information to thereby define the mechanistic basis of evasion of m^1A1408-mediated resistance by specific aminoglycosides. We find that strong evasion requires a combination of favorable interactions of specific ring substituents, ring

flexibility, and stabilization of drug-rRNA interaction by additional substituents such as the L-4-amino-2-hydroxybutyryl (L-HABA) moiety. Our studies also reveal why analogous evasion of the more clinically prevalent m^7G1405 resistance modification is not observed and provide a platform from which new aminoglycoside-based drugs could be designed to fully evade rRNA modification-mediated aminoglycoside resistance.

Results

Aminoglycosides exhibit a range of susceptibilities to m^1A1408 rRNA methylation.

Structurally and chemically diverse aminoglycosides were tested for activity in *E. coli* using minimum inhibitory concentration (MIC) assays in the absence or presence of m^1A1408 modification, *i.e.*, without or with expression of the aminoglycoside-resistance methyltransferase NpmA, respectively. As anticipated based on prior observations with a more limited set of aminoglycosides[13,19,20], a wide range of changes in drug sensitivity are observed in the presence of the modification (MIC range from 8 to >1024 μg/ml) compared to unmodified ribosomes (MICs 0.5-1.0 μg/ml, except Par = 4 μg/ml), indicative of a range of capacities to evade resistance due to m^1A1408 (**Fig. 1** and **Supplementary Table 1**). These differences must arise due to the distinct drug scaffolds, specific substituents presented on each ring, and/or their impact on the ability of a given aminoglycoside to adapt its bound conformation to the presence of the methylated nucleobase of A1408.

The activities of some aminoglycosides based on the kanamycin scaffold are among the most strongly impacted by m^1A1408 modification: kanamycin A (Kan), bekanamycin (Bek) and dibekacin (Dbk) are at least 1000-fold less effective with expression of NpmA (**Fig. 1**). Tob is also strongly impacted by the m^1A1408 modification but retains some activity (reduced 250- to 500-fold) compared to these three drugs. However, in sharp contrast, Amk and arbekacin (Abk), both

of which have a L-HABA group attached to the 2-DOS ring (Ring II), exhibit strong retained activity against the m^1A1408 modification (MICs of 8 μg/ml compared to 0.5 μg/ml in the absence of NpmA; **Fig. 1**).

Aminoglycosides with a gentamicin scaffold, including Gen, micronomicin (Mcr), and G418, exhibit generally greater retained activity. Of these three drugs, G418, which uniquely has a 6'-OH in Ring I, shows the greatest ability to evade the impact of m^1A1408 modification (**Fig. 1**). On the other hand, netilmicin (Net), an analog of sisomicin, which has a conformationally restricted Ring I, has the highest measurable MIC with NpmA expression (>1024 μg/ml; **Fig. 1**), highlighting a potential contribution of Ring I conformational flexibility to evasion of the m^1A1408 resistance modification.

Finally, for the two 4,5-DOS aminoglycosides tested, Neo and Par, distinct sensitivities to the m^1A1408 modification are again observed with a 32-fold difference in the impact of the resistance modification between the two drugs (**Fig. 1**). Neo and Par differ only in their Ring I 6' substituents (NH_3^+ vs OH, respectively) and, consistent with the observation for G418, these results suggest that the identity of the 6' substituent contributes significantly to the observed differences in sensitivity to m^1A1408.

Together, these results highlight the potential impacts of aminoglycoside features including specific ring substituents, polarity, and ring flexibility on drug sensitivity to m^1A1408-mediated aminoglycoside resistance. Additionally, these features encompass elements of aminoglycoside structure both near (*e.g.*, Ring I substituents at the 6' position) and distant from A1408 (*e.g.*, addition of a L-HABA group to Ring II).

Structural basis for Abk and G418 evasion of the m^1A1408 aminoglycoside-resistance modification

To determine the structural basis for the ability of some aminoglycosides to strongly evade m^1A1408-mediated resistance, we determined electron cryomicroscopy (cryo-EM) structures of three *E. coli* 70S ribosome-drug complexes. Ribosome complexes were independently prepared with two aminoglycosides with distinct scaffolds and ring substituents (Abk and G418) that each exhibit retained activity in the presence of the m^1A1408 modification, and used to determine their structures bound to the m^1A1408-modified 70S ribosome (hereafter referred to as "70S (m^1A1408)"; **Supplementary Figs. 1** and **2**, and **Supplementary Table 2**). The structure of the unmodified 70S (A1408)–Abk complex was also determined to enable direct comparison to the corresponding m^1A1408-containing structure (**Supplementary Fig. 3** and **Supplementary Table 2**). Both 70S (m^1A1408)–drug complexes were prepared in the presence of mRNA and cognate tRNAs which are included in the final model, while the 70S (A1408)-Abk complex were empty. The three final high-resolution cryo-EM maps, 70S (A1408)-Abk (2.7 Å), 70S (m^1A1408)-Abk (2.2 Å) and 70S (m^1A1408)–G418 (2.4 Å) (**Fig. 2a-c**), show clear density at h44 corresponding to the bound aminoglycosides, permitting comparison of drug-ribosome interactions in the presence and absence of A1408 methylation (**Supplementary Fig. 4)**.

Comparison of Abk bound to the ribosome with and without the m^1A1408 modification reveals discernible differences in both aminoglycoside and rRNA conformations, and their interactions (**Fig. 2a,b** and **Supplementary Fig. 5a,b**). In the 70S (A1408)-Abk complex, Abk engages with the phosphate backbone of 16S nucleotides A1493 and G1494 and the nucleobases of G1494 and U1495 through its 2-DOS ring (Ring II), while the L-HABA group interacts with C1496 and G1497, and Ring III interacts with G1405 and C1407. The Ring I 6' substituent (NH_3^+) is positioned to hydrogen bond with atom N1 of A1408 (2.6 Å distance) and is 4.9 Å from the phosphate backbone of A1493 (**Supplementary Fig. 5b**). Without any conformational adjustment of the rRNA or Abk, addition of the N1 methyl group to generate m^1A1408 would result in a clash with the Ring I 6'-NH_3^+ (**Fig. 2d,e**). Thus, although many drug-rRNA interactions are retained in the 70S (m^1A1408)-Abk complex structure (**Supplementary**

Table 3), the distance between the Abk Ring I 6'-NH_3^+ and m^1A1408 N1 is increased by 2.7 Å to 5.3 Å due to A1408 methylation. Movements of both the m^1A1408 base (shifted by ~1.5 Å) and adjustment of the Ring I and II glycosidic bond orientation (dihedral angle $\Phi_{I/II}$ rotated by ~19°) are necessary to accommodate the base methylation at A1408 (**Fig. 2f**, and **Supplementary Fig. 5c** and **Supplementary Table 4**). Other changes around A1408 include an increase in the distance between Abk Ring I O3 and N6 of A1408 from 3.6 to 5.4 Å, such that this interaction is disrupted when A1408 is methylated. Unique to the 70S (m^1A1408)-bound Abk, the methyl group of A1408 is oriented towards the O3 atom of Abk located 3.4 Å away, and thus positioned to potentially make a weak C-H···O hydrogen bond (**Supplementary Fig. 5b** and **Supplementary Table 3**). The Abk Ring I pucker also differs between the 70S (A1408)- and 70S (m^1A1408)-bound structures, with puckering phase angles of -21.0° and 60.2°, respectively; this change appears necessary to allow adjustment of the interatomic distance between the Ring I 6'-NH_3^+ and N1 of A1408 (**Fig. 2g** and **Supplementary Table 4**). This change in ring pucker also alters the Ring I ω dihedral angle (O-C-C-6'-N/O, from 26° to 57°), though both remain closest to the *gauche/trans* (*gt*) configuration. Collectively, these changes in the glycosidic dihedral angles between Rings I and II, the ω dihedral angle, and the puckering phase angle of Ring I allow adaptation of Abk binding in the presence of the methyl group on m^1A1408.

Differences in RNA base step and base pair helical parameters and pseudo-torsional angles for base rotation are observed between the ribosome structures with unmethylated and methylated A1408. In the immediate vicinity of the bound Abk and m^1A1408, roll, twist and tilt angle differ for three consecutive base steps of 16S rRNA including C1407~A1408, A1408~C1409 and C1409~A1410, with additional changes in shift and slide for C1407~A1408 and A1408~C1409, respectively (**Supplementary Fig. 5d**). On the opposite strand, except for the unpaired and highly mobile nucleotides A1492 and A1493, no other base step parameters change significantly. Similarly, adjacent to A1408, changes in buckle, propeller twist, and opening angles are observed for base pairs C1407-G1494 and C1409-G1491, and base pair shear is also

altered for C1407-G1494 (**Supplementary Fig. 5e**). Finally, pseudo-dihedral angles η″ and θ″, which measure the twist and bending in the RNA backbone, are most changed for nucleotides close to the modified m^1A1408 base (**Supplementary Fig. 5f**). These analyses reveal that conformational changes in the rRNA occur to accommodate binding of Abk when A1408 is modified, but that these changes are localized around m^1A1408 with no distant, large scale conformational changes being required. Comparison of the two 70S–Abk structures thus highlight the coordinated changes in both the drug conformation and its rRNA binding site that are necessary to maintain interaction and effectively evade resistance conferred by m^1A1408.

Many analogous drug-RNA interactions are also observed in the 70S (m^1A1408)-G418 complex structure (**Fig. 2c,h** and **Supplementary Table 4**). However, as both the 3' and 4' positions of the G418 Ring I are substituted with a hydroxyl group, additional interactions are possible with the phosphate backbone of A1492. Additionally, in contrast to Abk, the 6' position of G418 has both 6'-OH and 7'-CH_3 groups which are positioned 4.0 Å and 3.5 Å from the methyl group of m^1A1408, respectively (**Fig. 2h**). The position of the 6'-OH is adjusted compared to a previously determined crystal structure of G418 bound to a model A-site RNA (PDB code 1MWL), in which it is oriented to hydrogen bond with atom N1 of A1408 (2.7 Å distant), with the 7'-CH_3 located 3.3 Å away from the N1 atom. Despite this reorientation of the G418 6'-OH, it is positioned closer to atom N1 of m^1A1408 compared to the 6'-NH_3^+ of Abk (**Supplementary Fig. 5b** and **Supplementary Table 3**), which suggests the formation of a weak C-H···O hydrogen bond that might favor aminoglycosides like G418 containing a 6'-OH substituent. The G418 Ring I/II glycosidic linkage dihedral angles are intermediate between the values for Abk with A1408 vs. m^1A1408 for $\Phi_{I/II}$, and similar to both values for $\psi_{I/II}$ (**Supplementary Table 4**). The G418 Ring I has a puckering phase angle of -5.7°, which is most similar to Abk bound to 70S (A1408) (**Supplementary Table 4**). These findings indicate that Abk, with its 6'-NH_3^+, must move further from the partially charged m^1A1408 to avoid unfavorable interactions, necessitating a change in ring pucker that is not required for G418, for which smaller changes are necessary to adapt to the

presence of the methyl group. Collectively, these structures reveal key adaptations by specific aminoglycosides and their h44 binding site that allow them to maintain sufficient interaction with the rRNA to evade the impact of m^1A1408-mediated resistance.

Aminoglycoside conformational adaptation facilitates evasion of the m^1A1408 resistance modification

To fully define how evasion of m^1A1408 is achieved, analysis of a larger panel of aminoglycosides is needed, including those that evade resistance very poorly and for which empirical structural studies are therefore not possible. To accomplish this, we turned to molecular dynamics (MD) simulations with both m^1A1408-modified and unmodified A-site rRNA (hereafter referred to as modified and unmodified rRNA) and conducted all-atom MD simulations of a 25-nucleotide A-site rRNA model fragment (nucleotides C1403-U1414 and G1486-U1498) in complex with 12 different aminoglycosides (listed in **Fig. 1** and **Supplementary Table 1**). Starting coordinates for these simulations were taken from crystal structures of model A-site rRNA-aminoglycoside complexes where available or generated by docking based on the closest aminoglycoside structural analog (see **Methods** for details).

A partially restrained approach was used in which rRNA flexibility was limited with a harmonic constant, k = 0.2. This approach was selected based on observations from the structural studies above, wherein the A-site rRNA exhibited smaller conformational changes compared to the larger shifts in aminoglycoside conformation between unmodified and m^1A1408-modified ribosomes. Another consideration was to also avoid potential unrealistic binding scenarios that might arise from fully unrestrained simulation of the model rRNA in isolation. Each aminoglycoside was simulated bound to both modified and unmodified rRNAs in three 100 ns replicates, each following a 10 ns equilibration period, resulting in a total simulation period of 300 ns per aminoglycoside-rRNA complex. All simulations were assessed to ensure convergence of potential

energy of the complex, temperature, pressure and root mean square deviation (RMSD) of the aminoglycosides during the equilibration and production runs. To compare the rRNA-bound and free conformations of aminoglycosides, 100 ns MD simulations were also conducted for each aminoglycoside in its unbound state. To gain additional insight into free aminoglycoside flexibility, conformational scanning with the Optimized Potentials for Liquid Simulations 4 (OPLS4) force field was used to scan glycosidic and ω dihedral angles and thereby identify their energy landscape regions corresponding to favorable (low energy) and unfavorable (high energy) conformations.

We first analyzed the Ring I/II dihedral angles ($\Phi_{I/II}$ and $\Psi_{I/II}$), and Ring I ω angle as these were observed to change in our structures for drugs able to evade the modification (Abk and G418; **Fig. 2**). $\Phi_{I/II}$ and $\Psi_{I/II}$ are continuously sampled in the simulations and do not show distinct clustering for all eleven aminoglycosides tested (**Fig. 3a,b**). In contrast, two distinct conformational clusters are observed for ω for aminoglycosides bound to modified rRNA (**Fig. 3c**). Conformational scanning of ω in free aminoglycosides (Kan, Bek, Tob and Dbk) reveals three energy minima corresponding to the *gt* (30 to 90°), *trans*/*gauche* (*tg*; 150 to 180° and -180 to -150°) and *gauche*/*gauche* (*gg*; -30 to -90°) conformations, with *gt* and *tg* being the most and least favorable, respectively (**Supplementary Fig. 6a**). In the simulations of rRNA-bound aminoglycosides, the most favorable *gt* conformation is exclusively observed with unmodified rRNA, while distinct clusters of *gt* and *tg* conformations are predominantly observed when bound to modified rRNA (**Fig. 3c**). However, the adoption of each ω conformation when bound to modified rRNA depends upon distinct changes in $\Phi_{I/II}$ and $\Psi_{I/II}$ compared to the corresponding complexes with unmodified rRNA. We therefore refer to these distinct conformational states as "*gt* adaptation" and "*tg* adaptation," respectively, reflecting the distinct structural adjustments required to accommodate the modified rRNA. In the *gt* adaptation, ω is maintained in the favorable *gt* conformation and changes in $\Phi_{I/II}$ and $\Psi_{I/II}$ are primarily responsible for necessary movement of the Ring I 6' substituent (NH_3^+ or OH) away from the methyl group of m^1A1408 to minimize

clashes. In contrast, in the *tg* adaptation, the major reorientation of ω is primarily responsible for moving the Ring I 6' group away from m^1A1408.

Comparison of *gt*/*tg* conformation populations when bound to modified rRNA reveals that the 4,6-DOS gentamicin scaffold aminoglycosides Mcr and G418, and the 4,5-DOS Par exhibit a higher prevalence of the energetically favorable *gt* adaptation compared to their close analogs Gen and Neo, respectively (**Fig. 3d** and **Supplementary Table 1**). These aminoglycosides also show smaller increases in MIC upon m^1A1408 modification suggesting that retained ability to bind modified rRNA in the *gt* conformation correlates with more effective evasion of the resistance modification (**Fig. 1**). Notably, unlike all the other aminoglycosides examined which possess a 6'-NH_3^+ group, Mcr, G418 and Par have either a 6'-OH (G418 and Par) or N-methylamine (6'-NH_2CH_3; Mcr) group. The predominance of the *gt* adaptation thus appears to be driven by electronic stabilization at the interface between Ring I and m^1A1408 (discussed further in the following section).

While the extent of *tg* adaptation appears to be a component of m^1A1408 evasion, this feature alone cannot explain all the observed differences in MIC changes between unmodified and modified ribosomes. For example, Kan exhibits a greater extent of *gt* adaptation (35%) compared to Bek (8%) (**Fig. 3d**), despite differing only in their Ring I 2' substituent, but still exhibits among the highest MICs with m^1A1408 modification (**Fig. 1**). Further, the activities of Amk and Abk are least impacted by the resistance modification, but these aminoglycosides do not exhibit a particularly high population of the *gt* adaptation when bound to the modified rRNA. Amk and Abk differ from two of the poorest evaders of the m^1A1408 modification, Kan and Dbk, respectively, by only the addition of a L-HABA group to Ring II. These observations suggest that additional factors beyond the polarity at the Ring I 6' position, such as the identity of other Ring I substituents or addition of the Ring II L-HABA moiety also play a crucial role in determining the overall capacity for a given aminoglycoside to evade the m^1A1408 resistance modification.

Role of the Ring I 6′ substituent on adaptation to the modified A site

To further explore how the polarity of the Ring I 6' substituent affects aminoglycoside conformation when bound to m^1A1408 modified rRNA, we compared the simulated conformations of three aminoglycosides of the gentamicin scaffold, Gen (6'-NH_3^+), Mcr (6'-$NH_2^+CH_3$) and G418 (6'-OH and 7'-CH_3), as well as the 4,5-DOS aminoglycosides Par (6'-OH) and Neo (6'-NH_3^+).

When bound to modified rRNA, the Gen Ring I is found in two populations corresponding to the *gt* (20%) and *tg* (80%) adaptations (**Fig. 3d**). As noted previously, these conformations require distinct shifts in $\Phi_{I/II}/\Psi_{I/II}$ compared to the favored *gt* conformation that is observed when bound to unmodified rRNA, and these shifts affect the positioning of the charged 6'-NH_3^+ group relative to the N1 of A1408. In the *gt* adaptation, rotations around $\Phi_{I/II}/\Psi_{I/II}$ (11.1° and 5.1°, respectively) position the Gen 6'-NH_3^+ ~5 Å from the N1 of A1408, placing the methyl group of m^1A1408 at a distance of ~3.5 Å, which is an energetically unfavorable arrangement (**Fig. 4a**). In contrast, the *tg* adaptation involves smaller $\Phi_{I/II}/\Psi_{I/II}$ shifts (6 and 2.6°, respectively; **Fig. 4b**) but positions the 6'-NH_3^+ ~6 Å from N1 of A1408 due to the additional rotation around ω, placing the methyl group of m^1A1408 at a distance of ~5.2 Å. This difference also results in an overall average 6'-NH_3^+-A1408 N1 interatomic distance of ~6 Å when bound to the modified rRNA, as *tg* is the predominant conformation (**Fig. 4c**). As such, Gen can avoid making highly unfavorable interactions or clashes with the modification by predominantly adopting a less favorable *tg* conformation, which is necessitated by the presence of the NH_3^+ group.

In contrast to Gen, Mcr has a 6' secondary amine with an additional 7'-methyl group and predominantly (~81%) binds to modified rRNA in the *gt* conformation (**Fig. 3c,d** and **Supplementary Table 5**). Small rotations around $\Phi_{I/II}/\Psi_{I/II}$ (both 3°) result in an average interatomic distance of ~5 Å between the 6'-NH_2^+ and N1 of A1408 and place the methyl group of m^1A1408 at a distance of ~3.8 Å in the modified rRNA (**Fig. 4c,d**). The 7'-methyl group of Mcr and the methyl group of m^1A1408 are also ~4.6 Å, placing them at a distance that can support favorable van der Waals interactions, likely stabilizing this interaction and making the *gt*

adaptation more favorable in this context. The third gentamicin scaffold aminoglycoside, G418, binds to the modified rRNA almost exclusively in the more favorable *gt* conformation (~99%) attained through rotations about $\Phi_{I/II}/\Psi_{I/II}$ of 1.5 and 9.1°, respectively, compared to its conformation when bound to unmodified rRNA (**Fig. 3d** and **4e**). Similar to Mcr, the interatomic distance between the 6'-OH and N1 of A1408 is ~5 Å, placing the 7'-methyl group of m^1A1408 at a distance of ~4.2 Å to allow more favorable interactions, including a weak C-H···O hydrogen bond between the 6'-OH and the methyl group of m^1A1408 (**Fig. 4e**). Given that they have identical Ring II and III structures, these differences in Ring I 6' substituent positioning, and the resultant interactions with the methyl group of m^1A1408, must give rise to the observed differences in MIC change (Gen > Mcr > G418) between bacteria with unmodified and modified rRNA.

Similar comparisons of the 6' substituents of Ring I are possible with Par and Neo which have 6'-OH and 6'-NH_3^+ groups, respectively, but otherwise identical Ring I substituents. Neo primarily adopts a *tg* adaptation (~81%), with additional small adjustments in $\Phi_{I/II}/\Psi_{I/II}$ (2.1 and 4.1°, respectively), resulting in a larger interatomic distance (>6 Å) between the 6'-NH_3^+ and N1 of A1408 (**Fig. 4c,f**). In contrast, Par binds the modified rRNA exclusively in the more favorable *gt* conformation with only small adjustments of $\Phi_{I/II}/\Psi_{I/II}$ (2.3 and 1.2°, respectively) and maintaining an interatomic distance of ~5 Å between the 6'-OH and N1 of A1408 (**Fig. 4c,g** and **Supplementary Table 5**). Again, the impact of m^1A1408 on activity (change in MIC: Neo > Par) must result from the relatively unfavorable versus favorable interactions made by the 6'-NH_3^+ or 6'-OH substituent, respectively. Collectively, these findings highlight the important role of the 6' position in determining Ring I conformational preferences when binding to the m^1A1408 and reveal that a 6'-OH facilitates better adaptation to the methylated target site and thus evasion of the resistance conferred by the modification.

Influence of other Ring I substituents on adaptation to the m^1A1408 modified A site

The four kanamycin scaffold aminoglycosides without a Ring II L-HABA group–Kan, Bek, Tob, and Dbk–share a common Ring I 6'-NH_3^+ substituent (**Supplementary Fig. 6b**) but are otherwise distinct in terms of the number and polarity of their other Ring I substituents (**Fig. 1**), allowing us to explore the role of these substituents in resistance evasion. Kan and Bek exhibit a similarly low ability to evade the effect of m^1A1408 modification, with both exhibiting among the largest changes in MIC with NpmA expression (**Fig. 1**). The population of conformations corresponding to the *gt* adaptation in Kan (35%) and Bek (8%) differs, with shifts in $\Phi_{I/II}$ and $\Psi_{I/II}$ of 5.8°/9.2° for Kan compared to 11.5°/1.1° for Bek (**Fig. 5a** and **Supplementary Table 5**). These shifts position Ring I 6'-NH_3^+ ~5 Å from the N1 of A1408 in both Kan and Bek (**Fig. 5a,e**). The more prevalent *tg* adaptation, Kan (50%) and Bek (80%), require larger shifts in $\Phi_{I/II}$ and $\Psi_{I/II}$ of 11°/3.6° in Kan compared to 8.8°/0.6° in Bek, but similarly position the Ring I 6'-NH_3^+ group ~6.2 Å from A1408 for both aminoglycosides (**Fig 5b-e**). However, despite the apparent greater capacity of Kan to adopt the *gt* adaptation and its greater flexibility around $\Psi_{I/II}$, it nonetheless fails to evade the resistance conferred by m^1A1408 with a change in MIC identical to Bek.

To assess the availability of conformations of Kan and Bek that can bind to the ribosomal A site, we performed 100 ns MD simulations of the free states of these aminoglycosides. The $\Psi_{I/II}$ angle range for aminoglycosides is categorized into *syn*-Ψ (-30° to -90°) and *anti*-Ψ (150° to 180° and -150° to -180°). S*yn*-Ψ corresponds to the ribosomal A site-bound conformation, whereas the *anti*-Ψ conformation is incompatible with binding to the A site[22]. Kan exhibits two distinct clusters corresponding to *syn*-Ψ and *anti*-Ψ conformation angle ranges while, in contrast, Bek is exclusively observed in the *syn*-Ψ conformation (**Supplementary Fig. 6c**). In the *syn*-Ψ conformation, the Kan 2'-OH and 5-OH of Ring II interact favorably (**Fig. 5f**), while in Bek a hydrogen bond forms between the 2'-NH_3^+ and 5-OH of Ring II (**Fig. 5g**). In the *anti*-Ψ conformation, the Kan 2'-OH interacts favorably with a different Ring II substituent, 3-NH_3^+ (**Fig. 5h**), whereas in Bek the *anti*-Ψ conformation results in electrostatic repulsion between 2'-NH_3^+ and 3-NH_3^+, making this conformation disallowed (**Fig. 5i**). We further observed that Tob and Dbk

also exclusively adopt a *syn*-Ψ conformation due to their 2'-NH_3^+. These results are also consistent with previous MD simulations using NMR-derived time-averaged restraints of the Ring I/II disaccharide fragment of a more limited set of aminoglycosides and for a shorter time (5 ns) which showed adoption of both *syn*-Ψ and *anti*-Ψ for Kan but only *syn*-Ψ for Tob[22]. Thus, the sensitivity of Kan to m^1A1408 than expected may be explained by its greater propensity to adopt a conformation (*anti*-Ψ) that is incompatible with binding to the A site binding without first converting to the *syn*-Ψ conformation. Such conversion of the "inactive" drug fraction in the free state may be less readily accomplished in the context of the less favorable interaction with the m^1A1408-modified A site.

Tob, Dbk and Bek exhibit a range of MIC changes upon m^1A1408 modification in the order Bek > Dbk > Tob (**Fig. 1** and **Supplementary Table 1**). As these aminoglycosides have a common 2'-NH_3^+ and differ only in the presence or absence of 3'-OH/4'-OH, they offer an opportunity to assess the impact of these additional Ring I substituents on adaptation to m^1A1408. We first compared the *tg* adaptations of Bek (3'-OH and 4'-OH), Tob (4'-OH only), and Dbk (no OH at either site) which are accomplished through $\Phi_{I/II}/\Psi_{I/II}$ changes of ~9°/1°, ~17°/5° and ~6°/1°, respectively (**Fig. 5c,d,j,k** and **Supplementary Table 5**). The largest shifts are observed for Tob, allowing its 4'-OH group to reorient and interact with the phosphate backbone of A1492 (**Fig. 5j**). This new favorable interaction likely contributes significantly to its greatest ability among this group to evade the impact of the modification. In contrast, while Bek appears to exhibit a greater ability to change in $\Phi_{I/II}$ as compared to Dbk (i.e. Bek > Dbk), the order of activity in the presence of m^1A1408 is reversed (Dbk > Bek). However, from analysis of the dihedral energy landscape of these three free aminoglycosides, Dbk appears to have the greatest flexibility around $\Phi_{I/II}/\Psi_{I/II}$ (**Supplementary Fig. 6e**), consistent with the absence of the both bulky Ring I 3'-OH and 4'-OH substituents. Thus, inherent flexibility around the Ring I dihedrals alone does not determine resistance evasion.

We next used RMSD-based clustering to select representative frames from the simulations of Bek, Tob, or Dbk bound to m^1A1408-modified rRNA for calculation of ligand strain energy using molecular mechanics-generalized Born surface area (MM-GBSA). This analysis revealed ligand strain energy in the order Bek > Tob > Dbk (**Supplementary Table 6**), where higher strain energy in the bound state indicates a greater energetic cost of adaptation between the free and rRNA-bound states. Thus, the smaller change in $\Phi_{I/II}$ for Dbk results in lower strain (5.9 kcal/mol) compared to Bek which experiences the highest strain of the three aminoglycosides (13.0 kcal/mol). Tob, which exhibits the largest $\Phi_{I/II}$ shift and additional change in $\Psi_{I/II}$, exhibits an intermediate strain (9.4 kcal/mol), and thus appears to achieve an optimal balance between minimizing steric hindrance and maintain a favorable interaction via its 4'-OH. These trends are also reflected in the small change in average rRNA-aminoglycoside hydrogen bond count calculated over the full 300 ns simulation for Tob (8.8 in unmodified rRNA vs. 8.5 in modified rRNA) compared to the more significant decreases for Dbk (7.9 to 6.4 hydrogen bonds) and Bek (9.7 to 8.7 hydrogen bond), which indicate a loss of interaction energy that negatively impacts adaptability (**Supplementary Table 7**). Thus, while the absence of both 3'- and 4'-OH substituents results in lower ligand strain energy, Dbk lacks the ability to form interactions needed to adjust its glycosidic dihedral angles and engage with the rRNA phosphate backbone. Bek, despite having 3'- and 4'-OH groups, encounters high ligand strain energy and steric hindrances, making its interactions with the phosphate backbone unfavorable. In contrast, Tob, with only the 4'-OH substituent, exhibits greater flexibility to engage the phosphate backbone without incurring high strain energy, making it more adaptable to the modified rRNA.

Finally, when comparing MICs against modified rRNA, the sisomicin-scaffold aminoglycoside Net exhibits a significantly higher value (>1024 μg/mL) compared to Dbk and Gen (**Fig. 1** and **Supplementary Fig. 7a**). These three aminoglycosides have identical Ring I substituents, but Net differs in the presence of a carbon-carbon double bond in its Ring I. Our MD simulations reveal that after the 10 ns system equilibration, Net dissociates from the modified

rRNA, likely due to unfavorable interactions, as indicated by the higher RMSD of the rRNA-aminoglycoside complex (**Supplementary Fig. 7a,b**). In contrast, all other aminoglycosides remain bound throughout the 100 ns simulations. Conformational scans of the $\Phi_{I/II}/\Psi_{I/II}$ and ω of free Net and Gen reveal similar energetic landscapes and thus do not provide any insight the basis for differences in MIC or behavior in the simulation (**Supplementary Fig. 7c-e**). However, a severe restriction in Net Ring I pucker flexibility, resulting from the unsaturated bond, was confirmed through a conformational scan of Ring I dihedral angles θ3 and θ4, showing limited pucker flexibility close to -60º and 60º in Net compared to Gen (**Supplementary Fig. 7f,g**). This restriction can explain the inability of Net to adapt to the modified RNA and highlights the additional crucial role of Ring I pucker in aminoglycoside adaptability, as observed in our structures of the 70S-Abk complexes.

Impact of Ring II L-HABA on aminoglycoside-rRNA interaction and resistance evasion

Amk and Abk have a kanamycin scaffold but are distinguished by the addition of an L-HABA group at their Ring II N1 position (**Fig. 6a**). Analysis of representative structures from RMSD-based clustering of these MD simulations reveals that the L-HABA group consistently maintains stable interactions with the rRNA, regardless of the methylation status at A1408. The L-HABA group forms three direct hydrogen bonds with G1497, C1496, and U1495, thereby strengthening the A-site rRNA-drug interaction. The polar nature of the L-HABA group may also enhance the ability of Amk and Abk to engage in additional water-mediated interactions with the rRNA, unlike Kan and Dbk, which lack this group but are otherwise structurally identical. In the MD simulations, Amk and Abk maintain an average of 12.5 and 9.7 direct hydrogen bonds, respectively, with unmodified rRNA compared to 10.9 and 7.5 with modified rRNA (**Supplementary Table 7**). The overall greater number of direct hydrogen bonds, and the potential water mediated interactions of L-

HABA with the A-site rRNA, likely play a key role in the improved adaptability of Amk and Abk, allowing them to better overcome m^1A1408-mediated resistance by enhancing binding to the modified rRNA.

Amk and Abk can both adopt either the *gt* or *tg* adaptation when binding to modified rRNA, with the latter more prevalent. The differences in dihedral shifts and the populations of *gt* adaptations for aminoglycoside analogs with and without L-HABA, e.g. Amk (21%) compared to Kan (35%) and Abk (10%) compared to Dbk (3%), demonstrate that the presence of the L-HABA also influences *gt* adaptation (**Fig. 6b**). When bound to modified rRNA in either their *gt* or *tg* adaptation, Amk and Abk maintain a similar binding pose as observed with unmodified rRNA in the *gt* conformation, evidenced by the unchanged interatomic distances between these aminoglycosides and Ring II during the simulations (**Fig. 6c**). Amk adopts the *gt* adaptation more frequently (21%) than Abk (10%) and smaller changes in the Amk Ring I dihedrals are required, particularly in $\Psi_{I/II}$, with $\Phi_{I/II}/\Psi_{I/II}$ changing by 8.9°/1.1° and 8.0°/5.4°, respectively, compared to their binding to unmodified rRNA (**Fig. 6d,e** and **Supplementary Table 5**). The differences in the 2'-OH/-NH_3^+ groups also contribute to Amk's greater adaptability in the *gt* conformation compared to Abk, similar to what was noted above for Kan and Bek **(Supplementary Table 5**). In contrast, the *tg* adaptation requires shifts in $\Phi_{I/II}/\Psi_{I/II}$ 0.9°/2.2° and 7.2°/0.6° for Amk and Abk, respectively (**Fig. 6f,g**). These observations suggest that larger glycosidic dihedral changes are required in the *gt* adaptation to keep the 6'-NH_3^+ (present in both Amk and Abk) and N1 of m^1A1408 at a distance of ~5 Å, while for the *tg* adaptation a smaller shift is sufficient to more favorably position the two charges ~6 Å apart (**Fig. 6b,d-g**).

Collectively, these results reveal that the L-HABA group plays a crucial role in anchoring Amk and Abk to the rRNA by forming additional hydrogen bonds, which remain unaffected by the methylation of A1408. As such, these interactions substantially overcome penalties incurred due to other less favorable but necessary ring reorganizations or interactions with the modified base.

Role of aminoglycoside inherent flexibility on adaptation to modified RNA

Gen and Dbk have identical Ring I and II structures but differ in Ring III which influences the observed shifts in $\Psi_{I/II}$ upon binding to modified rRNA (**Supplementary Table 5**) and results in greater *gt* adaptation for Gen (19%) compared to Dbk (3%) (**Fig. 3d**). Additionally, G418 exhibited a larger $\Psi_{I/II}$ shift (9.1°) upon binding to modified rRNA compared to Gen (5.2°) and Mcr (3.3°) in the *gt* adaptation, despite sharing the same scaffold (**Fig. 4a,d,e**).

To understand the extent and impact of differences in aminoglycoside inherent flexibility around the Ring III/II dihedrals ($\Phi_{III/II}$) that may arise from variations in Ring III, we calculated the mean and standard deviation (SD) of aminoglycoside glycosidic dihedral angles in their free state (**Supplementary Fig.8a** and **Supplementary Table 8**). Here, the dihedral angle SD from MD simulations serve as a proxy for flexibility at ring connections, with higher SD indicating greater flexibility. While $\Phi_{III/II}$ is comparatively rigid across all aminoglycosides, $\Psi_{III/II}$ exhibits substantial flexibility (**Supplementary Fig.8a** and **Supplementary Table 8**). We next calculated the dihedral angles of aminoglycosides when bound to unmodified and m^1A1408-modified rRNA and calculated the shifts in mean dihedral angles, revealing that aminoglycosides with a gentamicin scaffold exhibit greater shifts in $\Phi_{III/II}$ compared to those with a kanamycin scaffold (**Supplementary Fig.8b,c** and **Supplementary Tables 8** and **9**). This difference can likely be attributed to the absence of the 5'' substituent in Ring III of the gentamicin scaffold, which enhances flexibility at this dihedral position. Notably, this increase in flexibility was most pronounced in G418 (**Supplementary Fig.8a**). Next, analyzing the Ring I/II dihedrals, we found that the flexibility of $\Phi_{I/II}$, was similar across the aminoglycosides, but $\Psi_{I/II}$ showed higher flexibility in Kan, Amk and G418 due to the presence of 2'-OH in Kan and Amk and 6'-OH in G418, further aiding in their adaptability.

4,6-DOS aminoglycosides fail to adapt to m^7G1405 modified rRNA

In the absence of modification at G1405, Ring III of the 4,6-DOS aminoglycosides forms extensive hydrogen bonds with nucleotides C1407 (N6), G1405 (O6 and N7), and C1404 (O6). In contrast, 4,5-DOS aminoglycosides, with their distinct Ring III orientation, do not interact directly with G1405. Consistent with these previous structural observations, MIC analyses show that the activity of 4,5-DOS aminoglycosides is unaffected by m^7G1405 methylation whereas no 4,6-DOS aminoglycoside retains any significant activity (**Supplementary Table 1**). Using Bek, G418, and Abk as representative examples that reflect the range of abilities to evade the m^1A1408-mediated resistance based on their distinct ring structures (**Fig. 1**), we first modeled the aminoglycoside-bound A-site rRNA with the m^7G1405 modification. Maintaining fixed rRNA atoms and minimizing aminoglycoside conformations, we found that these hydrogen bonds are all disrupted (shown for Abk in **Fig. 7a**).

We next conducted 100 ns MD simulations to explore why these aminoglycosides (Bek, G418, Abk) fail to effectively adapt their conformations in response to m^7G1405. These MD simulations reveal the loss of these three hydrogen bonds, along with an increased interatomic distance to ~6 Å between Ring III (N3") and the N7 atom of m^7G1405, hindering effective binding and resulting in significant displacement of Abk, Bek and G418 from the binding pocket (**Fig. 7b**). Additionally, comparisons of changes in $\Phi_{III/II}$ and $\Psi_{III/II}$ from unmodified to m^7G1405-modified rRNA show that unfavorable larger shifts are necessary in the more rigid $\Phi_{III/II}$ dihedral (**Fig. 7c** and **Supplementary Table 10**).

Next, to observe binding and unbinding events on a timescale in which ligands can remain trapped in energetically unfavorable states due to insufficient sampling in classical MD simulations, we applied replica exchange with solute tempering (REST) MD to rRNA complexes with these three aminoglycosides. REST MD enhances sampling by allowing replicas at different effective temperatures to exchange conformations, and thus the potential to observe unbinding within the 100 ns simulation timescale[23]. These simulations were conducted with Bek, Abk, and G418, bound to unmodified, m^1A1408-modified and m^7G1405-modified rRNA. In the m^1A1408-

modified rRNA complex, Bek exhibits unbinding events during the simulation consistent with observations from the classical MD simulations, while in the presence of m^7G1405, both Bek and Abk display similar unbinding behaviors (**Fig. 7d**). Further, while G418 does not exhibit a fully unbound state (**Fig. 7d**), substantial movement within the binding site is observed over the course of the simulation including partial displacement of Ring III (**Fig. 7d**). Consistent with maintained stable binding throughout the REST MD, lower RMSD values are observed for rRNA-aminoglycoside complexes with unmodified rRNA compared to those with modified rRNA (**Fig. 7e**). The RMSD values for complexes with m^1A1408-modified rRNA also accurately reflect the ability of each aminoglycoside to adapt to the modification: Abk exhibits the least variation in RMSD, indicating greater stability, while Bek showed the most variation, suggesting reduced stability with m^1A1408 (**Fig. 7e**). In contrast, simulations with m^7G1405-modified rRNA show large RMSD fluctuations, indicating greater conformational changes in the aminoglycosides and instability of the complex (**Fig. 7e**). This observation is further supported by interatomic distance measurements, including Ring I (6')-A1408 (N1), Ring II (N3)-A1492 (OP2), Ring II (N1)-U1495 (O4), and Ring III (N3")-G1405 (N7) (**Fig. 7f**; denoted as distances D1 to D4, respectively). All these distances show increased fluctuations and shifts in the mean in complexes with m^7G1405-modified rRNA, further illustrating the absence of an energetically-plausible conformation for effective adaptation and thus explaining their failure to evade m^7G1405.

Discussion

Aminoglycosides have been crucial as last-resort antibiotics, particularly in treating serious MDR infections[2,7]. Resistance mechanisms, including AMEs, efflux pumps, and the methylation of rRNA residues A1408 and G1405 lead to pan-aminoglycoside resistance and are increasingly associated with MDR superbugs[17,18]. Newer aminoglycosides like Plz can circumvent resistance from AMEs but remain vulnerable to rRNA methylation[14,15,24,25]. However, while the effects of one of these resistance methylations (m^1A1408) was previously observed to be at least partly

aminoglycoside-specific[13], how ring substituents and inter-ring flexibility contribute to the greater ability of some drugs to evade the impact of methylation at A1408 remained unclear until the present work.

Using a diverse panel of aminoglycosides, we confirmed that the m^1A1408 modification leads to varied changes in *E. coli* susceptibility, with some drugs largely evading its effects. In contrast, the m^7G1405 modification causes pan-resistance to 4,6-DOS aminoglycosides while 4,5-DOS aminoglycosides remain unaffected as they do not interact with G1405. This observation also indicates that there are no significant structural or allosteric alterations of aminoglycoside binding arising from m^7G1405 modification. Additionally, the high resistance conferred by m^7G1405 to 4,6-DOS aminoglycosides suggests that these drugs' ability to bind to the 50S ribosomal subunit (in addition to binding to the 30S subunit)[26] lacks bactericidal effect.

Our cryo-EM structures revealed that Abk and G418 binding to m^1A1408-methylated 70S ribosomes induces localized 16S rRNA conformational changes, with methylation having no effect on nucleotides further than two nucleotides from A1408. Abk adapts by significantly altering its Ring I/Ring II glycosidic dihedral angle to avoid the methyl group at A1408. Our results build on recent findings that a preorganized binding conformation is key to the effectiveness of bridged macrobicyclic antibiotics like cresomycin[27]. When cresomycin binds to methylated ribosomes, the dimethylated nucleobase A2503 (m^2m^8A2503) shifts minimally (0.6 Å compared to its position in the ribosome unmodified at this site), while cresomycin adapts to the modification by undergoing a 14° dihedral angle change. This structural adjustment highlights a common adaptive strategy employed by antibiotics to overcome the challenges posed by methylated rRNA. While prior MD studies have assessed the conformational flexibility of aminoglycosides in their free state, including Neo, Kan, Amk and Tob[22,28], our studies additionally explored how these dynamics influence their adaptation to methylated RNA, revealing critical insights into resistance evasion.

Interestingly, while our simulations suggest that aminoglycosides containing a Ring I 6'-NH_3^+ group can adapt to m^1A1408 by orienting this substituent in either the *gt* or *tg* configuration, we observe only *gt* adaptation via cryo-EM. It is possible that the addition of mRNA and tRNAs to these complexes, which was necessary to observe Abk and G418 bound to the 16S rRNA in

modified rRNA, subtly altered the h44 aminoglycoside binding site such that the *gt* adaptation was preferred. We emphasize, however, that our cryo-EM data demonstrate aminoglycoside conformations which permit evasion of m^1A1408 empirically, while our MD simulations additionally permit exploration of drug conformations which may be shorter lived or less energetically favorable and hence less likely to be observed in 3D reconstructions from cryo-EM.

The present work provides insight into the roles of specific aminoglycoside features in m^1A1408 resistance evasion, as well as the corresponding failure of any 4,6-DOS aminoglycoside to evade the resistance conferred by m^7G1405. These key insights include:

1. Aminoglycosides containing a 6'-OH group (G418 and Par) or a 6'-secondary amine with a terminal methyl group (Mcr) show a smaller change in MIC between unmodified and modified rRNA. MD simulations revealed that these aminoglycosides bind more frequently to the modified A site in the *gt* conformation, with the proximity (~5 Å) between the Ring I 6'-position and N1 of A1408 indicating energetic favorability.
2. A 2'-OH group on Ring I (Kan) promotes adoption of a Ring I/Ring II *anti*-Ψ conformation in the free state, which is incompatible with binding to the A site binding and thus results in a fraction of the drug being "inactive" without conversion to *syn*-Ψ.
3. The absence in Dbk of Ring I 3'- and 4'-OH groups reduces ligand strain energy upon 16S rRNA binding but limits crucial interactions with the rRNA phosphate backbone, resulting in fewer hydrogen bonds. In contrast, the presence in Bek of both 3'- and 4'-OH substituents leads to increased strain and steric hindrance, making interactions less favorable. The presence of only a 4'-OH achieves a balance of greater flexibility for engaging the backbone without high strain energy, resulting in the enhanced evasion of m^1A1408 observed for Tob.
4. Addition of an L-HABA group to Ring II anchors Amk and Abk to the rRNA with three hydrogen bonds that are unaffected by m^1A1408 methylation, allowing significantly better resistance evasion compared to their non-L-HABA-containing analogs Kan and Dbk, respectively.
5. The loss of the Ring III 5'' substituent in the gentamicin scaffold increases flexibility at the Ring III/Ring II glycosidic torsion that aids in adaptation to m^1A1408-methylated rRNA in the A site.

6. In the m^7G1405-methylated A site, 4,6-DOS aminoglycosides require larger, unfavorable changes in the $\Phi_{III/II}$ and $\Psi_{III/II}$ torsions, increasing ligand strain and leading to the loss of three crucial hydrogen bonds, which hinders effective adaptation to the A site.

These determinants, which can explain the observed differences in MIC between unmodified and m^1A1408- or m^7G1405-modified rRNA, could be leveraged for structure-guided aminoglycoside design. By using smaller rRNA-aminoglycoside complexes for computational screening and optimization, this framework can also aid in understanding other resistance mechanisms or toxicity arising from aminoglycosides binding to eukaryotic ribosomes . This approach could thus accelerate the discovery of new aminoglycosides with lower toxicity and improved resistance evasion, providing valuable antibiotics for treating Gram-negative and mycobacterial infections. Overall, this work provides a structural and computational framework for understanding adaptations to modified binding sites, such as rRNA methylation that can be broadly applied to other antibiotics, accounting for the dynamics of both the free antibiotic and its complex with the binding site, shaped by substituents and structural features. This framework can thus elucidate antibiotic resistance mechanisms and serve as a computational tool for structure-activity relationship studies in future antibiotic design.

Methods

Antibiotic minimum inhibitory concentration (MIC) measurements

Fresh cation-adjusted Mueller–Hinton (CA-MHB) medium (5 ml) containing 100 μg/ml ampicillin was inoculated (1:100 dilution) with saturated overnight culture of *E. coli* BL21(DE3) harboring plasmid encoding NpmA (pET-*npmA*), RmtB (pET-*rmtB*), or empty pET-44 control. All cultures were grown to ~0.1 A_{600} at 37 °C with vigorous shaking. Cells from 1 ml of culture were collected by centrifugation, washed with phosphate buffered saline solution (2× 0.5 ml), and resuspended CA-MHB medium to 0.1 A_{600} (5×10^7 cfu/ml). Following 50× further dilution with CA-MHB, 100 μl of diluted culture (1×10^5 cfu/well) was used to inoculate an equal volume of CA-MHB medium,

pre-dispensed on a 96-well plate, containing 10 μM isopropyl β-d-thiogalactopyranoside and a range of antibiotic concentrations. For cells with pET- *npmA* or pET-*rmtB*, an antibiotic concentration range of 2–1024 μg/ml was tested, except for Abk with pET–*npmA* for which 0.06-32 μg/ml was used. For empty pET-44 control, a range of 0.06–32 μg/ml was tested. MIC measurements were made in technical duplicates using two independent bacterial transformations for each plasmid/ drug combination. Wells with no antibiotic or no cells served as additional controls for each set of replicates. The plates were incubated at 37 °C with shaking and A_{600} measurements taken after 24 hours. The MIC was defined as the lowest concentration of antibiotic that inhibited growth, i.e., A_{600} of <0.05 above background.

MD Simulations

Model preparation and restraints–A 25 nucleotide A-site RNA model system (nts G1486-U1498 and C1403-U1414), with A1492 and A1493 in a "flipped out" configuration, was used for all simulations of aminoglycoside-rRNA complexes. RNA-bound aminoglycoside conformations were taken from experimental structures where available: with an A-site model rRNA for Kan (PDB code 2ESI), Tob (PDB code 1LC4), Amk (PDB 4P20), Gen (PDB code 2ET3), Par (PDB code 1J7T and Neo (PDB code 2ET4). In absence of an experimental structure additional aminoglycosides were modeled based on their closest analog: Dbk using Tob (PDB code 1LC4), Mcr using Gen (PDB code 2ET3), and Net using the sisomicin-A-site model RNA complex (PDB code 4F8V).

All system preparation and molecular dynamics (MD) simulations were carried out using the Desmond module of the Schrödinger software suite with the OPLS4 force field[29]. For methylated A-site rRNA fragments (m^1A1408 or m^7G1405), the methyl group was added, and a positive charge was assigned to the relevant nitrogen atom (N1 or N7, respectively). Additionally, aminoglycosides were protonated in all simulations. Structure preparation, including the addition

of hydrogens, bond order assignment, energy minimization, and hydrogen bond optimization, was performed in Schrödinger. The rRNA-aminoglycoside complex was solvated using TIP3P water molecules with a NaCl concentration of 100 mM. Similarly, free aminoglycoside simulations were solvated with a final salt concentration of 100 mM NaCl.

To explore the impact of methylation on A1408 dynamics in relation to aminoglycosides, we employed a restrained fragment approach. Simulations of the unmethylated RNA-Kan complex were first run for 100 ns with the RNA constrained using harmonic constants (k) of 0, 0.1, 0.2, or 0.5 kcal/mol/Å^2, while the aminoglycoside remained fully unrestrained in all cases. Without RNA restraints (k = 0), RMSD and residue room mean square fluctuation (RMSF) exceeded 10 Å, indicating unrealistic dynamics. The lowest (k = 0.1) and highest restraint (k = 0.5) resulted in high and low RMSD and RMSF, respectively, with the particularly low values around nucleotides known to be more dynamic (A1492, A1493, and A1408) in the latter case suggesting this system also did not accurately reflect the system dynamics. A harmonic constant of k = 0.2 was therefore empirically selected for all subsequent simulations, as the optimal balance of limiting unrealistic RNA flexibility while also capturing relevant dynamics of the rRNA-drug complexes.

MD simulation production run and trajectory analysis–After minimization, each system was heated to 310.5 K and equilibrated in the isobaric–isothermal (NPT) ensemble (P = 1 atm, T = 310.5 K) for 10 ns. Production simulations (100 ns) were then conducted in the NPT ensemble using the final configuration from the equilibration phase. The Langevin thermostat and barostat were employed with relaxation times of 1 ps and 2 ps, respectively. The equations of motion were integrated with multiple time steps: 2 fs for short-range interactions and 6 fs for long-range interactions, applying a 9-Å cutoff for nonbonded interactions. Coordinates were saved every 100 ps. Each simulation was performed in triplicate for a cumulative time of 300 ns. Post-simulation analyses included calculations of RMSD, RMSF, potential energy of the rRNA-aminoglycoside complex, interaction counts, and measurements of aminoglycoside dihedral angles and distances

between atoms of aminoglycosides and RNA. The quality of the simulations was evaluated using the Desmond simulation quality analysis module. The convergence of potential energy was confirmed, showing low standard deviations. Additionally, the temperature remained stable throughout the simulations, and the RMSD of the ligand stayed within 2 Å, indicating reliable system stability and simulation quality.

REST simulations–REST simulations were conducted in Desmond over a total simulation time of 100 ns across 8 parallel replicas, with temperatures ranging from 300 to 410 K. RNA atoms were restrained with a harmonic constant of k = 0.2 kcal/mol/Å^2, as before. Periodic exchanges of configurations between replicas were performed to enhance sampling efficiency. Exchange acceptance ratios ranged from 15% to 20%, with convergence assessed by monitoring potential energy. The simulations otherwise followed the standard Desmond protocol using the OPLS4 force field and trajectories were analyzed to examine dihedral angle changes and conformational adjustments within the RNA-aminoglycoside complex.

Dihedral angle potential energy scans–To assess the dihedral angle potential energy of different aminoglycosides, comparative energy calculations were performed using the Conformational Scan module in the Schrödinger suite. These calculations were carried out in implicit water with the OPLS4 force field. A conformational scan was conducted by sampling dihedral angles at 10° intervals, capturing a wide range of potential conformations for each aminoglycoside. The potential energy of aminoglycoside dihedral angles was calculated using 500 iterations of steepest descent minimization at each sampled angle. This iterative process ensured that the system converged to a stable local minimum for each conformation. A comparative energy approach was employed, allowing us to evaluate and compare the relative energies of different aminoglycosides, rather than focusing on absolute energy values.

MM-GBSA–Molecular Mechanics Generalized Born Surface Area (MM-GBSA) was performed on a representative structure from the top cluster of each MD simulation replicate, selected based on the aminoglycoside RMSD. Schrödinger's Prime MM-GBSA module was used, with

minimization applied only to polar hydrogens to maintain the conformations of both RNA and aminoglycosides during the calculations. Strain energy was calculated from the Prime MM-GBSA results, following previously established procedures[30,31].

Ribosome purification and 70S complex assembly

Expression of NpmA from pET-*npmA* was used to obtain modified *E. coli* 70S (m^1A1408) ribosomes. 70S ribosomes, with and without NpmA modification were purified identically, as previously described[32,33]. 70S (A1408) ribosome-Abk complex was prepared by incubating purified *E. coli* 70S ribosomes (0.5 μM) with Abk (0.5 mM) in Buffer 2 (10 mM HEPES/KOH pH 7.6, 10 mM $MgCl_2$ 1 M NH_4Cl and 6 mM 2-mercaptoethanol) at 37 °C for 40 minutes. Following incubation, 70S complexes were briefly placed on ice until used to prepare grids for cryo-EM. Aminoglycoside complexes with NpmA-modified ribosomes were assembled by incubating purified 70S (m^1A1408) (0.75 μM) with *in vitro* transcribed mRNA (2.5 μM; P- and A-site sequence: AUG GUA) and aminoglycoside (1 mM; Abk or G418) at 37 °C for 20 minutes. Purified *E. coli* $tRNA^{fMet}$ and $tRNA^{Val}$ (2.5 μM) were added and the final complex incubated at 37 °C for an additional 20 minutes before briefly placing on ice until used to prepare grids for cryo-EM.

Cryo-EM structure determination

Specimen preparation–To prepare samples for cryo-EM, C-Flat™ holey carbon gold grids (R1.2/1.3, 300 mesh) were glow discharged in a PELCO easiGlow™ glow discharger (Ted Pella) for 15 seconds. Grids were prepared in a Vitrobot Mark IV (FEI) at 4 °C and 100% humidity. 70S complex (3 μL) was applied to the grid and allowed to stand for 15 seconds before blotting for 4 seconds (for the 70S (A1408)-Abk complex) or 3.5 seconds (for both 70S (m^1A1408) complexes) and plunging into liquid ethane to vitrify. Prepared grids were stored under liquid nitrogen until performing quality screens and data collection.

Cryo-EM data collection–Cryo-EM data were collected for 70S (A1408)-Abk (17,071 micrographs), 70S (m^1A1408)-Abk (5,053 micrographs) and 70S (m^1A1408)-G418 (5,302 micrographs) at the National Center for CryoEM Access and Training (NCCAT) using a Krios G3i (Thermo Fisher Scientific) cryo-transmission electron microscope operating at 300 kV. Movies for the 70S (A1408)-Abk complex were recorded with a total electron dose of 52 $e^-/Å^2$ and magnification of 81,000x (pixel size of 1.069 Å/px) using a Gatan K3 direct electron detector. Movies for the 70S (m^1A1408)-Abk and 70S (m^1A1408)-G418 complexes were recorded with a total electron dose of 50 $e^-/Å^2$ and magnification of 96,000x (pixel size of 0.814 Å/px) using a Thermo Fisher Scientific Falcon 4i direct electron detector.

Image Processing–Prior to processing cryo-EM data, movie frames were aligned using motion correction in RELION-3.1[34], and contrast transfer function (CTF) parameters were estimated for the motion-corrected micrographs using GCTF[35]. Micrographs displaying poorer than 3 Å (70S (A1408)-Abk) or 6 Å (both 70S (m^1A1408) datasets) estimated maximum resolution were discarded. Following pre-processing, an initial round of automated particle picking was performed on a random subset of 50 micrographs using the reference-free Laplacian-of-Gaussian autopicker in RELION. Particles were extracted and downsampled by a factor of 4, then subjected to a round of reference-free two-dimensional classification in RELION-3.1 to generate 2D reference images, which were then used to perform reference-based automated particle picking on the random micrograph subsets. Picked particles were extracted, 2D-classified, and manually curated to remove junk particles and particles picked on carbon, then used to train a Topaz particle picking model[36] which was used to pick particles from all retained micrographs in each dataset. Identified particles were extracted from micrographs with 4× downsampling and subjected to 2D classification. Non-ribosome-like 2D classes were discarded.

Following identification of ribosome-like particles, initial 3D reconstructions were generated for each dataset in RELION-3.1 using the stochastic gradient descent method[37]. Initial reconstructions were checked to ensure correct handedness before performing three-dimensional

classification with particle alignment to identify 70S ribosome particles. Particles in non-70S classes (including junk classes and 50S ribosomal subunits) were discarded. Following 3D classification, particles were re-extracted without binning and initial 3D refinements were performed against 70S 3D class average maps to determine optimized particle coordinates and 3D orientations. 70S (m^1A1408) datasets were then subjected to focused 3D classification using masks generated from the A-, P-, and E-site tRNA chains of PDB code 5JTE[38]. Classes containing A- and P-site tRNAs were combined for further processing. Datasets were then subjected to iterative CTF refinement[34], Bayesian particle polishing[39], and 3D refinement steps to improve map quality. Finally, 70S (A1408) particles were 3D-classified without alignment and without a mask to resolve differences in 30S head domain position before performing final 3D refinement on particles with unratcheted 30S subunits and unswiveled 30S head domains.

Post-processing and Map Sharpening–Following final 3D refinement, maps were postprocessed in RELION-3.1 using solvent masks generated from 10 Å low-pass filtered 3D refinement consensus maps. No sharpening B factor was applied during postprocessing. Local resolution was estimated using the local resolution estimation tool in RELION-3.1. Masked, unsharpened maps from RELION-3.1 were sharpened in PHENIX using the Autosharpen tool[40] before use in molecular modeling.

Molecular modeling–PDB code 5JTE[38] and the $tRNA^{fMet}$ and ribosomal protein L31 chains of PDB code 7K00[41] were used as starting models. Initial coordinates and geometric restraints for Abk and G418 were generated using PHENIX eLBOW[42]. Models were rigidly fit into the final 3D refinement maps in UCSF ChimeraX [43] before performing real-space refinement in PHENIX. Local real-space refinement of models was performed as necessary in COOT[44]. Final validation of cryo-EM maps and models was performed in PHENIX using MolProbity[45].

Summaries of the complete cryo-EM workflow for each complex as well as all data collection, processing and final model statistics are provided in **Supplementary Fig. 1-4** and

Supplementary Table 2. Atomic coordinates and maps were deposited in the Protein Data Bank (PDB) and Electron Microscopy Database (EMDB), respectively (**Supplementary Table 2**).

Acknowledgements

This work was supported by NIH/ NIAID award R01-AI 088025 (to CMD and GLC) and NIH/ NIGMS award T32-GM135060 (to JMM). Some of this work was performed at the NCCAT and the Simons Electron Microscopy Center located at the New York Structural Biology Center, supported by the NIH Common Fund Transformative High Resolution Cryo-Electron Microscopy program (U24 GM129539,) and by grants from the Simons Foundation (SF349247) and NY State Assembly.

Author contributions

Author contributions: D.D., J.M.M., C.M.D., and G.L.C. designed research; D.D., J.M.M., and N.Z. performed research; D.D., J.M.M. analyzed data; and D.D., J.M.M., C.M.D., and G.L.C. wrote the paper. D.D. and J.M. contributed equally as co-first authors. C.M.D. and G.L.C. are co-corresponding authors.

Competing interests

The authors declare no competing interest.

References

1 Becker, B. & Cooper, M. A. Aminoglycoside antibiotics in the 21st century. *ACS Chem Biol* **8**, 105-115, doi:10.1021/cb3005116 (2013).
2 Krause, K. M., Serio, A. W., Kane, T. R. & Connolly, L. E. Aminoglycosides: An Overview. *Cold Spring Harb Perspect Med* **6**, doi:10.1101/cshperspect.a027029 (2016).
3 Safi, K. H., Damiani, J. M., Sturza, J. & Nasr, S. Z. Extended-Interval Aminoglycoside Use in Cystic Fibrosis Exacerbation in Children and Young Adults: A Prospective Quality Improvement Project. *Glob Pediatr Health* **3**, 2333794X16635464, doi:10.1177/2333794X16635464 (2016).
4 Ratjen, F., Brockhaus, F. & Angyalosi, G. Aminoglycoside therapy against Pseudomonas aeruginosa in cystic fibrosis: a review. *J Cyst Fibros* **8**, 361-369, doi:10.1016/j.jcf.2009.08.004 (2009).
5 Jiang, M., Karasawa, T. & Steyger, P. S. Aminoglycoside-Induced Cochleotoxicity: A Review. *Front Cell Neurosci* **11**, 308, doi:10.3389/fncel.2017.00308 (2017).
6 Jospe-Kaufman, M., Siomin, L. & Fridman, M. The relationship between the structure and toxicity of aminoglycoside antibiotics. *Bioorg Med Chem Lett* **30**, 127218, doi:10.1016/j.bmcl.2020.127218 (2020).
7 Serio, A. W., Keepers, T., Andrews, L. & Krause, K. M. Aminoglycoside Revival: Review of a Historically Important Class of Antimicrobials Undergoing Rejuvenation. *EcoSal Plus* **8**, doi:10.1128/ecosalplus.ESP-0002-2018 (2018).
8 Doi, Y. & Arakawa, Y. 16S ribosomal RNA methylation: emerging resistance mechanism against aminoglycosides. *Clin Infect Dis* **45**, 88-94, doi:10.1086/518605 (2007).
9 Ramirez, M. S. & Tolmasky, M. E. Aminoglycoside modifying enzymes. *Drug Resist Updat* **13**, 151-171, doi:10.1016/j.drup.2010.08.003 (2010).
10 Wachino, J. I., Doi, Y. & Arakawa, Y. Aminoglycoside Resistance: Updates with a Focus on Acquired 16S Ribosomal RNA Methyltransferases. *Infect Dis Clin North Am* **34**, 887-902, doi:10.1016/j.idc.2020.06.002 (2020).
11 Seupt, A., Schniederjans, M., Tomasch, J. & Haussler, S. Expression of the MexXY Aminoglycoside Efflux Pump and Presence of an Aminoglycoside-Modifying Enzyme in Clinical Pseudomonas aeruginosa Isolates Are Highly Correlated. *Antimicrob Agents Chemother* **65**, doi:10.1128/AAC.01166-20 (2020).
12 Nosrati, M. *et al.* Functionally critical residues in the aminoglycoside resistance-associated methyltransferase RmtC play distinct roles in 30S substrate recognition. *J Biol Chem* **294**, 17642-17653, doi:10.1074/jbc.RA119.011181 (2019).
13 Wachino, J. *et al.* Novel plasmid-mediated 16S rRNA m1A1408 methyltransferase, NpmA, found in a clinically isolated Escherichia coli strain resistant to structurally diverse aminoglycosides. *Antimicrob Agents Chemother* **51**, 4401-4409, doi:10.1128/aac.00926-07 (2007).
14 Clark, J. A. & Burgess, D. S. Plazomicin: a new aminoglycoside in the fight against antimicrobial resistance. *Ther Adv Infect Dis* **7**, 2049936120952604, doi:10.1177/2049936120952604 (2020).
15 Gur, D. *et al.* Comparative in vitro activity of plazomicin and older aminoglyosides against Enterobacterales isolates; prevalence of aminoglycoside modifying enzymes and 16S rRNA methyltransferases. *Diagn Microbiol Infect Dis* **97**, 115092, doi:10.1016/j.diagmicrobio.2020.115092 (2020).
16 Dunkle, J. A. *et al.* Molecular recognition and modification of the 30S ribosome by the aminoglycoside-resistance methyltransferase NpmA. *Proc Natl Acad Sci U S A* **111**, 6275-6280, doi:10.1073/pnas.1402789111 (2014).

17 Rahman, M. *et al.* RmtC and RmtF 16S rRNA Methyltransferase in NDM-1-Producing Pseudomonas aeruginosa. *Emerg Infect Dis* **21**, 2059-2062, doi:10.3201/eid2111.150271 (2015).
18 Gamal, D. *et al.* Carbapenem-resistant Klebsiella pneumoniae isolates from Egypt containing blaNDM-1 on IncR plasmids and its association with rmtF. *Int J Infect Dis* **43**, 17-20, doi:10.1016/j.ijid.2015.12.003 (2016).
19 Savic, M., Lovric, J., Tomic, T. I., Vasiljevic, B. & Conn, G. L. Determination of the target nucleosides for members of two families of 16S rRNA methyltransferases that confer resistance to partially overlapping groups of aminoglycoside antibiotics. *Nucleic Acids Res* **37**, 5420-5431, doi:10.1093/nar/gkp575 (2009).
20 Kawai, A., Suzuki, M., Tsukamoto, K., Minato, Y. & Doi, Y. Functional and Structural Characterization of Acquired 16S rRNA Methyltransferase NpmB1 Conferring Pan-Aminoglycoside Resistance. *Antimicrob Agents Chemother* **65**, e0100921, doi:10.1128/AAC.01009-21 (2021).
21 Kanazawa, H., Baba, F., Koganei, M. & Kondo, J. A structural basis for the antibiotic resistance conferred by an N1-methylation of A1408 in 16S rRNA. *Nucleic Acids Res* **45**, 12529-12535, doi:10.1093/nar/gkx882 (2017).
22 Corzana, F. *et al.* The pattern of distribution of amino groups modulates the structure and dynamics of natural aminoglycosides: implications for RNA recognition. *J Am Chem Soc* **129**, 2849-2865, doi:10.1021/ja066348x (2007).
23 Chyzy, P., Kulik, M., Re, S., Sugita, Y. & Trylska, J. Mutations of N1 Riboswitch Affect its Dynamics and Recognition by Neomycin Through Conformational Selection. *Front Mol Biosci* **8**, 633130, doi:10.3389/fmolb.2021.633130 (2021).
24 Blanchard, L. S. *et al.* Multicenter Clinical Evaluation of ETEST Plazomicin (PLZ) for Susceptibility Testing of Enterobacterales. *J Clin Microbiol* **60**, e0183121, doi:10.1128/JCM.01831-21 (2022).
25 Castanheira, M. *et al.* In Vitro Activity of Plazomicin against Gram-Negative and Gram-Positive Isolates Collected from U.S. Hospitals and Comparative Activities of Aminoglycosides against Carbapenem-Resistant Enterobacteriaceae and Isolates Carrying Carbapenemase Genes. *Antimicrob Agents Chemother* **62**, doi:10.1128/AAC.00313-18 (2018).
26 Seely, S. M. *et al.* Molecular basis of the pleiotropic effects by the antibiotic amikacin on the ribosome. *Nat Commun* **14**, 4666, doi:10.1038/s41467-023-40416-5 (2023).
27 Wu, K. J. Y. *et al.* An antibiotic preorganized for ribosomal binding overcomes antimicrobial resistance. *Science* **383**, 721-726, doi:10.1126/science.adk8013 (2024).
28 Asensio, J. L. *et al.* Experimental evidence for the existence of non-exo-anomeric conformations in branched oligosaccharides: NMR analysis of the structure and dynamics of aminoglycosides of the neomycin family. *Chemistry* **8**, 5228-5240, doi:10.1002/1521-3765(20021115)8:22<5228::AID-CHEM5228>3.0.CO;2-L (2002).
29 Lu, C. *et al.* OPLS4: Improving Force Field Accuracy on Challenging Regimes of Chemical Space. *J Chem Theory Comput* **17**, 4291-4300, doi:10.1021/acs.jctc.1c00302 (2021).
30 Dey, D., Ramakumar, S. & Conn, G. L. Targeted Redesign of Suramin Analogs for Novel Antimicrobial Lead Development. *J Chem Inf Model* **61**, 4442-4454, doi:10.1021/acs.jcim.1c00578 (2021).
31 Kavanaugh, L. G., Mahoney, A. R., Dey, D., Wuest, W. M. & Conn, G. L. Di-berberine conjugates as chemical probes of Pseudomonas aeruginosa MexXY-OprM efflux function and inhibition. *npj Antimicrobials and Resistance* **1**, 12, doi:10.1038/s44259-023-00013-4 (2023).
32 Hong, S. *et al.* Mechanism of tRNA-mediated +1 ribosomal frameshifting. *Proc Natl Acad Sci U S A* **115**, 11226-11231, doi:10.1073/pnas.1809319115 (2018).

33 Nguyen, H. A., Hoffer, E. D. & Dunham, C. M. Importance of a tRNA anticodon loop modification and a conserved, noncanonical anticodon stem pairing in tRNACGGProfor decoding. *J Biol Chem* **294**, 5281-5291, doi:10.1074/jbc.RA119.007410 (2019).
34 Zivanov, J. *et al.* New tools for automated high-resolution cryo-EM structure determination in RELION-3. *Elife* **7**, doi:10.7554/eLife.42166 (2018).
35 Zhang, K. Gctf: Real-time CTF determination and correction. *J Struct Biol* **193**, 1-12, doi:10.1016/j.jsb.2015.11.003 (2016).
36 Bepler, T. *et al.* Positive-unlabeled convolutional neural networks for particle picking in cryo-electron micrographs. *Nat Methods* **16**, 1153-1160, doi:10.1038/s41592-019-0575-8 (2019).
37 Punjani, A., Rubinstein, J. L., Fleet, D. J. & Brubaker, M. A. cryoSPARC: algorithms for rapid unsupervised cryo-EM structure determination. *Nat Methods* **14**, 290-296, doi:10.1038/nmeth.4169 (2017).
38 Arenz, S. *et al.* A combined cryo-EM and molecular dynamics approach reveals the mechanism of ErmBL-mediated translation arrest. *Nat Commun* **7**, 12026, doi:10.1038/ncomms12026 (2016).
39 Zivanov, J., Nakane, T. & Scheres, S. H. W. Estimation of high-order aberrations and anisotropic magnification from cryo-EM data sets in RELION-3.1. *IUCrJ* **7**, 253-267, doi:10.1107/S2052252520000081 (2020).
40 Liebschner, D. *et al.* Macromolecular structure determination using X-rays, neutrons and electrons: recent developments in Phenix. *Acta Crystallogr D Struct Biol* **75**, 861-877, doi:10.1107/S2059798319011471 (2019).
41 Watson, Z. L. *et al.* Structure of the bacterial ribosome at 2 Å resolution. *Elife* **9**, doi:10.7554/eLife.60482 (2020).
42 Moriarty, N. W., Grosse-Kunstleve, R. W. & Adams, P. D. electronic Ligand Builder and Optimization Workbench (eLBOW): a tool for ligand coordinate and restraint generation. *Acta Crystallogr D Biol Crystallogr* **65**, 1074-1080, doi:10.1107/S0907444909029436 (2009).
43 Goddard, T. D. *et al.* UCSF ChimeraX: Meeting modern challenges in visualization and analysis. *Protein Sci* **27**, 14-25, doi:10.1002/pro.3235 (2018).
44 Emsley, P. & Cowtan, K. Coot: model-building tools for molecular graphics. *Acta Crystallogr D Biol Crystallogr* **60**, 2126-2132, doi:10.1107/S0907444904019158 (2004).
45 Williams, C. J. *et al.* MolProbity: More and better reference data for improved all-atom structure validation. *Protein Sci* **27**, 293-315, doi:10.1002/pro.3330 (2018).

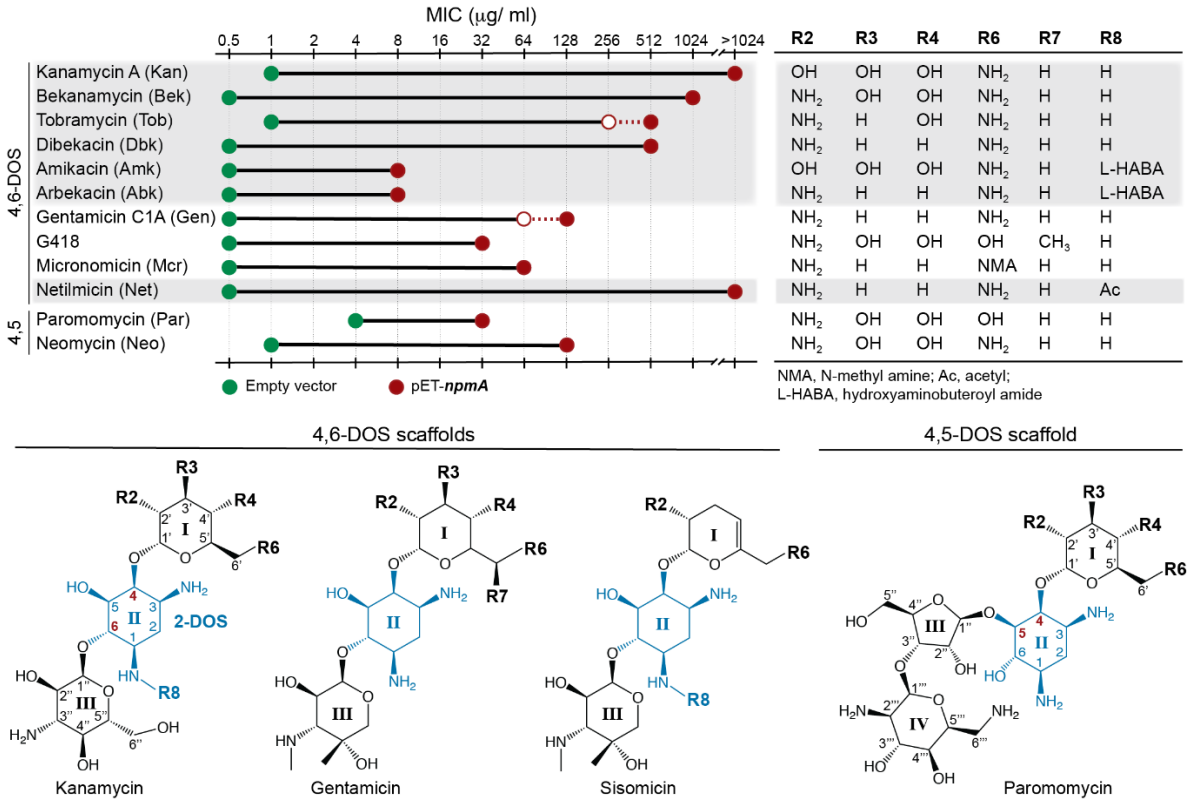

Fig. 1 | MICs of diverse aminoglycosides against *E. coli* with and without m^{1}A1408 modification. Structurally and chemically diverse aminoglycosides, including both 4,6- and 4,5-DOS drugs, were tested for their activity against *E. coli* without (green filled circles) and with (red filled and open circles) expression of NpmA, corresponding to the absence and presence of the m^{1}A1408 aminoglycoside-resistance modification, respectively. Where present, pairs of open and filled circles denote a range for the final consensus MIC determined from the replicate measurements. The kanamycin, gentamicin, sisomicin, and paromomycin chemical scaffolds are shown (*below*), with the individual substituents (R groups) in Rings I and II detailed in the accompanying panel (*right*).

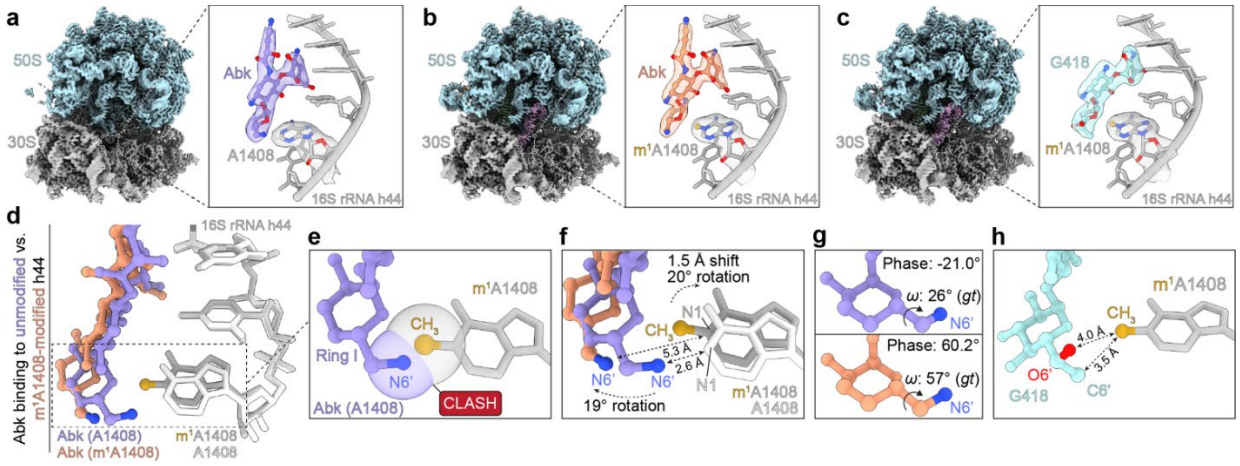

Fig. 2 | Structural basis for m^{1}A1408 modification-based resistance evasion. a, Cryo-EM map of the unmodified *E. coli* 70S ribosome-Abk complex (map threshold: 4.0; map value range -10.8 – 28.7) and a zoomed view (box) of Abk bound at the A site with map segments indicating positions of Abk and 16S nucleotide A1408 (map threshold 5.7). **b**, Cryo-EM map of the m^{1}A1408-modified *E. coli* 70S ribosome-Abk complex (map threshold: 4.0; map value range -7.71 – 29.1) and a zoomed view (box) of Abk bound at the A site with map segments indicating positions of Abk and m^{1}A1408 (map threshold 5.1). **c**, Cryo-EM map of the m^{1}A1408-modified *E. coli* 70S ribosome-G418 complex (map threshold: 4.0; map value range -7.98 – 28.5) and a zoomed view (box) of G418 bound at the A site with map segments indicating positions of G418 and m^{1}A1408 (map threshold 5.1). **d**, Superposition of the A-site rRNA nucleotides 1404-1409, comparing the unmodified (white) and m^{1}A1408-modified (gray) structures, showing conformational changes in Abk and m^{1}A1408. **e**, The 6'-NH_3^+ of Abk would clash with the m^{1}A1408 if it did not undergo a conformational change. **f**, The glycosidic dihedral angles ($\Phi_{I/II}$) shift by 19° with a concurrent shift in the RNA conformation, moving m^{1}A1408 1.5 Å away with a 20˚ rotation. **g**, Comparison of Abk Ring I puckering when bound to the unmodified and m^{1}A1408-modified A site revealing changes in phase angle (-21° to 60°) and 6'-NH_3^+ ω angle (26° to 57°). **h**, G418 favorably positions its 6'-OH and CH_3 groups, 4.0 Å and 3.5 Å, respectively, from the methyl group of m^{1}A1408.

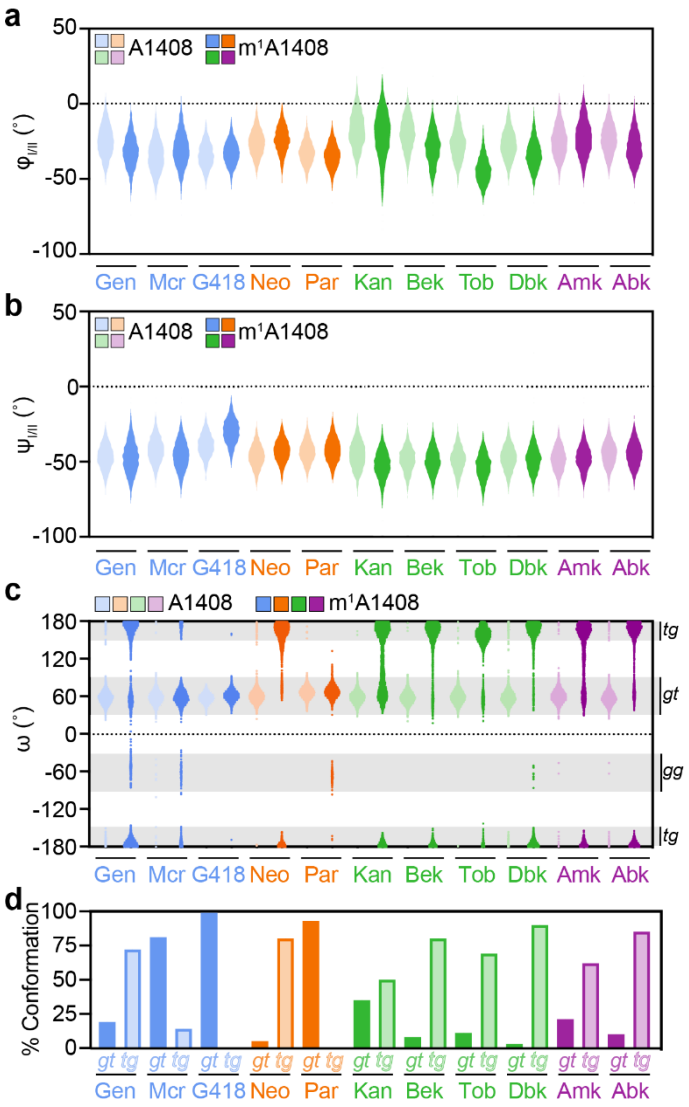

Fig. 3 | Aminoglycoside conformational adaptation facilitates evasion of the m^{1}A1408 resistance modification. a, $\Phi_{I/II}$ and **b**, $\Psi_{I/II}$ dihedral angle distributions from MD simulations (300 ns) of aminoglycosides bound to unmodified and m^{1}A1408-modified rRNA, indicating no distinct clustering. Aminoglycosides are colored by scaffold: gentamicin (blue), 4,5-DOS (orange), kanamycin (green), and kanamycin with L-HABA (purple). Lighter and darker shades represent binding to unmodified and m^{1}A1408-modified rRNA, respectively. **c**, ω dihedral angle distribution, highlighting preferential clustering in the *gt*, *gg*, and *tg* conformations (ranges shaded in gray). **d**, Upon aminoglycoside binding to m^{1}A1408-modified rRNA, the population of conformations based

on *ω* dihedral angle shows adaptations in the *gt* (light shades) and *tg* (dark shades) conformations.

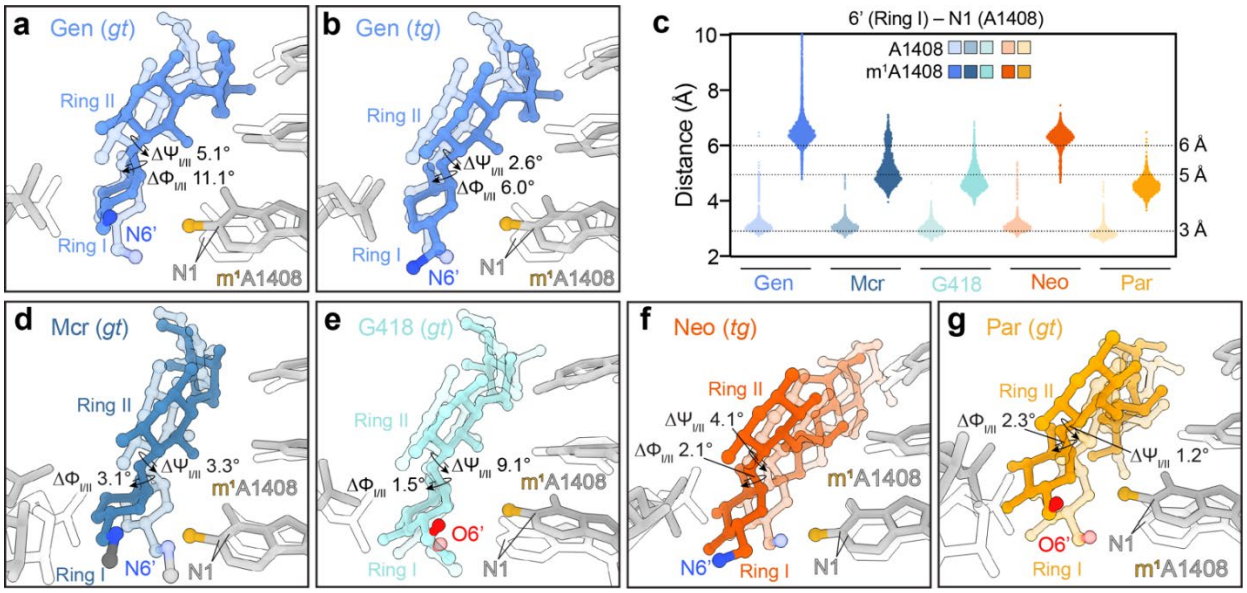

Fig. 4 | Role of the Ring I 6′ substituent in adaptation to the modified A site. a, Superposition of models of simulated Gen binding to m^{1}A1408-modified (opaque drug, gray RNA) or unmodified (semi-transparent drug, white RNA) 16S rRNA in the *gt* conformation. The $\Phi_{I/II}$ and $\Psi_{I/II}$ dihedral angles are shifted (Δ) in the presence of m^{1}A1408 compared to the unmodified base. **b**, Superposition of models of simulated Gen binding to m^{1}A1408-modified or unmodified 16S rRNA in the *tg* conformation. **c**, Distribution of interatomic distances between the aminoglycoside 6' substituent and N1 of A1408, showing greater distances are necessary for accommodation of m^{1}A1408 by 6'-NH_3^+ (Gen and Neo) compared to 6'-OH (Mcr, G418 and Par). Structural superposition of simulated A site-bound **d**, Mcr (*gt* adaptation), **e**, G418 (*gt* adaptation), **f**, Neo (*tg* adaptation) and **g**, Par (*tg* adaptation), with and without A1408 methylation.

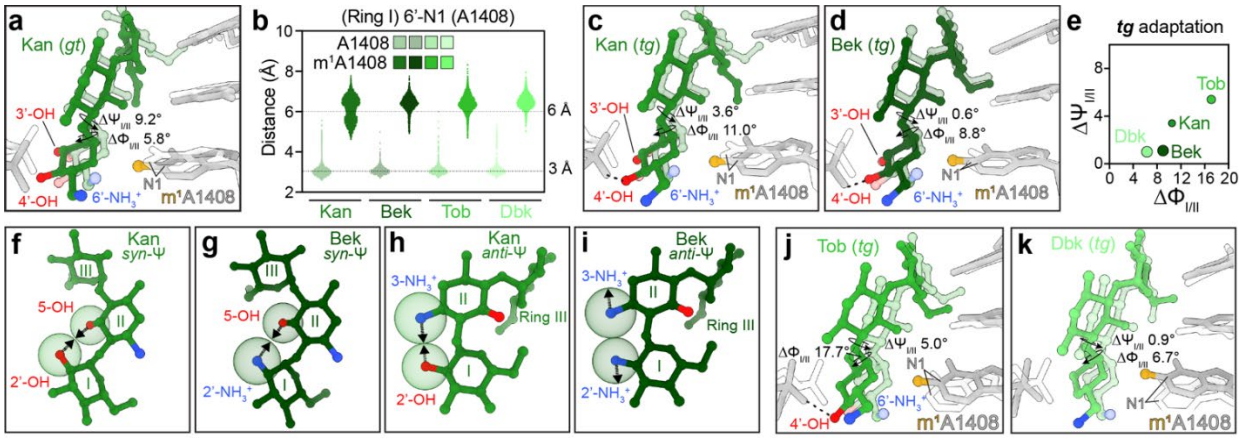

Fig. 5 | Influence of other Ring I substituents on adaptation to the m^{1}A1408-modified A site. **a**, Superposition of models of simulated Kan binding to m^{1}A1408-modified (opaque drug, gray RNA) or unmodified (semi-transparent drug, white RNA) 16S rRNA in the *gt* conformation. The $\Phi_{I/II}$ and $\Psi_{I/II}$ dihedral angles are shifted (Δ) in the presence of m^{1}A1408 compared to the unmodified base. **b**, Distribution of inter-atomic distances between the 6'-NH_3^+ of the kanamycin scaffold aminoglycosides and atom N1 of A1408 (with and without methylation), showing larger average distances compared to 6'-OH containing aminoglycosides (G418, Mcr, and Par; **Fig. 4c**), and suggesting unfavorable interactions with m^{1}A1408. Superposition of simulated A site-bound **c**, Kan and **d**, Bek in the *tg* adaptation. **e**, Summary of shifts in $\Phi_{I/II}$ and $\Psi_{I/II}$ upon *tg* adaptation to m^{1}A1408 for Kan, Bek, Tob and Dbk. **f,g**, *Syn*-Ψ and **h, i**, a*nti*-Ψ conformations of Kan and Bek, respectively. In the s*yn*-Ψ conformation, Ring I and Ring II substituents of both Kan and Bek are positioned in a sterically and electrostatically favorable configuration. In contrast, in the *anti*-Ψ conformation, the repositioned Kan substituent interaction is favorable but unfavorable for Bek, resulting in a mixture of free drug configurations only for Kan. Structural superposition of simulated A site-bound **j**, Tob and **k**, Dbk in the *tg* adaptation.

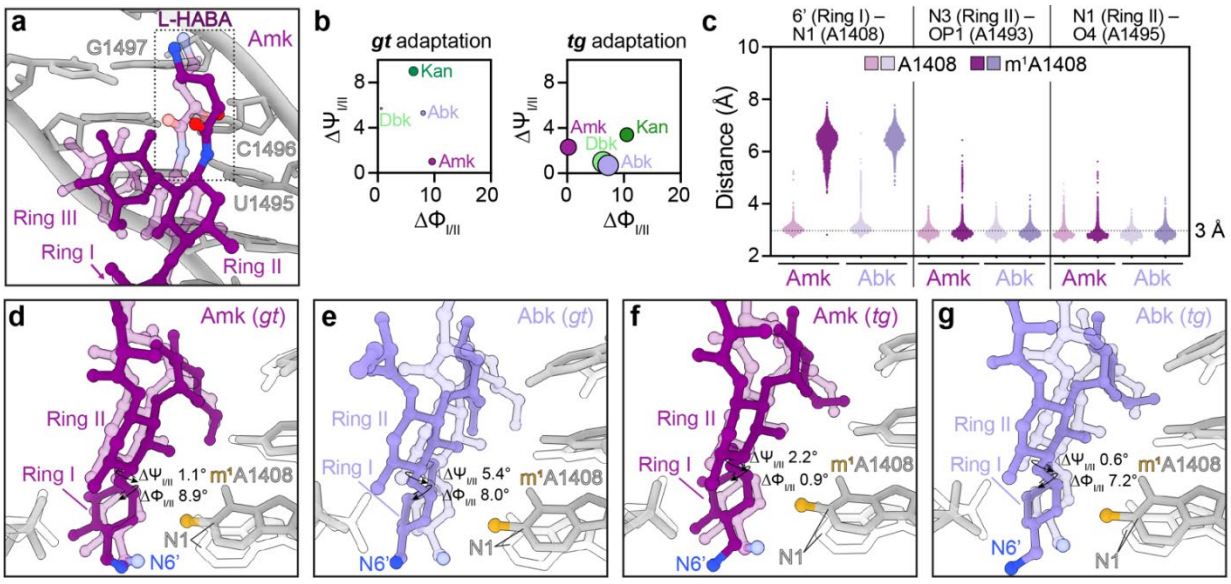

Fig. 6 | Impact of L-HABA on aminoglycoside-rRNA interaction. a, Attachment of the L-HABA group to the 2-DOS ring (Ring II) establishes additional hydrogen bonds with the 16S rRNA distal to A1408, strengthening the interaction with the A site (shown for Abk). The L-HABA conformation remains stable, with the modification at A1408 not affecting its ability to interact with the RNA (opaque drug: m^1A1408; semi-transparent drug: unmodified A1408). **b**, Differences in $\Phi_{I/II}$ and $\Psi_{I/II}$ upon *gt* and *tg* adaptations for Amk and Abk compared to corresponding kanamycin scaffold aminoglycosides lacking an L-HABA group (Kan and Dbk, respectively). **c**, Distribution of interatomic distances between the Ring I 6'-NH_3^+ and N1 of A1408, and two rRNA contacts made by Ring II. For both Amk and Abk, changes in the 6'-NH_3^+ to N1 distance are similar to other kanamycin scaffold aminoglycosides (**Fig. 5b**), which move away >6 Å due to the unfavorable 6' substituent. In contrast, the Ring II interactions are essentially unchanged upon m^1A1408 modification. Structural superposition of simulated A site-bound **d**, Amk and **e**, Abk in the *gt* conformation and **f**, Amk and **g**, Abk in the *tg* conformation.

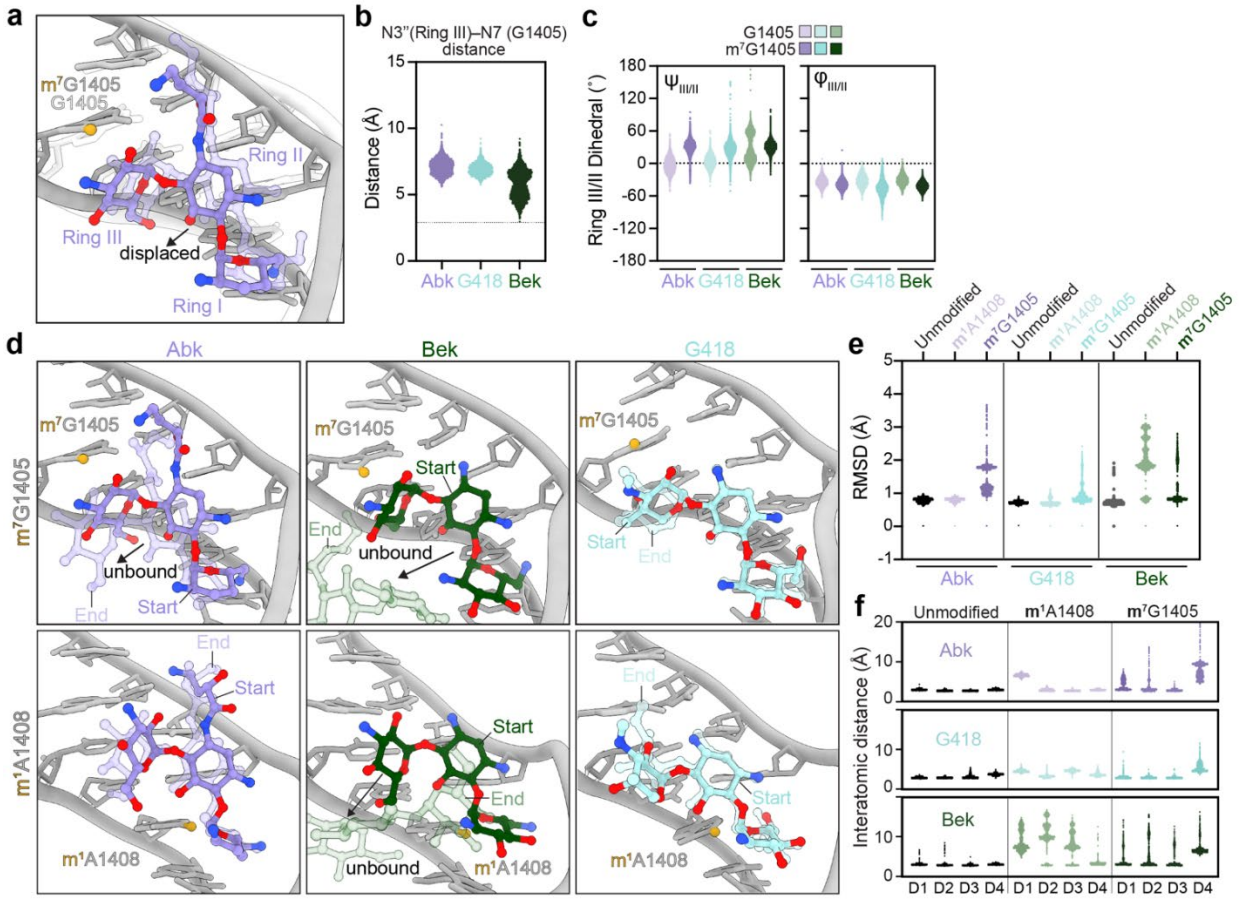

Fig. 7 | 4,6-DOS aminoglycosides fail to adapt to m^{7}G1405 modified rRNA. a, Structural superposition of simulated Abk binding to m^{7}G1405-modified (opaque drug, gray RNA) and unmodified (semi-transparent drug, white RNA) A-site rRNA. The indicated displacement of Abk from h44 by m^{7}G1405 causes a loss of hydrogen bonds between Abk and the rRNA. **b**, Interatomic distances between atom N7 of m^{7}G1405 and the Ring III 3''-NH_3^+ of Abk, G418, and Bek, from classical MD simulations are greater than 4 Å, precluding hydrogen bonding with G1405. **c**, Dihedral angle differences along the Ring III/II glycosidic linkage of Abk, G418, and Bek bound to unmodified and m^{7}G1405-modified rRNA from classical MD simulations. **d**, Structural superpositions of unmodified, m^{1}A1408-modified and m^{7}G1405-modified A-site rRNA bound to Abk, G418, and Bek in REST simulations, showing unbinding events in Bek and Amk when simulated with a m^{7}G1405-modified A site. **e**, RMSD of aminoglycoside-RNA complexes in REST simulations shows an increased range of RMSD for Bek, G418, and Abk when rRNA is modified at m^{7}G1405, with only Bek showing a similar increase when the rRNA is modified at

m^1A1408. **f**, Interatomic distance measurements–D1: N6’ (Ring I)-N1(A1408), D2: N3 (Ring II)-OP1 (A1493), D3: N1 (Ring II)-O4 (U1495), and D4: N3" (Ring III)-N7 (G1405)–reveal larger distance distributions for Bek, G418, and Abk when rRNA is modified at G1405, but only for Bek when rRNA is modified at m^1A1408, aligning with the observed changes in MICs in response to these resistance modifications.

SUPPLEMENTARY INFORMATION

Basis for selective drug evasion of an aminoglycoside-resistance ribosomal RNA modification

Debayan Dey[1*], Jacob Mattingly[2,3*], Natalia Zelinskaya[1], Christine M. Dunham[2†] and Graeme L Conn[1†]

[1]Department of Biochemistry, Emory University School of Medicine, Atlanta, GA 30322

[2]Department of Chemistry, Emory University, Atlanta, GA 30322

[3]Graduate Program in Biochemistry, Cell, and Developmental Biology (BCDB), Emory University, Atlanta, GA 30322

*Co-first authors.

[†]Correspondence may be addressed to: Christine M. Dunham, cmdunha@emory.edu or Graeme L. Conn, gconn@emory.edu.

This file contains:

Supplementary Figures 1-8

Supplementary Tables 1-9

SUPPLEMENTARY FIGURES

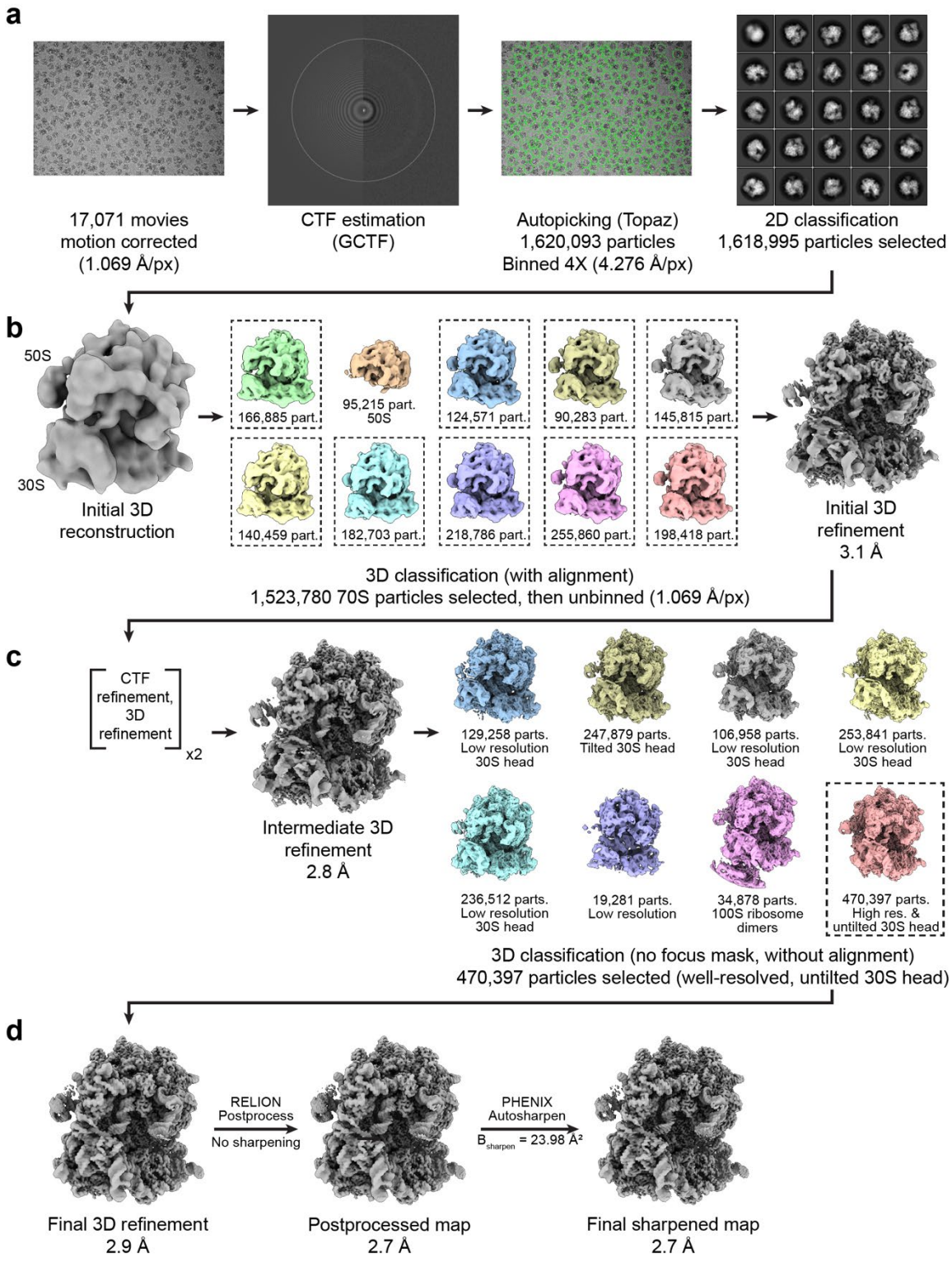

Supplementary Fig. 1. 70S (A1408)-Abk cryo-EM processing pipeline. a, Micrograph preprocessing, particle picking, and reference-free 2D classification to isolate ribosome-like particles (1,618,995 particles selected). **b**, Initial 3D reconstruction, 3D classification with particle alignment to isolate 70S ribosome particles (1,523,780 selected), and initial 3D auto-refinement. **c**, Iterative CTF refinement and 3D auto-refinement followed by unmasked 3D classification without particle alignment to isolate 70S particles with unratcheted 30S subunits and unswiveled 30S head domains (470,397 selected). **d**, Final 3D refinement, solvent masking (postprocessing) to calculate final map resolution (2.7 Å), and PHENIX Autosharpen to prepare final map for molecular modeling ($B_{sharpen}$ = 23.98 $Å^2$).

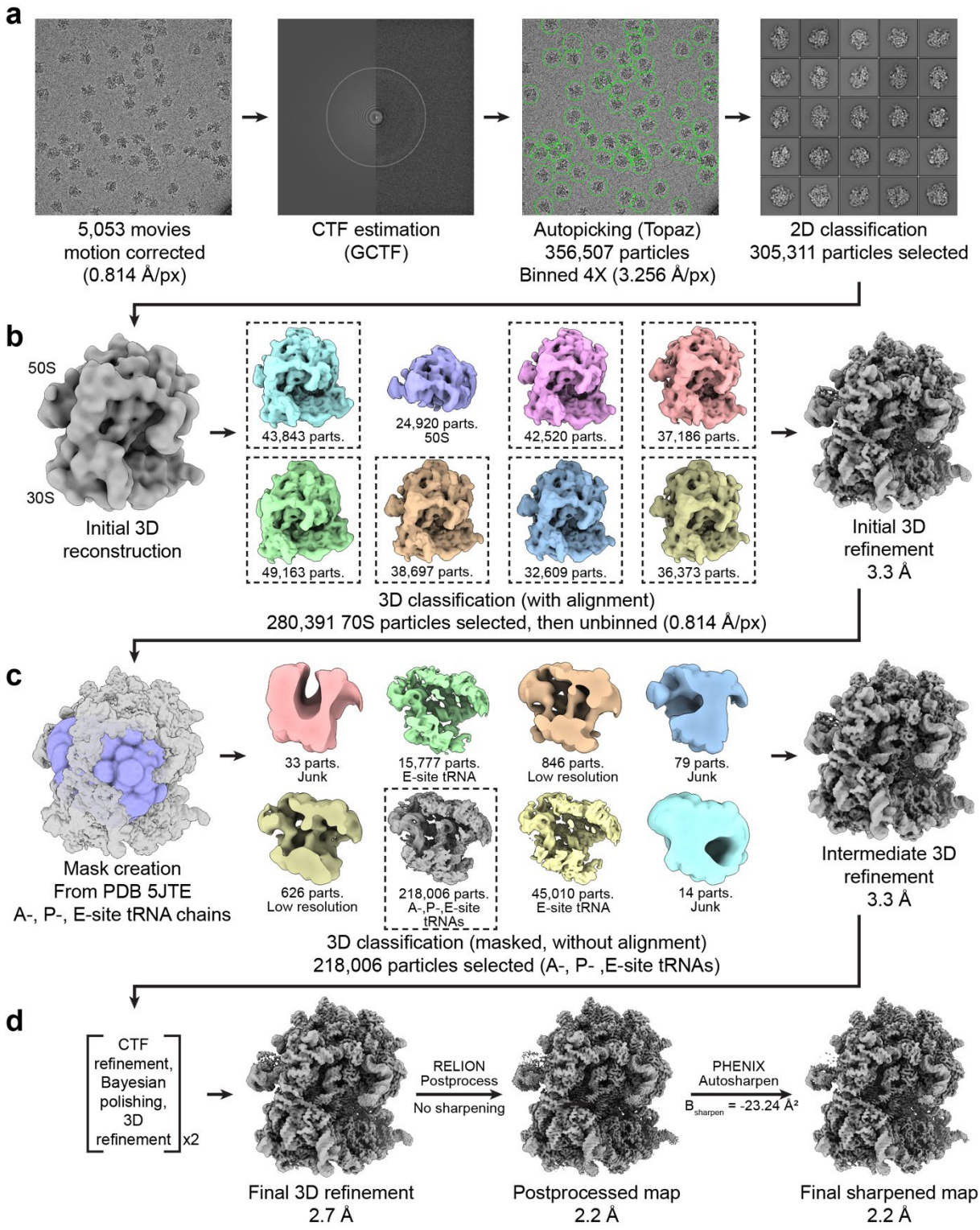

Supplementary Fig. 2. 70S (m^1A1408)-Abk cryo-EM processing pipeline. a, Micrograph preprocessing, particle picking, and reference-free 2D classification to isolate ribosome-like particles (305,311 particles selected). **b**, Initial 3D reconstruction, 3D classification with particle

alignment to isolate 70S ribosome particles (280,391 selected), and initial 3D auto-refinement. **c**, A, P, and E site focus mask creation from PDB 5JTE, focused 3D classification without particle alignment (218,006 selected), and 3D auto-refinement of particles containing A-, P-, and E-site tRNAs. **d**, Iterative CTF refinement, Bayesian polishing, and 3D auto-refinement followed by final 3D refinement, solvent masking (postprocessing) to calculate final map resolution (2.2 Å), and PHENIX Autosharpen to prepare final map for molecular modeling ($B_{sharpen}$ = -23.24 $Å^2$).

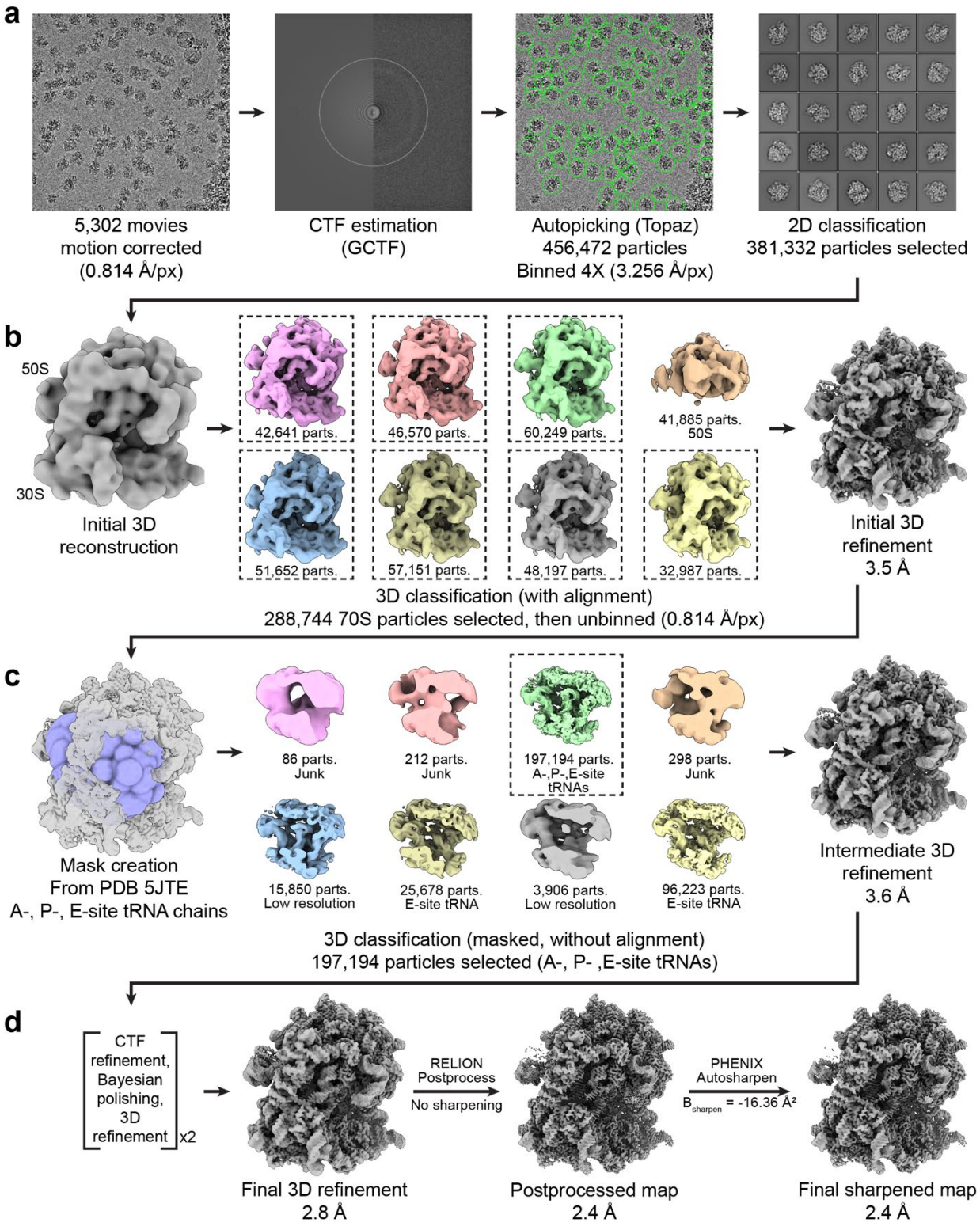

Supplementary Fig. 3. 70S (m^1A1408)-G418 cryo-EM processing pipeline. a, Micrograph preprocessing, particle picking, and reference-free 2D classification to isolate ribosome-like

particles (381,332 particles selected). **b**, Initial 3D reconstruction, 3D classification with particle alignment to isolate 70S ribosome particles (288,744 selected), and initial 3D auto-refinement. **c**, A-, P,- and E-site focus mask creation from PDB 5JTE, focused 3D classification without particle alignment (197,194 selected), and 3D auto-refinement of particles containing A-, P-, and E-site tRNAs. **d**, Iterative CTF refinement, Bayesian polishing, and 3D auto-refinement followed by final 3D refinement, solvent masking (postprocessing) to calculate final map resolution (2.4 Å), and PHENIX Autosharpen to prepare final map for molecular modeling ($B_{sharpen}$ = -16.36 $Å^2$).

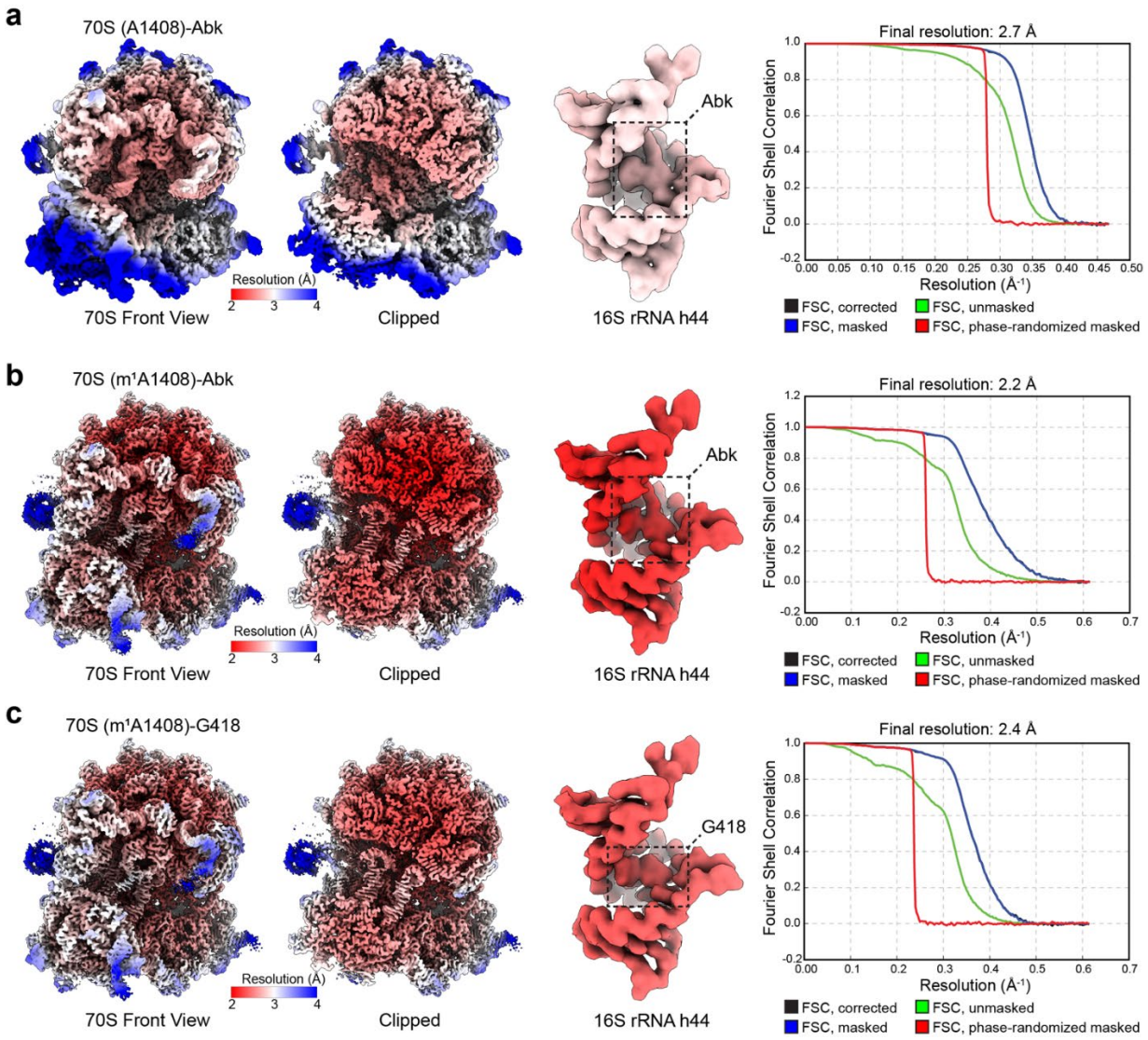

Supplementary Fig. 4. Cryo-EM local resolution maps and Fourier shell correlation curves. **a**, 70S (A1408)-Abk local resolution maps (*left:* 70S front view; *middle:* clipped for visibility of tRNA binding sites; *right:* 16S rRNA h44 aminoglycoside binding site) and FSC curve (resolution of 2.7 Å at FSC=0.143 cutoff). **b**, 70S (m^1A1408)-Abk local resolution maps (shown in same views as *panel A*) and FSC curve (resolution of 2.2 Å at FSC=0.143 cutoff). **c**, 70S (m^1A1408)-G418 local resolution maps (shown in same views as *panel A*) and FSC curve (resolution of 2.4 Å at FSC=0.143 cutoff).

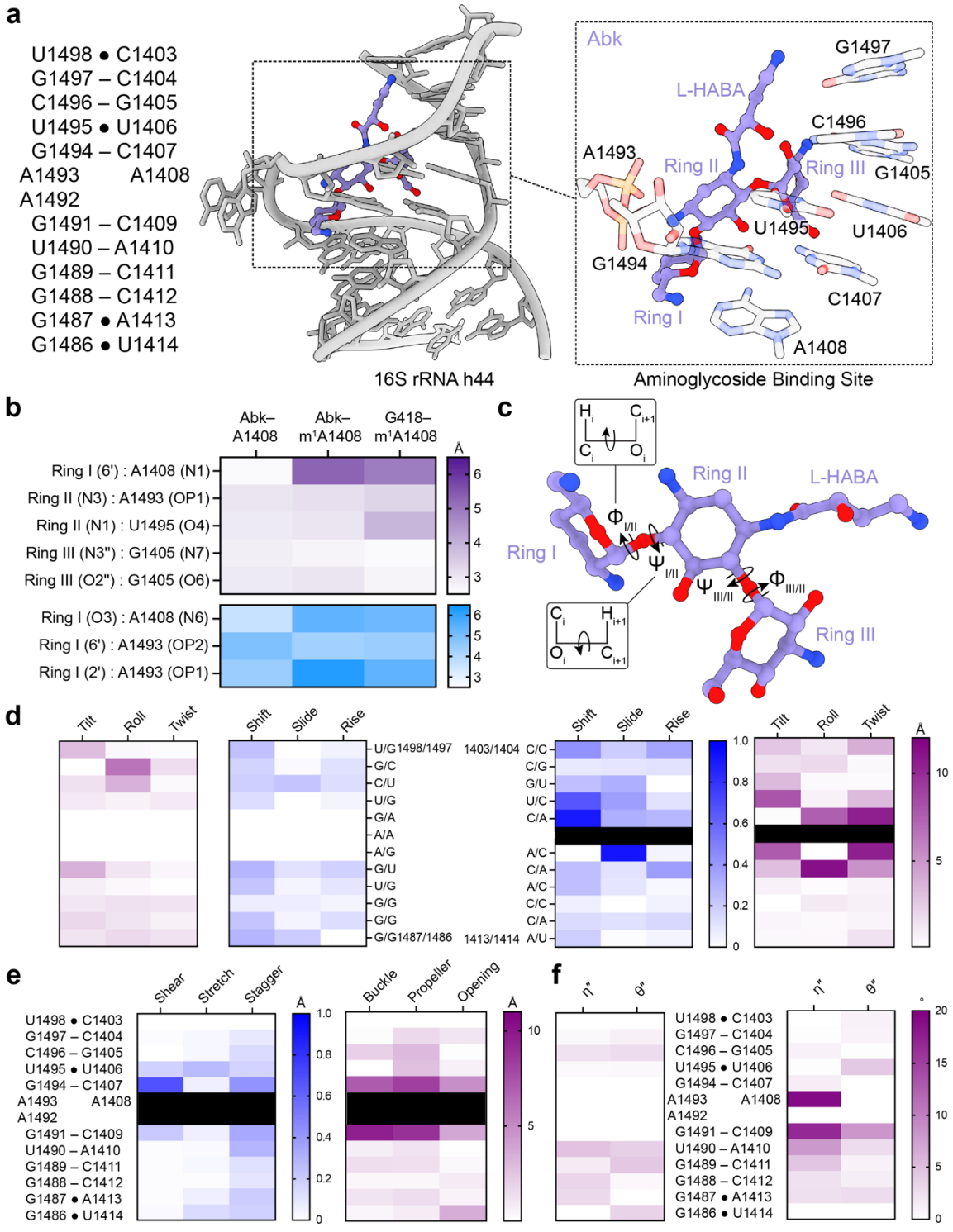

Supplementary Fig. 5. Conformational changes in aminoglycosides and the A-site RNA. a, Sequence and structure of the A-site RNA bound to the aminoglycoside arbekacin (Abk), highlighting interactions with key residues within the A site. **b**, Heatmap showing the calculated

interatomic distances for Abk when bound to both unmodified and m^1A1408-modified RNA, as well as for G418 bound to m^1A1408-modified RNA. The heatmap includes color legends denoting the distance variations. **c**, Structure of Abk with the glycosidic dihedral angles Φ (Phi) and Ψ (Psi) shown for Ring I/II and Ring III/II, illustrating the conformational details of 4,6-DOS aminoglycosides. Differences in A1408 and m1A1408 RNA conformations when bound to Abk, calculated by comparing the absolute changes in **d**, base pair, **e**, base step parameters, and **f**, pseudo-dihedral angles η″ and θ″, which measure twist and bending in the RNA backbone.

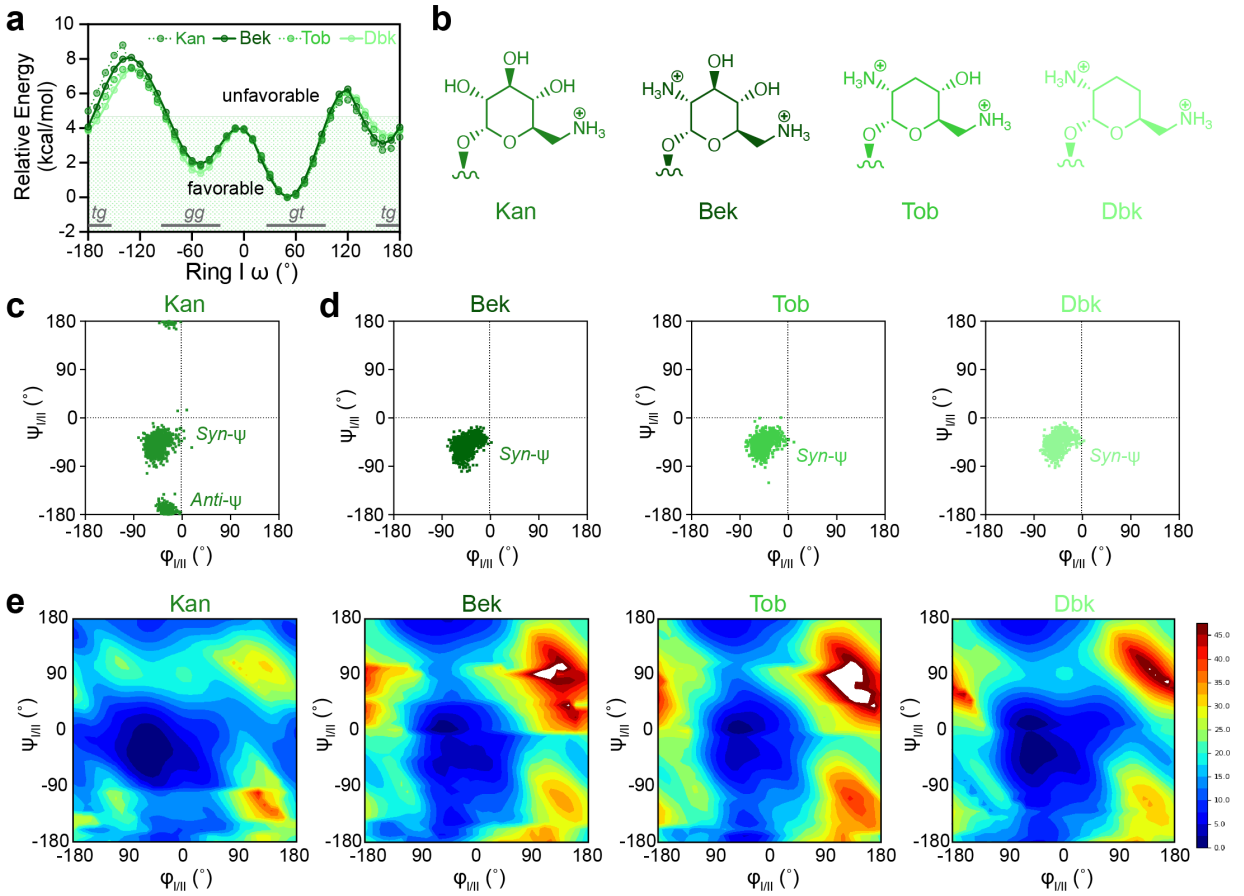

Supplementary Fig. 6. Conformation of kanamycin scaffold aminoglycosides. a, Potential energy landscape of omega (ω) angle of kanamycin scaffold in aminoglycosides using the OPLS4 force field, with blue shaded region being energetically permissible. **b**, Comparison of the Ring I chemical structure in Kan, Bek, Tob and Dbk. **c,d**, Plot of $\Phi_{I/II}$/ $\Psi_{I/II}$ values from MD simulations of free Kan, Bek, Tob and Dbk. **e**, Potential energy landscape scanning $\Phi_{I/II}$/$\Psi_{I/II}$ using the OPLS4 force field for Kan, Bek, Tob and Dbk.

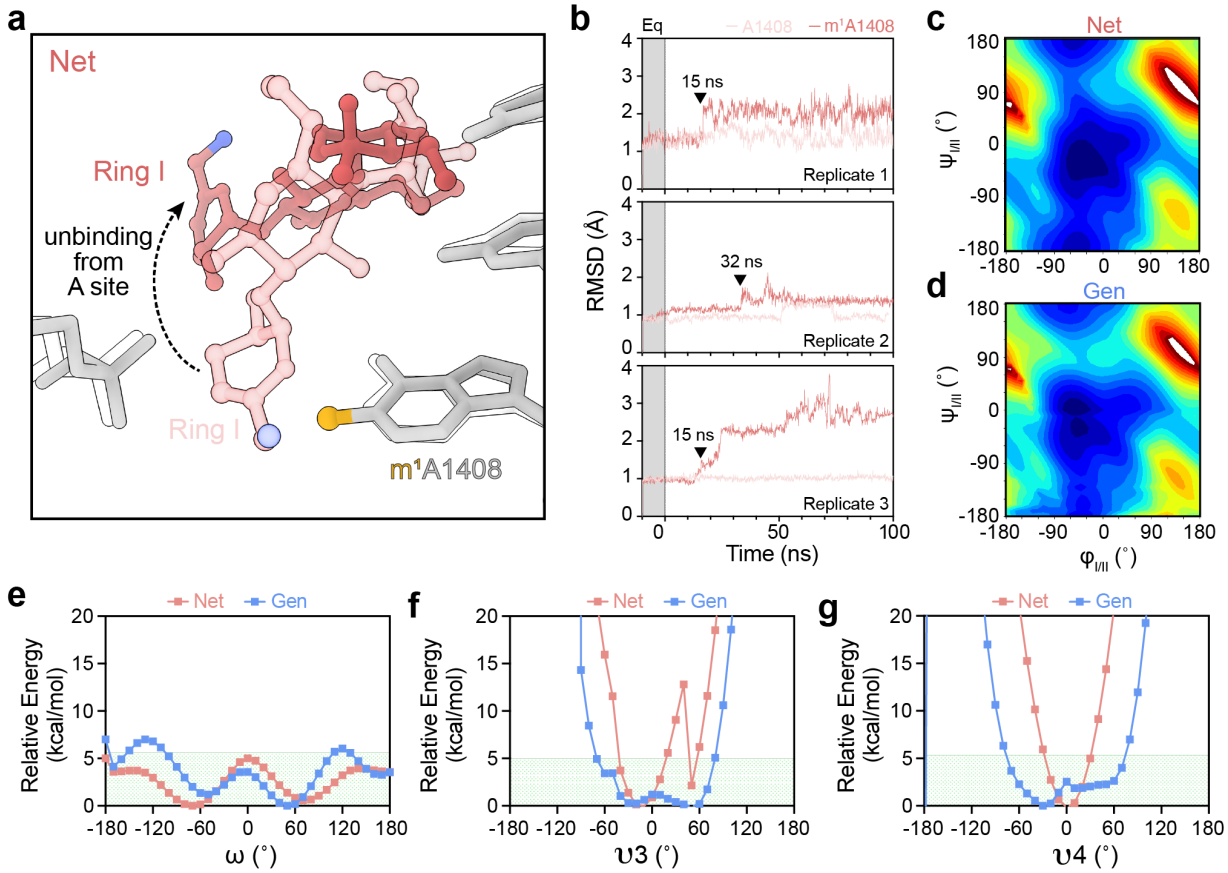

Supplementary Fig. 7. The conformational rigidity in Net restricts adaptation to m^{1}A1408. **a**, Superposition of simulated Net binding to unmodified (white RNA and light red drug) and m^{1}A1408-modified (gray RNA, and red drug) A-site rRNA, showing that Net dissociates from the latter complex. **b**, RMSD plot of Net bound to unmodified (light red) and m^{1}A1408-modfied (red) rRNA in the three independent replicate simulations. **c,d**, Potential energy landscapes scanning $\Phi_{I/II}/\Psi_{I/II}$ using the OPLS4 force field for Net and Gen, respectively, which have similar Ring I structure, except for the carbon-carbon double bond in Net. **e-g**, Potential energy plots of Net (red) and Gen (blue) scanning ω, υ3 and υ4 dihedral angles in Ring I, respectively. Green shading indicates the energetically permissible dihedral values.

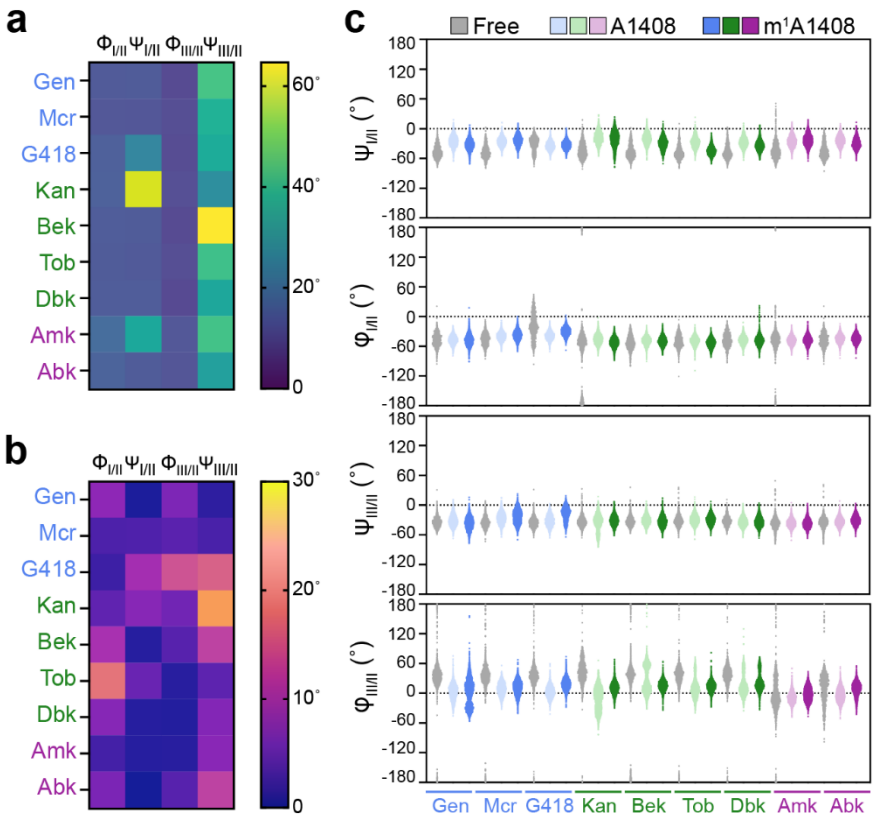

Supplementary Fig. 8. Differences in flexibility and adaptability of aminoglycosides. a, Standard deviation (SD) of all glycosidic dihedral angles for aminoglycosides free in solution, which serves as a proxy for flexibility with higher SD indicating greater flexibility. **b**, Shifts in mean dihedral angles for aminoglycosides bound to both unmodified and modified rRNA. **c**, Comparison of Ring I/II and Ring III/II dihedral angles for free aminoglycosides and bound to both unmodified and modified rRNA and free in solution.

SUPPLEMENTARY TABLES

Table S1. Aminoglycoside activity in absence and presence of 16S rRNA resistance modifications m^1A1408 (NpmA) and m^7G1405 (RmtB)

DOS	Aminoglycoside	MIC (μg/ml)[a]		
		Empty vector	**pET-*npmA***	**pET-*rmtB***
4,6-	Kanamycin A (Kan)	1	>1024	>1024
	Bekanamycin (Bek)	0.5	1024	>1024
	Tobramycin (Tob)	1	512-256	512
	Dibekacin (Dbk)	0.5	512	>1024
	Amikacin (Amk)	0.5	8	>1024
	Arbekacin (Abk)	0.5	8	512
	Gentamicin C1A (Gen)	0.5	64/128	>1024
	Micronomicin (Mcr)	0.5	64	>1024
	G418	0.5	32	>1024
	Netilmicin (Net)	0.5	>1024	>1024
4,5-	Paromomycin (Par)	4	32	8
	Neomycin (Neo)	1	128	8

[a]For pET44 vector encoding aminoglycoside-resistance 16S rRNA methyltransferases NpmA (m^1A1408 modification) or RmtB (m^7G1405 modification) in *E. coli* BL21(DE3). Empty vector lacks encoded enzyme but was otherwise treated identically.

Table S2. Cryo-EM data collection and model statistics.

	70S (A1408)-Abk	70S (m^1A1408)-Abk	70S (m^1A1408)-G418
Deposition			
EMDB accession	EMD-44193	EMD-44192	EMD-44194
PDB ID	9B50	9B4Z	9B51
Data collection			
Microscope	TFS Krios	TFS Krios	TFS Krios
Detector	Gatan K3 BioQuantum	TFS Falcon 4i	TFS Falcon 4i
Voltage (keV)	300	300	300
Electron exposure ($e^-/Å^2$)	52	50	50
Pixel size (Å)	1.069	0.814	0.814
Defocus range (μm)	-0.5–3.5	-0.5–2.5	-0.5–2.5
Frames per movie	40	29	29
Micrographs (#)	17,071	5,053	5,302
Initial particles (#)	1,620,093	356,507	456,472
Final particles (#)	470,397	218,006	197,194
Model composition, refinement and validation statistics			
Composition			
Total Atoms	141,469	146,493	146,485
Residues: Protein	5,534	5,534	5,534;
RNA	4,554	4,789	4,789
Ligands: Mg	309	309	309
Zn	2	2	2
Abk	2	2	–
G418	–	–	2
Bonds (RMSD)			
Length (Å) (# > 4σ)	0.006 (4)	0.004 (10)	0.004 (9)
Angles (°) (# > 4σ)	0.697 (6)	0.669 (22)	0.672 (11)
MolProbity score	1.92	1.93	1.85
Clash score	6.01	5.17	4.80
Ramachandran plot (%)			
Outliers	0.64	0.68	0.70
Allowed	8.28	7.44	7.66
Favored	91.07	91.88	91.64
Rotamer outliers (%)	1.26	1.65	1.37
Cβ outliers (%)	0.00	0.00	0.00
Peptide plane (%)			
Cis proline/general	0.0/0.0	0.0/0.0	0.0/0.0
Twisted proline/general	0.0/0.0	0.0/0.0	0.0/0.0
CaBLAM outliers (%)	5.01	4.77	4.99
ADP (B factors): min/max/mean			
Protein	17.71/167.64/74.00	12.93/170.73/66.92	16.11/192.80/68.75
Nucleotide	15.31/364.76/82.90	13.47/443.70/95.21	0.00/287.71/76.88
Ligand	20.00/156.32/56.92	20.00/130.77/71.90	20.00/122.79/49.19
Resolution Estimates (Å): Masked (Unmasked)			
d FSC (half maps; 0.143)	2.7 (2.8)	2.2 (2.4)	2.4 (2.6)
d 99 (full/half1/half2)	3.2/3.0/3.0 (3.1/2.3/2.3)	3.0/2.3/2.3 (3.0/1.9/1.9)	3.0/2.2/2.2 (3.0/1.8/1.8)
d model	3.0 (3.0)	2.6 (2.6)	2.8 (2.8)

d FSC model (0/0.143/0.5)	2.6/2.7/2.8 (2.6/2.7/2.9)	2.1/2.2/2.7 (2.2/2.3/2.8)	2.3/2.4/2.6 (2.4/2.5/2.8)
Map min/max/mean	-10.80/28.70/0.24	-7.71/29.09/0.28	-7.98/28.55/0.27
Model vs. Data			
CC (mask)	0.91	0.87	0.91

Table S3. Aminoglycoside and A-site rRNA interatomic distances.

	Distance (Å)		
	70S (A1408)–Abk	70S (m^1A1408)–Abk	70S (m^1A1408)–G418
Ring I (6') : A1408 (N1)	2.6	5.3	4.9
Ring II (N3) : A1493 (OP1)	3.0	3.1	3.3
Ring II (N1) : U1495 (O4)	2.9	3.0	3.9
Ring III (N3") : G1405 (N7)	2.8	2.7	2.6
Ring III (O2") : G1405 (O6)	2.9	3.0	2.7
Ring I (O3) : A1408 (N6)	3.6	5.4	5.2
Ring I (6') : A1493 (OP2)	4.9	4.3	4.4
Ring I (2') : A1493 (OP1)	4.4	6.2	5.4

Table S4. Dihedral angles of aminoglycoside glycosidic linkages, 6’ configuration and Ring I puckering parameters.

Dihedral angle (˚)/ ring puckering parameter	70S (A1408)–Abk	70S (m^1A1408)–Abk	70S (m^1A1408)–G418
$\varphi_{I/II}$	-46.5	-27.5	-35.4
$\psi_{I/II}$	-29.2	-29.8	-28.9
ω	26.0	57.0	71.0
*ϑ*1	49.3	55.1	54.0
*ϑ*2	-51.3	-53.1	-61.9
*ϑ*3	53.1	49.8	68.7
*ϑ*4[a]	-53.9	48.8	-69.7
*ϑ*5	52.7	50	61.2
Phase angle	-21.0	60.2	-5.7
Puckering amplitude	0.8	1.4	1

[a]*ϑ*1 (49.3 to 55.1), *ϑ*2 (-61.9 to -51.3), *ϑ*3 (49.8 to 68.7), and *ϑ*5 (50.0 to 61.2) were similar for all three structures.

Table S5. Dihedral angle (Ring I/II) changes in the MD simulations[a]

Aminoglycosides	Unmodified rRNA		m^{1}A1408 modified *gt*			Δ *gt*[b]		m^{1}A1408 modified *tg*			Δ *tg*[b]	
	$\Phi_{I/II}$	$\Psi_{I/II}$	%	$\Phi_{I/II}$	$\Psi_{I/II}$	$\Delta\Phi_{I/II}$	$\Delta\Psi_{I/II}$	%	$\Phi_{I/II}$	$\Psi_{I/II}$	$\Delta\Phi_{I/II}$	$\Delta\Psi_{I/II}$
Gentamicin C1A (Gen)	-24.6	-47.1	19	-35.7	-41.9	11.1	5.2	72	-30.6	-49.7	6.0	2.6
Micronomicin (Mcr)	-25.8	-39.8	81	-22.7	-36.5	3.1	3.3	14	-26.5	-41.3	0.7	1.5
G418	-34.1	-39.2	99	-32.6	-30.1	1.5	9.1	0	-	-	-	-
Neomycin (Neo)	-26	-46.6	5	-35.1	-41.5	9.1	5.1	80	-23.9	-42.5	2.1	4.1
Paromomycin (Par)	-32.4	-43.3	93	-34.7	-42.1	2.3	1.2	0	-	-	-	-
Kanamycin A (Kan)	-17.4	-45.5	35	-11.6	-54.7	5.8	9.2	50	-28.4	-49.1	11.0	3.6
Bekanamycin (Bek)	-19.9	-48.9	8	-31.4	-50	11.5	1.1	80	-28.7	-49.5	8.8	0.6
Tobramycin (Tob)	-26.7	-49	11	-38.4	-50.9	11.7	1.9	69	-44.4	-54	17.7	5
Dibekacin (Dbk)	-27	-47.7	3	-26.8	-41.9	0.2	5.8	90	-33.7	-48.6	6.7	0.9
Amikacin (Amk)	-24.7	-48.2	21	-15.8	-49.3	8.9	1.1	62	-25.6	-46	0.9	2.2
Arbekacin (Abk)	-23.4	-44.8	10	-15.4	-39.4	8.0	5.4	85	-30.6	-45.4	7.2	0.6

[a]The MD simulations refer to the unmodified and m^{1}A1408-modified rRNA. The terms *gt* and *tg* represent the populations of simulations where the Ring I ω angle falls within the *gt* and *tg* ranges, respectively. The corresponding average dihedral angles for each population are reported. Some conformations do not fall into either the *gt* or *tg* categories, so the total population does not sum to 100%.
[b]The term *Δtg* and *Δgt* refers to the absolute value of the changes in dihedral angles when transitioning from the conformation bound to the unmodified rRNA to the one bound to the modified rRNA.

Table S6. Ligand strain energy from *tg* adaptation

Aminoglycosides[a]	Ligand strain energy (Kcal/mol)			
	Rep A	Rep B	Rep C	Average
Kanamycin A (Kan)	14.7	15.4	20.4	16.8
Bekanamycin (Bek)	15.1	13.4	10.6	13.0
Tobramycin (Tob)	9.0	8.5	10.6	9.4
Dibekacin (Dbk)	6.5	3.6	7.7	5.9

Table S7. Average H-bond between aminoglycosides and rRNA in MD simulations

Aminoglycosides	H-Bond		Salt bridge	
	A1408	m^{1}A1408	A1408	m^{1}A1408
Gentamicin C1A (Gen)	7.6	6.0	3.6	3.5
Micronomicin (Mcr)	7.5	5.9	2.9	3.6
G418	10.5	7.1	2.8	3.1
Neomycin (Neo)	12	10.8	5.4	5.3
Paromomycin (Par)	12.9	11.2	5.1	5.5
Kanamycin A (Kan)	10	8.8	3.6	4.0
Bekanamycin (Bek)	10	8.7	5.0	4.8
Tobramycin (Tob)	8.9	8.5	4.7	5.6
Dibekacin (Dbk)	7.8	6.3	4.8	5.0
Amikacin (Amk)	12.5	10.9	4.4	4.2
Arbekacin (Abk)	9.7	7.5	4.6	4.4

Table S8. Mean and standard deviations (SD) of Ring I/II and Ring III/II dihedral angles in the rRNA-bound and free states of 4, 6-DOS aminoglycosides in MD simulations[a]

State	Aminoglycosides	$\Phi_{I/II}$ (˚)		$\Psi_{I/II}$ (˚)		$\Phi_{III/II}$ (˚)		$\Psi_{III/II}$ (˚)	
		Mean	*SD*	Mean	*SD*	Mean	*SD*	Mean	*SD*
Free	Gentamicin C1A (Gen)	**-45.9**	*13.3*	**-47.3**	*13.6*	**-34.3**	*10.1*	**33.2**	*44.4*
	Micronomicin (Mcr)	**-46.9**	*12.8*	**-46.2**	*12.6*	**-34.5**	*10.7*	**33.4**	*38.5*
	G418	**-30.9**	*14.6*	**-19.9**	*25.0*	**-34.9**	*10.4*	**34.6**	*36.5*
	Kanamycin A (Kan)	**-43.1**	*14.9*	**-61.5**	*60.2*	**-32.7**	*11.1*	**43.6**	*27.4*
	Bekanamycin (Bek)	**-46.4**	*13.9*	**-52.9**	*13.7*	**-31.7**	*10.1*	**24.0**	*64.7*
	Tobramycin (Tob)	**-47.2**	*13.6*	**-49.4**	*13.1*	**-31.3**	*10.7*	**31.2**	*43.3*
	Dibekacin (Dbk)	**-46.3**	*13.9*	**-47.3**	*13.9*	**-31.6**	*10.0*	**34.6**	*34.6*
	Amikacin (Amk)	**-42.7**	*17.6*	**-48.4**	*35.1*	**-37.0**	*12.8*	**-2.6**	*43.8*
	Arbekacin (Abk)	**-44.1**	*15.4*	**-47.3**	*13.6*	**-35.1**	*12.3*	**10.0**	*32.3*
A1408	Gentamicin C1A (Gen)	**-24.6**	*11.1*	**-47.1**	*8.7*	**-30.6**	*11.6*	**2.7**	*15.5*
	Micronomicin (Mcr)	**-25.8**	*9.0*	**-39.8**	*8.2*	**-26.2**	*11.5*	**8.8**	*12.8*
	G418	**-34.1**	*8.7*	**-39.2**	*8.1*	**-31.3**	*11.4*	**3.3**	*12.5*
	Kanamycin A (Kan)	**-17.4**	*12.5*	**-45.5**	*9.9*	**-35.4**	*17.2*	**-10.7**	*23.4*
	Bekanamycin (Bek)	**-19.9**	*11.5*	**-48.9**	*8.6*	**-30.1**	*9.8*	**27.0**	*27.0*
	Tobramycin (Tob)	**-26.7**	*11.3*	**-49.0**	*9.0*	**-28.7**	*10.0*	**10.1**	*19.3*
	Dibekacin (Dbk)	**-27.0**	*10.3*	**-47.7**	*8.7*	**-33.6**	*9.5*	**15.9**	*21.0*
	Amikacin (Amk)	**-24.7**	*11.3*	**-48.2**	*8.5*	**-36.1**	*8.6*	**-8.4**	*11.5*
	Arbekacin (Abk)	**-23.4**	*10.3*	**-44.8**	*8.5*	**-33.2**	*9.4*	**-3.3**	*13.9*
m^{1}A1408	Gentamicin C1A (Gen)	**-31.8**	*11.3*	**-47.4**	*11.5*	**-36.4**	*13.0*	**1.9**	*27.3*
	Micronomicin (Mcr)	**-23.3**	*10.9*	**-37.2**	*10.0*	**-22.8**	*14.2*	**11.1**	*15.0*
	G418	**-32.6**	*8.5*	**-30.1**	*8.9*	**-17.5**	*14.0*	**18.5**	*12.2*
	Kanamycin A (Kan)	**-21.1**	*16.5*	**-52.2**	*10.0*	**-30.5**	*10.5*	**10.9**	*12.1*
	Bekanamycin (Bek)	**-29.4**	*11.8*	**-49.6**	*9.1*	**-33.1**	*10.6*	**15.4**	*10.4*
	Tobramycin (Tob)	**-43.9**	*9.5*	**-53.3**	*9.2*	**-29.4**	*10.0*	**13.6**	*10.9*
	Dibekacin (Dbk)	**-33.4**	*10.4*	**-48.3**	*9.8*	**-33.1**	*10.4*	**22.2**	*17.9*
	Amikacin (Amk)	**-22.6**	*12.6*	**-47.7**	*9.4*	**-36.8**	*9.5*	**-1.6**	*14.5*
	Arbekacin (Abk)	**-29.0**	*11.0*	**-44.9**	*8.9*	**-30.1**	*9.8*	**8.3**	*14.8*

[a]The MD simulations refer to the aminoglycoside-A1408 or -m^{1}A1408 rRNA and ”free” refers to simulations of aminoglycoside in free state. $\Phi_{I/II}$, $\Psi_{I/II}$, $\Phi_{III/II}$, and $\Psi_{III/II}$ refer to the glycosidic dihedral angles between Rings I and II, and Rings III and I. A higher SD indicates greater flexibility or conformational variability in dihedral angles, while a lower SD suggests more rigidity.

Table S9. Average changes in Ring I/II and Ring III/II dihedral angles of 4, 6-DOS aminoglycosides in unmodified compared to m[1]A1408-modified rRNA in MD simulations.

Aminoglycosides	Average Δ (˚)			
	$\Delta\Phi_{I/II}$	$\Delta\Psi_{I/II}$	$\Delta\Phi_{III/II}$	$\Delta\Psi_{III/II}$
Gentamicin C1A (Gen)	7.2	0.3	5.8	0.9
Micronomicin (Mcr)	2.5	2.6	3.3	2.3
G418	1.6	9.1	13.7	15.2
Kanamycin A (Kan)	3.7	6.6	4.9	21.6
Bekanamycin (Bek)	9.5	0.6	3.1	11.7
Tobramycin (Tob)	17.2	4.3	0.7	3.5
Dibekacin (Dbk)	6.5	0.6	0.5	6.3
Amikacin (Amk)	2.0	0.6	0.7	6.8
Arbekacin (Abk)	5.6	0.1	3.1	11.7

[a]The MD simulations refer to the unmodified and m¹A1408-modified rRNA simulation with aminoglycosides.

Chapter 4: Discussion

Accurately producing proteins from information stored in genes is a critical function of all organisms[1]. The work presented here provides important structural insights into bacterial translational fidelity, revealing how weakening RNA-RNA interactions between the bacterial initiator tRNA ($tRNA^{fMet}$) and the ribosome disrupts translation initiation and suggesting a potential mechanism by which the initiation factor IF2 restores normal initiation. This work has also uncovered several structural principles governing the ability of ribosome-targeting aminoglycoside antibiotics to evade 16S rRNA A1408 methylation-mediated mediated resistance, an increasingly prevalent mode of resistance which threatens the efficacy of these crucial antibiotics of last resort. These principles can be used to design improved aminoglycoside scaffolds, preserving the utility of this essential antibiotic class as resistant infections become increasingly common.

4.1: Initiation is fine-tuned for a mixture of accuracy and efficiency

Results from this dissertation and prior studies of bacterial translation initiation suggest that initiation is optimized for a balance of accuracy and efficiency based on the strength of interactions between fMet-$tRNA^{fMet}$, the ribosome, and the mRNA codon. Productive initiation requires both strong tRNA-mRNA base pairing at the start codon and robust tRNA-ribosome interactions along the anticodon stem[2-5]. The strength of these interactions affects the thermodynamic and kinetic stability of initiation complexes, with weaker interactions increasing tRNA off-rates from the 30S ribosomal subunit[2, 6]. The initiator tRNA off-rate likely plays a role in start codon selection, as strengthening the interactions of $tRNA^{fMet}$ with the ribosome through the 16S rRNA mutation G1338A (and hence reducing the tRNA off-rate) causes spurious initiation at noncanonical start codons[5, 7]. Conversely, weakening these interactions through mutations in the $tRNA^{fMet}$ anticodon stem reduces the preference for the canonical but near-cognate start codons

GUG and UUG (where “near-cognate” defines tRNA-mRNA pairings having a single base pair mismatch)[2]. Notably, the tRNA-mRNA interaction strength does not appear to directly affect tRNA-ribosome interactions at the tRNA minor groove, as cryo-EM structures of 70S initiation complexes reveal similar tRNA-ribosome interaction distances for all four NUG start codons paired with $tRNA^{fMet}$ M1[8].

A view of initiation as a finely tuned process balancing speed and accuracy aligns with observations of other steps of the translation cycle, such as elongation. Because protein function typically tolerates minor substitutions in amino acid sequence[9, 10], and because protein synthesis rate is a major limiting factor to bacterial growth in nutrient-rich conditions[11-14], ribosomes can afford a higher error rate (1 error per 10^3-10^4 amino acids during elongation) than DNA or RNA polymerases (where errors could have a more pronounced effect on cellular function and fitness) in exchange for a higher rate of protein synthesis[15-19]. Notably, mutations conferring hyperaccuracy to bacterial ribosomes at the expense of elongation speed often reduce fitness[20-23]. Similarly, it appears that the ribosome is tuned for an intermediate level of speed and accuracy during initiation. The type-II A-minor interaction between the conserved 16S nucleotide G1338 and $tRNA^{fMet}$ nucleotide C41 is of suboptimal strength[24, 25]; the mutation G1338A strengthens the interaction between the ribosome and tRNA minor groove at this position, yielding ribosomes with increased translational activity but with a propensity to undergo spurious initiation on non-start codons[5, 7]. Conversely, mutations of 16S nucleotide A1339, which weaken the interaction of the ribosome with the tRNA minor groove at this position, greatly reduce translational activity[3, 4, 6]. This suggests that balancing speed and accuracy is a general principle of ribosomal function across multiple stages of the translation cycle, with fitness penalties resulting from shifting this balance in either direction.

4.2: The role of IF2 in quality control during translation initiation

Prior biochemical studies of 30S and 70S initiation complexes have shown that IF2 serves a quality control function during initiation, rescuing normal initiation when RNA-RNA interactions between the anticodon stem loop (ASL) of the initiator tRNA variant $tRNA^{fMet}$ M1 and the 16S rRNA are weakened. However, prior to the work presented in this dissertation, the mechanism by which this activity occurs remained an open question. Our structures of 70S initiation complexes reveal that IF2 strengthens the type-II A-minor interaction between 16S rRNA nucleotide G1338 and the $tRNA^{fMet}$ M1 ASL minor groove[8]. However, it remains unclear whether IF2-mediated strengthening of tRNA-ribosome interactions alone is responsible for restoration of normal initiation behavior in ICs containing $tRNA^{fMet}$ M1. Additionally, there are potential discrepancies between *in vitro* reconstituted and *in vivo* studies of translation initiation using $tRNA^{fMet}$ M1. *In vitro,* IF2 restores normal ribosome toeprint banding and peptide bond formation activity to ICs containing $tRNA^{fMet}$ M1 initiating translation on a CUG start codon. However, *in vivo*, $tRNA^{fMet}$ M1 drastically reduces translation activity by roughly 20-fold compared to wild type despite IF2 being present in living cells[26]. This decrease in *in vivo* translation rate is true even though the M1 variant does not exhibit a pronounced decrease in preference for the canonical AUG start codon (unlike the canonical but near-cognate start codons GUG and UUG), which is the predominant start codon used *in vivo*[2]. For this reason, it is unclear why $tRNA^{fMet}$ M1 reduces translation to such a degree *in vivo* despite initiation being rescued by IF2 *in vitro*.

Past competition binding assays have shown that $tRNA^{fMet}$ M1 forms ICs which are less thermodynamically and kinetically stable than those containing wild type $tRNA^{fMet}$. In particular, the M1 variant exhibits a markedly higher off-rate from the 30S subunit compared to wild type[2]. Because 30S ICs do not have a required order for assembly[27-29], *in vitro* assays where initiation factors are provided in excess of the concentration of ribosomes may involve substantial association of IF2 with 30S subunits before $tRNA^{fMet}$ M1 binds. In contrast, IFs in living cells are present at lower concentrations than that of ribosomes (roughly 0.2-0.3 molecules of IF2 per

ribosome in *E. coli*), suggesting that most 30S subunits would not have IF2 bound[30, 31]. Because $tRNA^{fMet}$ M1 has a shorter dwell time on 30S subunits during initiation than wild type $tRNA^{fMet}$, and because the initiation factor IF3 is known to increase both the on-rate and off-rate of tRNAs on the 30S subunit during initiation[32, 33], it may be the case that $tRNA^{fMet}$ M1 does not typically associate with 30S for long enough *in vivo* for IF2 to find it bound to 30S. However, in *in vitro* assays where IF2 is provided in excess, 30S subunits may already have IF2 bound when $tRNA^{fMet}$ M1 arrives, allowing IF2 to quickly drive productive initiation after arrival of the tRNA (Fig. 1). It should be possible to test whether the decreased dwell time of $tRNA^{fMet}$ M1 permits IF2 to rescue normal initiation in a concentration-dependent manner by measuring translation of a reporter protein in cells possessing either wild type $tRNA^{fMet}$ or $tRNA^{fMet}$ M1 as their sole initiator tRNAs with or without overexpression of IF2. If fast recognition of $tRNA^{fMet}$ M1-containing 30S pre-ICs by IF2 is sufficient to yield normal translation activity, then the discrepancy in reporter protein production between cells with wild type $tRNA^{fMet}$ and the M1 variant should be reduced upon IF2 overexpression.

While our cryo-EM data suggest that the interactions between IF2 and $tRNA^{fMet}$ are likely important for the ability of IF2 to restore normal initiation behavior to $tRNA^{fMet}$ M1 *in vitro*, it is possible that this quality control function may proceed through a mechanism independent of IF2's direct interaction with the $tRNA^{fMet}$ M1 acceptor end, instead depending only on the interactions of IF2 with the 30S ribosomal subunit. This possibility cannot be evaluated using wild type IF2, which interacts with both the 30S subunit and fMet-$tRNA^{fMet}$, but could be evaluated using an IF2 variant with abolished tRNA binding activity. IF2 variants deficient in $tRNA^{fMet}$ binding have been isolated from *Geobacillus stearothermophilus* (IF2 G715X, where X can represent the amino acids Glu, Val, Tyr, Lys, Asp, Pro, or Gln)[34]. Position G715 in *G. stearothermophilus* IF2 corresponds to G862 in *E. coli* (Fig. 2A), which is part of the tRNA-binding C2 domain of IF2 and contacts the fMet moiety at the tRNA acceptor end. To test the importance of IF2's interactions with fMet-

$tRNA^{fMet}$ M1 for its ability to rescue wild type-like initiation behavior, one could repeat toeprint assays analogous to those previously performed by the Fredrick Lab. Samples of non-enzymatically assembled 30S ICs containing $tRNA^{fMet}$ M1 and a CUG start codon, which display a banding pattern suggestive of altered mRNA position, could be tested alongside enzymatically assembled 30S ICs using either wild type IF2 or IF2 G862 substitution variants ("IF2 G862X"), with the expectation that the toeprint banding pattern of the IF2 G862X ICs should appear similar to that of the non-enzymatically assembled complexes if IF2 must interact with the tRNA acceptor end to rescue normal initiation (a sample gel schematic is shown in Fig. 2B). Observing a similar banding pattern in the samples containing WT IF2 and IF2 G862X would suggest that IF2's quality control function during initiation is not mediated by its interactions with the initiator tRNA, instead likely being mediated by its interactions with the 30S subunit of the ribosome. This may involve functions such as allosteric modification of the structure of the mRNA path.

4.3: The role of G1338 in stabilizing tRNA conformations adjacent to the P site

G1338 is conserved among bacteria, suggesting that its suboptimal interaction strength with the tRNA minor groove is likely important for its function. It is possible that maintaining intermediate-strength interactions with the tRNA minor groove (compared to the more strongly interacting 16S rRNA variant G1338A) could allow the 16S rRNA to dynamically strengthen or weaken its interaction with the P-site tRNA in different contexts depending on the tRNA conformation. For example, RNA footprinting experiments have demonstrated that G1338 is accessible to chemical probes when peptidyl-tRNA is bound to 70S ribosomes in the "classical" P/P orientation (where the tRNA occupies the P site on both subunits) but becomes protected following peptidyl transfer, after which the deacylated P-site tRNA can spontaneously move into the "hybrid" P/E orientation (where it occupies the P site on the small subunit and the E site on the large subunit) before EF-G mediated translocation[35]. This suggests the G1338 base is buried

more deeply into the tRNA minor groove in the P/E orientation than in the P/P orientation. Later 16S rRNA mutational studies have also demonstrated that G1338 has a role in stabilizing tRNAs in the P/E orientation. Binding experiments using the 16S rRNA mutant G1338U, which interacts weakly with the tRNA minor groove, show destabilization of tRNA binding relative to wild type. This effect can be compensated by the 23S rRNA mutation C2394A, which disrupts interactions with the tRNA at the E site and shifts the P/P ←→ P/E tRNA binding equilibrium toward the classical P/P state, stabilizing tRNA binding[6]. Together, these studies suggest that tRNAs are more prone to early dissociation from the ribosome in the P/E state than in the P/P state and that G1338 plays a role in the stabilization of tRNAs in the P/E state. Like the P/E orientation, the unique P/I orientation occupied by $tRNA^{fMet}$ when bound to IF2 in initiating 70S ribosome complexes entails a displacement of the tRNA (primarily the acceptor end but also the anticodon stem) toward the E site. Our observation that G1338 binds more deeply in the $tRNA^{fMet}$ M1 minor groove when IF2 is present is consistent with G1338 serving a broader function of stabilizing tRNAs which bind near the P site in non-classical states which may especially require maintenance of strong tRNA-ribosome interactions to prevent tRNA dissociation.

4.4: $tRNA^{fMet}$ M1 does not cause frameshifting during initiation

Ribosome toeprint analysis is a molecular biology technique which uses inhibition of extension of a labeled DNA primer by reverse transcriptase to determine of the position of ribosomes on mRNA molecules within a sample to single-nucleotide resolution. Results from past toeprint analysis experiments performed by the Fredrick Lab suggested that 30S and 70S ICs containing $tRNA^{fMet}$ paired with a CUG start codon may occupy a shifted mRNA reading frame compared to ICs containing the canonical start codons AUG, GUG, and UUG[2]. Because frameshifting during initiation would change the sequence of the entire synthesized polypeptide downstream of the start codon, this would be particularly detrimental to the fidelity of translation

and would potentially explain why bacteria have evolved to use CUG as a start codon only very rarely. Toeprint samples of $tRNA^{fMet}$ M1 + CUG ICs display a shift of their toeprint bands by 1 or 2 nucleotides in the 3' direction, with the apparent +2 reading frame band comprising the major product in these reactions[2]. In contrast to these experimental results, our 70S IC structures containing $tRNA^{fMet}$ M1 paired with each of the four possible NUG start codons (where N is any RNA nucleotide) suggest that these 70S complexes occupy the 0 reading frame. In the CUG start codon-containing mRNA used in two of our structures, the 0, +1, and +2 reading frames have P-site codons of sequence CUG, UGG, and GGU, respectively, which differ in their arrangements of purine and pyrimidine bases. Cryo-EM map density for the CUG complex is suggestive of a pyrimidine-pyrimidine-purine codon in the P site in both the presence and absence of IF2, which would indicate the P-site codon is CUG. Additionally, it is possible to use tRNA binding to monitor codon presentation at the ribosomal A site[36]. In the 0 reading frame, a GUA codon should be presented at the A site, while in the +2 reading frame, the A-site codon would be AUA. AUA codons are decoded by an uncommon $tRNA^{Ile}$ isoacceptor, $tRNA^{IleX}$ [37, 38], which was added to the CUG start codon 70S complex assembly reaction lacking IF2 and excluded from the reactions containing AUG, GUG, and UUG start codons. The AUG, GUG, and UUG samples displayed A-site tRNA density in approximately 9% of picked particles, representing a background level of A-site occupancy in complexes known to occupy the 0 reading frame. Because these samples were prepared without $tRNA^{IleX}$, the observed A-site tRNA density represents only $tRNA^{fMet}$ M1 bound at the A site. The CUG start codon sample contained A-site tRNA density in 10.7% of picked 70S particles, only a slight enrichment in A-site occupancy compared to the known 0-frame complexes containing AUG, GUG, or UUG start codons. Because the apparent +2 frame band is the major product in toeprint analysis assays, we expected to observe a substantially larger population (roughly 50% of 70S particles based on toeprint results) of A-site tRNA-containing particles compared to samples prepared without $tRNA^{IleX}$ if the apparent +2 frame band represents a genuine frameshifted 70S complex. Because we did not observe this, and because P-site mRNA

codon density is suggestive of a 0 frame complex, we conclude that $tRNA^{fMet}$ M1 likely does not engage mRNA containing a CUG start codon in a shifted reading frame and that bacteria have evolved to discriminate against noncanonical CUG start codons for reasons other than a tendency to frameshift during initiation.

An alternative explanation for the shifted toeprint pattern observed by the Fredrick Lab is a change in the mRNA path within the ribosome. If the mRNA occupies an altered conformation in the presence of $tRNA^{fMet}$ M1 paired with a CUG start codon, it could alter the accessibility of the mRNA to reverse transcriptase in toeprint assays without altering the reading frame (and therefore preserving tRNA pairing with the CUG codon at the ribosomal P site)[2]. Given the reduced peptide bond formation activity exhibited by 70S ribosome complexes prepared with $tRNA^{fMet}$ M1 paired to a CUG start codon, the Fredrick Lab proposed that the mRNA conformation in the ribosomal A site may be altered such that the ribosome cannot productively engage tRNAs there. Although cryo-EM map quality is typically poor for A-site mRNA codons in 70S ribosome complexes lacking A-site tRNAs, the map quality was sufficiently high for comparison to published structures of 70S complexes known to productively engage tRNAs at the A site. In all of our structures of complexes prepared without IF2, A-site mRNA density suggests that the mRNA positioning is normal, deviating only slightly from A-site codon positioning observed when a tRNA is present (PDB 7K00[39]). Additionally, we observe no non-canonical interactions of the first-position A-site codon nucleotide G_{+4}, which was previously hypothesized to form non-canonical interactions with either the P-site tRNA or the nearby rRNA in a manner which would explain both the reduced peptide bond formation activity and altered toeprint banding observed for these complexes[2].

A limitation of our cryo-EM-based approach in this study is that, given that our structural data represent snapshots of these initiation complexes, and given that we do not clearly observe either frameshifting or A-site codon mispositioning, we are unable to propose a conclusive

mechanism for the altered toeprint banding observed in the Fredrick Lab's prior experiments. The lack of apparent frameshifting or mispositioning of the A-site mRNA codon suggest that toeprint assays are reporting on other features of the 70S ICs leading to altered mRNA accessibility to reverse transcriptase. Although alteration of mRNA positioning 3' of the A site has been proposed as another alternative explanation of the observed change in the toeprint band pattern of CUG start codon complexes compared to AUG, GUG, and UUG start codon complexes, map density 3' of the A site is of insufficient quality to evaluate this. Because cryo-EM maps represent the average conformation of particles in the dataset, it is possible that the mRNA position is dynamic either at the A site or along the mRNA path downstream of the A site, but our cryo-EM data alone are not sufficient to determine this.

4.5: Mechanisms of resistance evasion by 4,6-DOS aminoglycosides

Methylation of 16S ribosomal RNA helix 44 (h44) at atom N1 of nucleotide A1408 confers a spectrum of resistance to 4,6-disubstituted 2-deoxystreptamine (4,6-DOS) aminoglycoside antibiotics, with some drugs displaying nearly completely abolished antibiotic activity and others experiencing a relatively small increase in minimum inhibitory concentration (MIC)[40, 41]. This must be due to chemical features of certain 4,6-DOS aminoglycosides rendering them more capable of evading resistance than others. Identifying these features is crucial for the rational improvement of aminoglycosides, and while prior studies of m^1A1408-mediated aminoglycoside resistance have observed a spectrum of MIC values in the presence of m^1A1408, these studies have not determined generalizable principles describing aminoglycoside features which maximize antibiotic activity in the presence of the resistance modification. Structural studies of aminoglycoside-bound ribosomes with and without methylation at h44 can reveal the features which permit accommodation of aminoglycosides into their binding site when A1408 is methylated; however, cryo-EM structure determination of high-MIC aminoglycosides bound to

methylated ribosomes may be infeasible due to their low binding affinity to resistant ribosomes. Molecular dynamics (MD) simulations of 4,6-DOS aminoglycoside binding to h44 with or without methylations at A1408 can provide useful information about drug-ribosome interactions even in cases where determining a cryo-EM structure is not possible[42]. Our combined cryo-EM and MD approach has revealed several key features governing aminoglycoside binding in the presence of A1408 methylation. These include antibiotic ring flexibility, the nature and polarity of ring substituent groups, and the presence of additional modifications that anchor the drug to h44 (Fig. 3).

4.6: Influence of drug structure flexibility

Compared to aminoglycoside-bound h44 structures lacking A1408 methylation, the methyl group on m^1A1408 introduces a clash with Ring I of the aminoglycoside. This necessitates a displacement of Ring I away from m^1A1408 to accommodate the drug into its binding site, suggesting that aminoglycosides which are more flexible around the Ring I-II glycosidic linkage should be more evasive of A1408-mediated resistance than those which are more rigid. We find that the presence of Ring I 3' and 4' substitutions negatively impact the flexibility of Ring I to changes in ring pucker and rotation about the glycosidic linkage. Bekanamycin (Bek), tobramycin (Tob), and dibekacin (Dbk) are kanamycin scaffold antibiotics having identical Rings II and III but differing in their degree of Ring I substitution, making them ideal samples for determining the effects of Ring I substituents on resistance evasion[43, 44]. Bek possesses 3' and 4'-OH groups, Tob has only a 4'-OH group and is unsubstituted at the 3' position, and Dbk is unsubstituted at both the 3' and 4' positions. Increasing substitution in these positions restricts Ring I flexibility, but the 4'-OH group interacts with the rRNA backbone at nucleotide A1492. This interaction appears to be important for drug binding in the context of m^1A1408, as removing it through use of an unsubstituted 4' position decreases resistance evasion despite improving Ring I-II linkage

flexibility. For this reason, preserving substitution at the 4’ position while using an unsubstituted 3’ position (as in Tob) yields greater evasiveness than either 3’,4’-disubstituted drugs (*e.g.*, Bek) or 3’,4’-unsubstituted drugs (*e.g.*, Dbk).

Importantly, improved flexibility at the Ring I-II linkage does not universally improve drug binding when A1408 is methylated. Our MD simulations suggest that the preferred conformations of aminoglycoside drugs free in solution (driven by intramolecular interactions) also affect their ability to accommodate m^1A1408. Because aminoglycosides bind their h44 target in the *syn*-Ψ conformation (with the Ring I-II dihedral angle near 0°), alternative stable conformations in solution (*e.g.*, *anti*-Ψ, with the dihedral angle near 180°) impose an energy penalty to binding, whereby to bind h44, an aminoglycoside must first transition out of a local energy minimum. Free kanamycin appears to be especially flexible in simulations but tends to occupy the *anti*-Ψ conformation in free solution, explaining its anomalously high MICs under conditions of A1408 methylation. In contrast, free Bek, Tob, and Dbk primarily occupy the *syn*-Ψ conformation in simulations due to repulsion between two positively charged amino substituents in the *anti*-Ψ conformation. This suggests their ability to accommodate m^1A1408 is limited primarily by factors such as their ring pucker flexibility and their ability to contact the rRNA backbone rather than needing to undergo an energetically unfavorable conformational change before binding.

Further evidence of the importance of ring pucker flexibility in the ability of aminoglycosides to evade m^1A1408-mediated resistance is provided by netilmicin (Net), which, unlike 4,6-DOS aminoglycosides of the kanamycin or gentamicin scaffolds, possesses a carbon-carbon double bond in Ring I[45]. The double bond confers rigidity to Ring I, rendering it less amenable to changes in ring pucker. Compared to aminoglycosides with similar Ring II and III scaffolds, Net is less evasive of m^1A1408-mediated resistance, which is corroborated by MD simulations showing that it is unable to accommodate the presence of the *N1*-methyl group on A1408 and is quickly ejected from its binding site.

4.7: Influence of Ring I substituent identity

Methylation of A1408 imparts a positive charge to the nucleobase, which can impact its interaction with aminoglycosides[46, 47]. The 6' position of Ring I, which interacts with atom N1 of A1408, can be substituted with either an amino or hydroxyl moiety, with some aminoglycosides, such as G418, having additional branching groups at this position[44]. At physiological pH, amino moieties are primarily protonated (i.e., $-NH_3^+$) and therefore positively charged, while hydroxyl groups remain neutral[45]. Given the charge characteristics at this position, we expected to observe greater resistance evasion in the presence of m^1A1408 among aminoglycosides possessing 6'-OH groups compared to 6'-NH_3^+ groups due to electrostatic repulsion of 6'-NH_3^+ by m^1A1408. As predicted, MIC assays and simulations of 6'-OH-containing aminoglycosides (e.g., G418) and 6'-NH_3^+-containing aminoglycosides (e.g., gentamicin C1A) with similar Ring II and Ring III scaffolds suggest a 6'-OH is preferred for binding when h44 is methylated.

4.8: Influence of Ring II HABA group

Cryo-EM structures of A1408-methylated and unmethylated *E. coli* ribosomes containing the aminoglycoside drug arbekacin, which performed especially well in MIC assays against *E. coli* cells expressing the A1408 *N1*-methyltransferase NpmA, demonstrate that chemical modifications to the base aminoglycoside scaffold can preserve drug binding in the context of A1408 methylation by compensating for the loss of rRNA-drug hydrogen bonds due to displacement of Ring I. In contrast to many other 4,6-DOS aminoglycosides, arbekacin contains a 4-amino-2-hydroxybutyroyl amide (L-HABA) modification on Ring II which forms additional contacts with h44 distant from the site of interaction with nucleotide A1408[48-50]. These interactions, along with the tolerance of arbekacin's structure to rotation along the glycosidic linkage between

Rings I and II, stabilize drug binding despite A1408 methylation. This leads to only a slight displacement of Rings II and III in the A1408-methylated structure compared to the A1408-unmethylated structure. Interestingly, the addition of a HABA group appears to be able to compensate for suboptimal characteristics in other parts of the drug's structure. For example, Abk is produced by addition of a HABA group to Ring II of Dbk. In MIC assays, Abk is one of the most resistance-evasive 4,6-DOS aminoglycosides tested, while Dbk evades resistance poorly.

4.9: Considerations for antibiotic design

In addition to studying accommodation of m^1A1408 by existing aminoglycoside drugs, this simulation platform also provides a valuable system for predicting resistance evasion in hypothetical new aminoglycosides which have not yet been manufactured. In this study, we only simulated the interaction of bacterial ribosomes with antibiotics which are already available; however, using the principles discovered in this study for maximization of activity in the presence of m^1A1408, newly designed aminoglycosides could be simulated to predict their activity in the presence of this resistance modification. This could aid in the development of new aminoglycosides by narrowing the space of new drug structures which need to be produced and tested against resistant pathogens expressing A1408 methyltransferases.

A challenge for aminoglycoside design and use, and a reason for their use as last-resort antibiotics, is their tendency to cause toxicity in patients (ototoxicity, nephrotoxicity), especially during extended use, due to their ability to bind and disrupt decoding in human ribosomes[51-54]. For this reason, it is of interest when rationally optimizing aminoglycoside design to also consider activity against human cytoplasmic and mitochondrial ribosomes, and, where possible, to minimize features in the drug structure that encourage disruption of translation in human cells. The interactions between aminoglycosides and eukaryotic ribosomes are well characterized, with

binding data and published structures with bound 4,5-DOS and 4,6-DOS aminoglycosides available for both mitochondrial and cytoplasmic eukaryotic ribosomes (or model RNAs consisting of decoding center nucleotides from these ribosomes)[55-60]. While identifying toxicity in human cells by existing aminoglycosides is straightforward and could be tested directly in cultured cell lines with cell viability assays[61, 62], the simulation platform presented in our study could additionally be used to predict the interactions of aminoglycoside antibiotics with their binding sites in human ribosomes. Another challenge is presented by the fact that, while bacterial and eukaryotic rRNA sequences have diverged over time, the functional centers of the ribosome are highly conserved[63-65]. For this reason, modifications to antibiotic structures which render them more potent against bacterial translation may also render them more active against human ribosomes, which risks amplifying toxic side effects. Human mitochondrial ribosomes possess an A1408 residue (using *E. coli* numbering), which may complicate the design of aminoglycosides with improved binding to A1408 or nearby regions of h44 in bacteria[56, 60, 66].

A limitation of the combined simulation and cryo-EM approach used in our study of aminoglycoside antibiotic resistance evasion lies in the agreement between the simulations and experimental structural data. Because cryo-EM is based on image averaging, the map data most clearly reflect the most abundant conformations of the ribosomes and associated aminoglycoside ligands in the sample, with visibility of low frequency or partially occupied states being suppressed[67]. While this permits modeling the drug in what is likely its lowest energy conformation, this may not reflect all possible conformations of aminoglycosides at their h44 binding site. In particular, Ring I 6'-NH_3^+ substituents, which interact with atom N1 of A1408 in unmethylated structures, appear to occupy both the *trans-gauche* (flipped away from m^1A1408 and toward the A1492-A1493 phosphate backbone) and *gauche-trans* (flipped toward m^1A1408) configurations in simulations of m^1A1408-containing rRNA, while we only observe this substituent in the *gauche-trans* configuration in our cryo-EM data. This suggests either that the cryo-EM data

do not reflect all accessible conformations of aminoglycosides at h44 or that the simulation system used does not accurately model the interaction of aminoglycosides with h44 in all aspects. If *trans-gauche* accommodation at h44 is possible in the presence of A1408 *N1*-methylation but happens infrequently compared to *gauche-trans* accommodation, the cryo-EM map density may not reflect this. Alternatively, it is possible that the simulation parameters chosen for this study tend to overestimate the electrostatic repulsion of 6'-NH_3^+ by m^1A1408 and that *trans-gauche* accommodation is either infeasible or uncommon. In this case, modification of simulation parameters could bring the empirical structures and simulation data further into agreement.

4.10: Conclusions

The work presented in this dissertation has generated novel findings relating to the maintenance and disruption of protein synthesis fidelity during the initiation and elongation phases of bacterial translation. Our structures of *E. coli* 70S ribosomes initiating translation using $tRNA^{fMet}$ M1, a mutant variant of the bacterial initiator tRNA with weakened interactions with the ribosomal P site, have demonstrated a possible mechanism for the quality control role of the GTPase initiation factor IF2, which directly binds $tRNA^{fMet}$ during the assembly of the 30S IC. During initiation, IF2 improves interactions between the conserved 16S rRNA nucleotide G1338 and the minor groove of the $tRNA^{fMet}$ anticodon stem and stabilizes $tRNA^{fMet}$ M1 in the initiation complex, helping to explain the ability of IF2 to restore wild type-like initiation behavior with $tRNA^{fMet}$ M1. Our work adds to a body of evidence showing that the stability of tRNA binding at the P site is particularly sensitive to the strength of A-minor interactions between the P-site rRNA nucleotides A1339 and G1338 and the tRNA minor groove and suggests that, like translation elongation, translation initiation is tuned for an intermediate mix of efficiency and accuracy based on the strength of both tRNA-mRNA and tRNA-ribosome interactions. Additionally, these structures provide evidence that previously hypothesized mRNA frameshifts or mispositioning of the A-site

mRNA codon following initiation using $tRNA^{fMet}$ M1 on a CUG start codon do not occur, suggesting that $tRNA^{fMet}$ M1 likely disrupts normal ribosome toeprint band formation through a change in the mRNA conformation elsewhere on the ribosome and that bacteria have evolved to discriminate against CUG as a translational start codon for reasons other than a tendency to frameshift during initiation.

Finally, our combined cryo-EM and molecular dynamics simulation approach to studying 4,6-DOS aminoglycoside resistance evasion has suggested a series of aminoglycoside design principles which could be used to maximize evasion of resistance mediated by 16S A1408 *N1*-methylation. While the ability of m^1A1408 to confer varying degrees of resistance to 4,6-DOS aminoglycosides has been known from past studies, the features governing the ability of these drugs to overcome this mode of resistance have not. Aminoglycoside features which improve Ring I flexibility while preserving key contacts with the rRNA tend to improve accommodation of A1408 N1-methylation. 6'-OH groups yield improved resistance evasion compared to 6'-NH_3^+ due to a lack of electrostatic repulsion toward m^1A1408; however, this may not be preferred in practice due to high activity against human ribosomes[56, 58]. Finally, additional functional groups (*e.g.*, L-HABA) added to Ring II can anchor the aminoglycoside at its binding site through additional contacts with the rRNA distal to m^1A1408 and can compensate for suboptimal drug characteristics on Ring I. These design principles can be used to rationally modify aminoglycosides to preserve the activity of this critical antibiotic class, and the simulation platform could feasibly be extended and used alongside cell-based aminoglycoside toxicity assays to predict and reduce activity against eukaryotic ribosomes. As m^1A1408-mediated resistance becomes increasingly common, these aminoglycoside design principles can assist in maintaining the efficacy of this essential class of antibiotics.

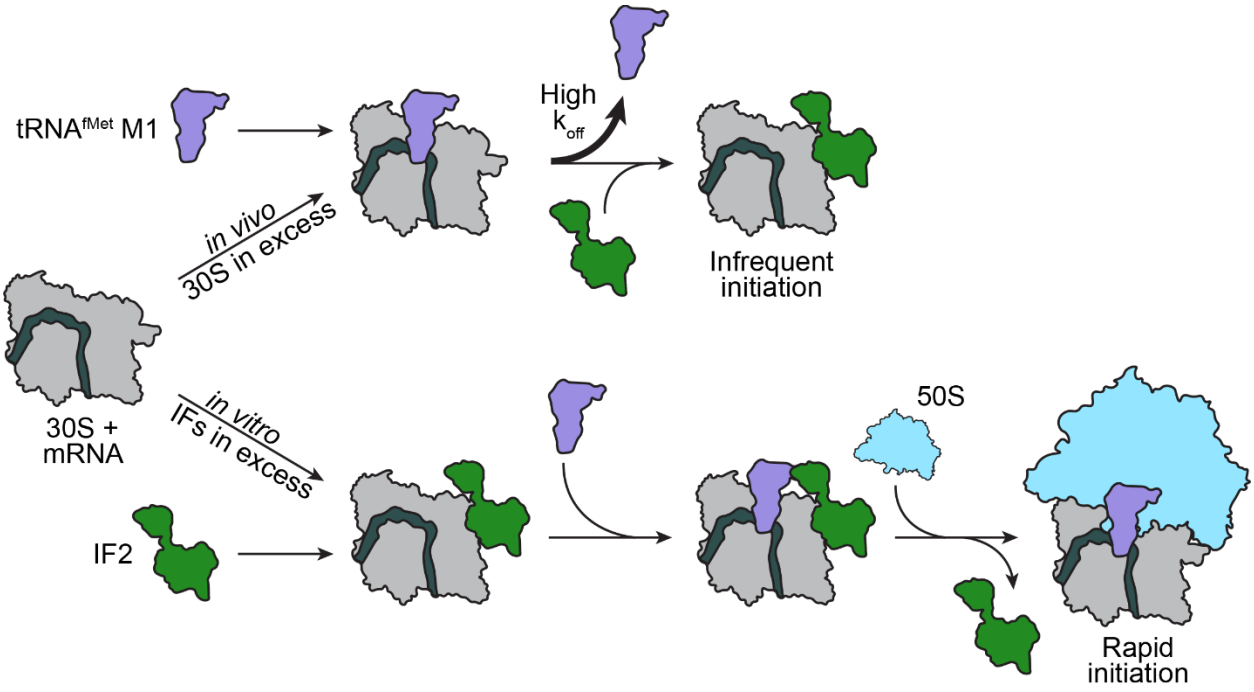

Fig. 1. Proposed mechanism for differences between tRNA^{fMet} M1 effects on *in vivo* vs. *in vitro* initiation. 30S subunits bound to mRNA must associate with an initiator tRNA and initiation factors to recruit the 50S subunit and begin translation. *Upper* – *in vivo*, where ribosomes are in excess relative to IFs, tRNA^{fMet} M1 may associate with 30S subunits before IFs. However, because of its high off-rate due to weak interactions with the 16S rRNA, it may tend to unbind before IFs arrive, making colocation of the initiator tRNA and IFs on the 30S (and hence translation initiation) more infrequent relative to wild type tRNA^{fMet}. *Lower* – in prior *in vitro* studies of initiation using tRNA^{fMet} M1, IFs have been provided in excess relative to ribosomes. Because the 30S IC components may assemble in any order and IFs are in excess, IFs (particularly IF2) may pre-associate with the 30S, permitting rapid recruitment of the 50S and initiation of translation when tRNA^{fMet} M1 binds.

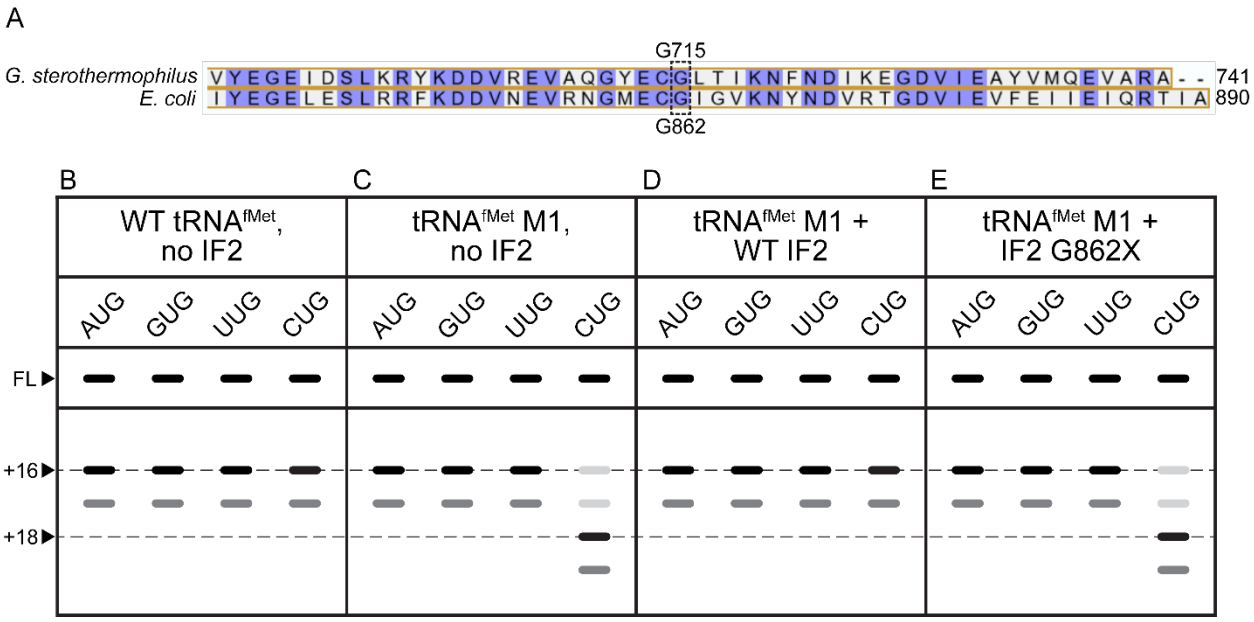

Fig. 2. Proposed results of toeprint assays using IF2 G862X. A). Sequence alignment of *G. stearothermophilus* and *E. coli* IF2. Residue G715 in *G. stearothermophilus* corresponds to residue G862 in *E. coli*. B). 70S ICs prepared non-enzymatically with wild type $tRNA^{fMet}$ should display a normal toeprint pattern irrespective of the start codon used in complex assembly, with the major product band occurring at the +16 position. “FL” band corresponds to expected full-length RT runoff product from mRNA molecules not bound to ribosomes. C). 70S ICs prepared non-enzymatically with $tRNA^{fMet}$ M1 should display typical toeprint banding patterns for AUG, GUG, and UUG start codons and should display a banding pattern with the major product at the +18 position when assembled with a CUG start codon. D). The addition of IF2 during complex assembly with $tRNA^{fMet}$ M1 restores toeprint banding in complexes assembled with a CUG start codon to the +16 position without affecting the appearance of bands for complexes prepared with an AUG, GUG, or UUG start codon. E). If interactions between IF2 and the $tRNA^{fMet}$ M1 acceptor end are essential for rescue of normal toeprint banding with a CUG start codon, complexes assembled using IF2 G862X should yield results similar to non-enzymatically assembled 70S initiation complexes containing $tRNA^{fMet}$ M1.

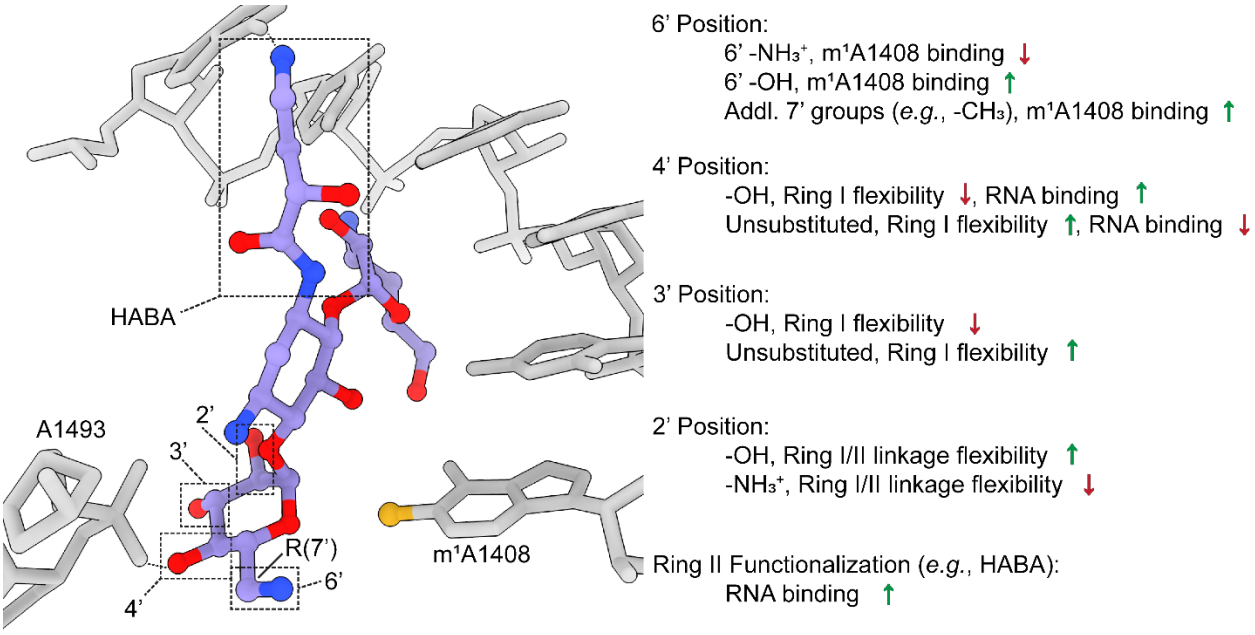

Fig. 3. Aminoglycoside design principles for evasion of m^{1}A1408-mediated resistance. At the 6' position of Ring II, -OH groups yield improved binding to m^{1}A1408 vs. -NH_3^+, while additional branching functional groups at the 7' position (such as -CH_3) also improve binding when A1408 is methylated. At the 4' position, substitution with -OH allows the aminoglycoside to maintain contact with the 16S A1493 backbone, improving RNA binding at a small cost of reduced Ring I flexibility. Substitutions at the 3' position negatively impact resistance evasion, as they reduce Ring I flexibility while their contacts with the rRNA appear to be dispensable. 2' -OH substitutions are preferred over 2' -NH_3^+, as the latter reduces conformational flexibility around the Ring I/II glycosidic linkage due to electrostatic repulsion with positively-charged -NH_3^+ group on Ring II. Finally, additional Ring II functionalizations such as L-HABA can preserve drug-RNA binding in the context of A1408 methylation by making additional contacts with the rRNA that anchor the drug at its binding site.

References

1. Rodnina MV. Translation in Prokaryotes. LID - 10.1101/cshperspect.a032664 [doi] LID - a032664(1943-0264 (Electronic)).
2. Roy B, Liu Q, Shoji S, Fredrick K. IF2 and unique features of initiator tRNAfMet help establish the translational reading frame. RNA Biology. 2018;15(4-5):604-13. doi: 10.1080/15476286.2017.1379636.
3. ABDI NM, FREDRICK K. Contribution of 16S rRNA nucleotides forming the 30S subunit A and P sites to translation in Escherichia coli. RNA. 2005;11(11):1624-32. doi: 10.1261/rna.2118105.
4. Lancaster L, Noller HF. Involvement of 16S rRNA Nucleotides G1338 and A1339 in Discrimination of Initiator tRNA. Molecular Cell. 2005;20(4):623-32. doi: https://doi.org/10.1016/j.molcel.2005.10.006.
5. Qin D, Abdi NM, Fredrick K. Characterization of 16S rRNA mutations that decrease the fidelity of translation initiation. RNA. 2007;13(12):2348-55. doi: 10.1261/rna.715307.
6. Shoji S, Abdi NM, Bundschuh R, Fredrick K. Contribution of ribosomal residues to P-site tRNA binding. Nucleic Acids Research. 2009;37(12):4033-42. doi: 10.1093/nar/gkp296.
7. Qin D, Fredrick K. Control of translation initiation involves a factor-induced rearrangement of helix 44 of 16S ribosomal RNA. Mol Microbiol. 2009;71(5):1239-49. Epub 20090116. doi: 10.1111/j.1365-2958.2009.06598.x. PubMed PMID: 19154330; PMCID: PMC3647337.
8. Mattingly JM, Nguyen HA, Roy B, Fredrick K, Dunham CM. Structural analysis of noncanonical translation initiation complexes. Journal of Biological Chemistry. 2024;300(10). doi: 10.1016/j.jbc.2024.107743.
9. Bowie JU, Reidhaar-Olson JF, Lim WA, Sauer RT. Deciphering the Message in Protein Sequences: Tolerance to Amino Acid Substitutions. Science. 1990;247(4948):1306-10. doi: doi:10.1126/science.2315699.
10. Guo HH, Choe J, Loeb LA. Protein tolerance to random amino acid change. Proceedings of the National Academy of Sciences. 2004;101(25):9205-10. doi: doi:10.1073/pnas.0403255101.
11. Bremer H, Dennis PP. Modulation of chemical composition and other parameters of the cell by growth rate. Escherichia coli and Salmonella: cellular and molecular biology. 1996;2(2):1553-69.
12. Li GW, Burkhardt D, Gross C, Weissman JS. Quantifying absolute protein synthesis rates reveals principles underlying allocation of cellular resources. Cell. 2014;157(3):624-35. doi: 10.1016/j.cell.2014.02.033. PubMed PMID: 24766808; PMCID: PMC4006352.
13. Klumpp S, Scott M, Pedersen S, Hwa T. Molecular crowding limits translation and cell growth. Proceedings of the National Academy of Sciences. 2013;110(42):16754-9. doi: doi:10.1073/pnas.1310377110.
14. Matamouros S, Gensch T, Cerff M, Sachs CC, Abdollahzadeh I, Hendriks J, Horst L, Tenhaef N, Tenhaef J, Noack S, Graf M, Takors R, Nöh K, Bott M. Growth-rate dependency of ribosome abundance and translation elongation rate in Corynebacterium glutamicum differs from that in Escherichia coli. Nature Communications. 2023;14(1):5611. doi: 10.1038/s41467-023-41176-y.
15. Kramer EB, Farabaugh PJ. The frequency of translational misreading errors in E. coli is largely determined by tRNA competition. Rna. 2007;13(1):87-96. Epub 20061109. doi: 10.1261/rna.294907. PubMed PMID: 17095544; PMCID: PMC1705757.
16. Fijalkowska IJ, Schaaper RM, Jonczyk P. DNA replication fidelity in Escherichia coli: a multi-DNA polymerase affair. FEMS Microbiol Rev. 2012;36(6):1105-21. Epub 20120405. doi: 10.1111/j.1574-6976.2012.00338.x. PubMed PMID: 22404288; PMCID: PMC3391330.

17. Bębenek A, Ziuzia-Graczyk I. Fidelity of DNA replication-a matter of proofreading. Curr Genet. 2018;64(5):985-96. Epub 20180302. doi: 10.1007/s00294-018-0820-1. PubMed PMID: 29500597; PMCID: PMC6153641.
18. Spencer PS, Barral JM. Genetic code redundancy and its influence on the encoded polypeptides. Comput Struct Biotechnol J. 2012;1:e201204006. Epub 20120320. doi: 10.5936/csbj.201204006. PubMed PMID: 24688635; PMCID: PMC3962081.
19. Traverse CC, Ochman H. Conserved rates and patterns of transcription errors across bacterial growth states and lifestyles. Proceedings of the National Academy of Sciences. 2016;113(12):3311-6. doi: doi:10.1073/pnas.1525329113.
20. Andersson DI, van Verseveld HW, Stouthamer AH, Kurland CG. Suboptimal growth with hyper-accurate ribosomes. Arch Microbiol. 1986;144(1):96-101. doi: 10.1007/bf00454963. PubMed PMID: 3963992.
21. Ruusala T, Andersson D, Ehrenberg M, Kurland CG. Hyper-accurate ribosomes inhibit growth. The EMBO Journal. 1984;3(11):2575-80. doi: https://doi.org/10.1002/j.1460-2075.1984.tb02176.x.
22. Björkman J, Samuelsson P, Andersson DI, Hughes D. Novel ribosomal mutations affecting translational accuracy, antibiotic resistance and virulence of Salmonella typhimurium. Molecular Microbiology. 1999;31(1):53-8. doi: https://doi.org/10.1046/j.1365-2958.1999.01142.x.
23. Gorini L, Kataja E. PHENOTYPIC REPAIR BY STREPTOMYCIN OF DEFECTIVE GENOTYPES IN E. COLI[*]. Proceedings of the National Academy of Sciences. 1964;51(3):487-93. doi: doi:10.1073/pnas.51.3.487.
24. Battle DJ, Doudna JA. Specificity of RNA-RNA helix recognition. Proc Natl Acad Sci U S A. 2002;99(18):11676-81. Epub 20020820. doi: 10.1073/pnas.182221799. PubMed PMID: 12189204; PMCID: PMC129328.
25. Doherty EA, Batey RT, Masquida B, Doudna JA. A universal mode of helix packing in RNA. Nat Struct Biol. 2001;8(4):339-43. doi: 10.1038/86221. PubMed PMID: 11276255.
26. Mandal N, Mangroo D, Dalluge JJ, McCloskey JA, RajBhandary UL. Role of the three consecutive G:C base pairs conserved in the anticodon stem of initiator tRNAs in initiation of protein synthesis in Escherichia coli. RNA. 1996;2(5):473-82.
27. Milón P, Maracci C, Filonava L, Gualerzi CO, Rodnina MV. Real-time assembly landscape of bacterial 30S translation initiation complex. Nature Structural & Molecular Biology. 2012;19(6):609-15. doi: 10.1038/nsmb.2285.
28. Milón P, Rodnina MV. Kinetic control of translation initiation in bacteria. Critical Reviews in Biochemistry and Molecular Biology. 2012;47(4):334-48. doi: 10.3109/10409238.2012.678284.
29. Laursen BS, Sørensen Hp Fau - Mortensen KK, Mortensen Kk Fau - Sperling-Petersen HU, Sperling-Petersen HU. Initiation of protein synthesis in bacteria(1092-2172 (Print)).
30. Bremer H, Dennis Patrick P. Modulation of Chemical Composition and Other Parameters of the Cell at Different Exponential Growth Rates. EcoSal Plus. 2008;3(1):10.1128/ecosal.5.2.3. doi: 10.1128/ecosal.5.2.3.
31. Howe Jg Fau - Hershey JW, Hershey JW. Initiation factor and ribosome levels are coordinately controlled in Escherichia coli growing at different rates(0021-9258 (Print)).
32. Antoun A, Pavlov MY, Lovmar M, Ehrenberg M. How initiation factors maximize the accuracy of tRNA selection in initiation of bacterial protein synthesis. Mol Cell. 2006;23(2):183-93. doi: 10.1016/j.molcel.2006.05.030. PubMed PMID: 16857585.
33. Wintermeyer W, Gualerzi C. Effect of Escherichia coli initiation factors on the kinetics of N-Acphe-tRNAPhe binding to 30S ribosomal subunits. A fluorescence stopped-flow study. Biochemistry. 1983;22(3):690-4. doi: 10.1021/bi00272a025. PubMed PMID: 6340723.
34. Guenneugues M, Caserta E, Brandi L, Spurio R, Meunier S, Pon CL, Boelens R, Gualerzi CO. Mapping the fMet-tRNA(f)(Met) binding site of initiation factor IF2. Embo j.

2000;19(19):5233-40. doi: 10.1093/emboj/19.19.5233. PubMed PMID: 11013225; PMCID: PMC302095.
35. Moazed D, Noller HF. Intermediate states in the movement of transfer RNA in the ribosome. Nature. 1989;342(6246):142-8. doi: 10.1038/342142a0. PubMed PMID: 2682263.
36. Uemura S, Aitken CE, Korlach J, Flusberg BA, Turner SW, Puglisi JD. Real-time tRNA transit on single translating ribosomes at codon resolution. Nature. 2010;464(7291):1012-7. doi: 10.1038/nature08925. PubMed PMID: 20393556; PMCID: PMC4466108.
37. Muramatsu T, Nishikawa K, Nemoto F, Kuchino Y, Nishimura S, Miyazawa T, Yokoyama S. Codon and amino-acid specificities of a transfer RNA are both converted by a single post-transcriptional modification. Nature. 1988;336(6195):179-81. doi: 10.1038/336179a0.
38. Muramatsu T, Yokoyama S, Horie N, Matsuda A, Ueda T, Yamaizumi Z, Kuchino Y, Nishimura S, Miyazawa T. A novel lysine-substituted nucleoside in the first position of the anticodon of minor isoleucine tRNA from Escherichia coli. J Biol Chem. 1988;263(19):9261-7. doi: 10.1351/pac198961030573. PubMed PMID: 3132458.
39. Watson ZL, Ward FR, Méheust R, Ad O, Schepartz A, Banfield JF, Cate JH. Structure of the bacterial ribosome at 2 Å resolution. Elife. 2020;9. Epub 20200914. doi: 10.7554/eLife.60482. PubMed PMID: 32924932; PMCID: PMC7550191.
40. Wachino J, Shibayama K, Kurokawa H, Kimura K, Yamane K, Suzuki S, Shibata N, Ike Y, Arakawa Y. Novel plasmid-mediated 16S rRNA m1A1408 methyltransferase, NpmA, found in a clinically isolated Escherichia coli strain resistant to structurally diverse aminoglycosides. Antimicrob Agents Chemother. 2007;51(12):4401-9. Epub 20070917. doi: 10.1128/aac.00926-07. PubMed PMID: 17875999; PMCID: PMC2168023.
41. Kanazawa H, Baba F, Koganei M, Kondo J. A structural basis for the antibiotic resistance conferred by an N1-methylation of A1408 in 16S rRNA. Nucleic Acids Res. 2017;45(21):12529-35. doi: 10.1093/nar/gkx882. PubMed PMID: 29036479; PMCID: PMC5716097.
42. Nierzwicki Ł, Palermo G. Molecular Dynamics to Predict Cryo-EM: Capturing Transitions and Short-Lived Conformational States of Biomolecules. Front Mol Biosci. 2021;8:641208. Epub 20210405. doi: 10.3389/fmolb.2021.641208. PubMed PMID: 33884260; PMCID: PMC8053777.
43. Krause KM, Serio AW, Kane TR, Connolly LE. Aminoglycosides: An Overview. Cold Spring Harb Perspect Med. 2016;6(6). Epub 20160601. doi: 10.1101/cshperspect.a027029. PubMed PMID: 27252397; PMCID: PMC4888811.
44. Takahashi Y, Igarashi M. Destination of aminoglycoside antibiotics in the ‘post-antibiotic era’. The Journal of Antibiotics. 2018;71(1):4-14. doi: 10.1038/ja.2017.117.
45. Alkhzem AH, Woodman TJ, Blagbrough IS. Individual pKa Values of Tobramycin, Kanamycin B, Amikacin, Sisomicin, and Netilmicin Determined by Multinuclear NMR Spectroscopy. ACS Omega. 2020;5(33):21094-103. doi: 10.1021/acsomega.0c02744.
46. Xiong W, Zhao Y, Wei Z, Li C, Zhao R, Ge J, Shi B. N1-methyladenosine formation, gene regulation, biological functions, and clinical relevance. Mol Ther. 2023;31(2):308-30. Epub 20221029. doi: 10.1016/j.ymthe.2022.10.015; PMCID: PMC9931621.
47. Chen W, Feng P, Tang H, Ding H, Lin H. RAMPred: identifying the N1-methyladenosine sites in eukaryotic transcriptomes. Scientific Reports. 2016;6(1):31080. doi: 10.1038/srep31080.
48. Dozzo P, Moser HE. New aminoglycoside antibiotics. Expert Opinion on Therapeutic Patents. 2010;20(10):1321-41. doi: 10.1517/13543776.2010.506189.
49. Parajuli Narayan P, Mandava Chandra S, Pavlov Michael Y, Sanyal S. Mechanistic insights into translation inhibition by aminoglycoside antibiotic arbekacin. Nucleic Acids Research. 2021;49(12):6880-92. doi: 10.1093/nar/gkab495.
50. Kondo J, François B, Russell RJM, Murray JB, Westhof E. Crystal structure of the bacterial ribosomal decoding site complexed with amikacin containing the γ-amino-α-hydroxybutyryl

(haba) group. Biochimie. 2006;88(8):1027-31. doi: https://doi.org/10.1016/j.biochi.2006.05.017.
51. Fee WE, Jr. Aminoglycoside ototoxicity in the human. Laryngoscope. 1980;90(10 Pt 2 Suppl 24):1-19. doi: 10.1288/00005537-198010001-00001. PubMed PMID: 7432055.
52. Mulheran M, Degg C, Burr S, Morgan DW, Stableforth DE. Occurrence and risk of cochleotoxicity in cystic fibrosis patients receiving repeated high-dose aminoglycoside therapy. Antimicrob Agents Chemother. 2001;45(9):2502-9. doi: 10.1128/aac.45.9.2502-2509.2001. PubMed PMID: 11502521; PMCID: PMC90684.
53. Toubeau G, Laurent G, Carlier MB, Abid S, Maldague P, Heuson-Stiennon JA, Tulkens PM. Tissue repair in rat kidney cortex after short treatment with aminoglycosides at low doses. A comparative biochemical and morphometric study. Lab Invest. 1986;54(4):385-93. PubMed PMID: 3959542.
54. Hock R, Anderson RJ. Prevention of drug-induced nephrotoxicity in the intensive care unit. J Crit Care. 1995;10(1):33-43. doi: 10.1016/0883-9441(95)90029-2. PubMed PMID: 7757141.
55. Tomono J, Asano K, Chiashi T, Suzuki M, Igarashi M, Takahashi Y, Tanaka Y, Yokoyama T. Direct visualization of ribosomes in the cell-free system revealed the functional evolution of aminoglycoside. J Biochem. 2024;175(6):587-98. doi: 10.1093/jb/mvae002. PubMed PMID: 38227611.
56. Prokhorova I, Altman RB, Djumagulov M, Shrestha JP, Urzhumtsev A, Ferguson A, Chang CT, Yusupov M, Blanchard SC, Yusupova G. Aminoglycoside interactions and impacts on the eukaryotic ribosome. Proc Natl Acad Sci U S A. 2017;114(51):E10899-e908. Epub 20171205. doi: 10.1073/pnas.1715501114. PubMed PMID: 29208708; PMCID: PMC5754804.
57. Hyun Ryu D, Rando RR. Aminoglycoside binding to human and bacterial A-Site rRNA decoding region constructs. Bioorganic & Medicinal Chemistry. 2001;9(10):2601-8. doi: https://doi.org/10.1016/S0968-0896(01)00034-7.
58. Hong S, Harris KA, Fanning KD, Sarachan KL, Frohlich KM, Agris PF. Evidence That Antibiotics Bind to Human Mitochondrial Ribosomal RNA Has Implications for Aminoglycoside Toxicity *. Journal of Biological Chemistry. 2015;290(31):19273-86. doi: 10.1074/jbc.M115.655092.
59. Lynch SR, Puglisi JD. Structural origins of aminoglycoside specificity for prokaryotic ribosomes1 1Edited by I. Tinoco. Journal of Molecular Biology. 2001;306(5):1037-58. doi: https://doi.org/10.1006/jmbi.2000.4420.
60. Kondo J, Westhof E. The bacterial and mitochondrial ribosomal A-site molecular switches possess different conformational substates. Nucleic Acids Research. 2008;36(8):2654-66. doi: 10.1093/nar/gkn112.
61. Varghese DS, Parween S, Ardah MT, Emerald BS, Ansari SA. Effects of Aminoglycoside Antibiotics on Human Embryonic Stem Cell Viability during Differentiation In Vitro. Stem Cells International. 2017;2017(1):2451927. doi: https://doi.org/10.1155/2017/2451927.
62. Kumar P, Nagarajan A, Uchil PD. Analysis of Cell Viability by the MTT Assay. Cold Spring Harbor Protocols. 2018;2018(6):pdb.prot095505. doi: 10.1101/pdb.prot095505.
63. Matt T, Akbergenov R, Shcherbakov D, Böttger EC. The Ribosomal A-site: Decoding, Drug Target, and Disease. Israel Journal of Chemistry. 2010;50(1):60-70. doi: https://doi.org/10.1002/ijch.201000003.
64. Wilson DN, Doudna Cate JH. The Structure and Function of the Eukaryotic Ribosome. Cold Spring Harbor Perspectives in Biology. 2012;4(5). doi: 10.1101/cshperspect.a011536.
65. Melnikov S, Ben-Shem A, Garreau de Loubresse N, Jenner L, Yusupova G, Yusupov M. One core, two shells: bacterial and eukaryotic ribosomes. Nature Structural & Molecular Biology. 2012;19(6):560-7. doi: 10.1038/nsmb.2313.
66. Perez-Fernandez D, Shcherbakov D, Matt T, Leong NC, Kudyba I, Duscha S, Boukari H, Patak R, Dubbaka SR, Lang K, Meyer M, Akbergenov R, Freihofer P, Vaddi S, Thommes P,

Ramakrishnan V, Vasella A, Böttger EC. 4′-O-substitutions determine selectivity of aminoglycoside antibiotics. Nature Communications. 2014;5(1):3112. doi: 10.1038/ncomms4112.
67. Thouvenin E, Hewat E. When two into one won't go: fitting in the presence of steric hindrance and partial occupancy. Acta Crystallographica Section D: Biological Crystallography. 2000;56(10):1350-7.